

# POLITECNICO DI TORINO

Corso di Laurea Magistrale

in

Ingegneria Aerospaziale

Tesi di Laurea Magistrale

Spacecraft – Plasma Interactions for a LEO – GEO Mission

Tug with Direct Drive Hall Effect Thruster



Relatore

*Prof.ssa Sabrina Corpino*

Correlatore

*Dott. Tommaso Andreussi*

Candidato

*Francesco Secchia*

Anno Accademico 2017/2018



*I have whirl'd with the earth at the dawning,  
When the sky was a vaporous flame;  
I have seen the dark universe yawning,  
Where the black planets roll without aim;  
Where they roll in their horror unheeded, without knowledge or lustre or name.*

*Ho vorticato con la terra all'alba,  
Quando il cielo era una fiamma vaporosa;  
Ho visto l'universo oscuro che sbadiglia,  
Dove i pianeti neri rotolano senza scopo;  
Dove rotolano nel loro orrore inascoltati, senza conoscenza, lustro o nome.*

*H.P. Lovecraft, Nemesis.*

# Index

Index .....	I
Premessa.....	V
Abstract.....	VII
List of Figures .....	IX
List of Tables .....	XIII
List of Acronyms and Abbreviations .....	XV
1 Chapter 1 .....	1
1.1 Space Propulsion.....	1
1.2 Electric Propulsion.....	4
1.3 Electrostatic Propulsion .....	8
1.3.1 Electron Bombardment .....	9
1.3.2 Neutralization.....	9
1.3.3 Hall Current.....	9
2 Chapter 2 .....	11
2.1 Development History of Hall Thrusters .....	11
2.2 Application and Present Capabilities .....	12
2.3 Particle Motion and Hall Parameter .....	13
2.4 General Scheme and Acceleration Process .....	15
2.4.1 Generation of the Thrust .....	18
2.4.2 Internal Currents.....	19
2.5 HT20k Performance.....	21
3 Chapter 3 .....	25
3.1 Space Tug Surroundings .....	25
3.2 Tug Properties .....	26
3.3 Electric Orbit Raising.....	28
3.4 GTO – GEO .....	29
3.4.1 GTO to GEO Tug.....	34
3.5 Spiral LEO – GEO .....	34
3.5.1 STK Study.....	36

3.5.2	STK Results .....	41
3.5.3	Eclipses Considerations .....	42
4	Chapter 4 .....	43
4.1	Mission Concept .....	43
4.2	System Design.....	43
4.2.1	Electric Propulsion Subsystem (EP) .....	45
4.2.2	Electrical Power System EPS.....	46
4.2.3	Solar Array .....	47
4.3	Structural Design.....	48
4.4	Introduction to Direct Drive.....	49
4.4.1	Differences .....	50
4.5	Direct-Drive Mass Benefits.....	52
4.6	Direct Advantages.....	53
4.6.1	PPU Reduction .....	53
4.6.2	Thermal Control System .....	54
4.7	Indirect Advantages .....	54
4.7.1	Solar Array Active Area Reduction .....	55
4.7.2	Shunt Regulator.....	55
4.7.3	PMAD .....	55
4.7.4	Battery .....	56
4.7.5	Further Mass Reductions.....	56
4.8	Mass evaluation.....	56
5	Chapter 5 .....	58
5.1	Sheath Theory .....	58
5.1.1	Plasma between two Walls.....	59
5.1.2	Pre – Sheath.....	60
5.1.3	Collisionless Sheath .....	61
5.1.4	The Bohm Sheath Criterion .....	62
5.1.5	Collisional Plasmas .....	64
5.2	Langmuir Probe.....	64
5.3	A Couple of Probes .....	67

6	Chapter 6 .....	69
6.1	Plume Interactions.....	69
6.2	Spacecraft charging.....	70
6.2.1	Arc-Discharge .....	72
6.2.2	Avoid Spacecraft Charging Effects.....	72
6.3	Schematic Model Introduction.....	74
6.4	Cathode .....	75
6.5	Spacecraft Chassis and Theory of the Floating Potential.....	77
6.6	Spacecraft and Solar Array .....	78
6.6.1	Linear Load Panel .....	82
6.6.2	Interconnects .....	83
6.6.3	Saturation Region.....	84
6.7	Thruster Body .....	85
6.8	Non-Linear Equations System .....	87
7	Chapter 7 .....	90
7.1	First step.....	90
7.2	Second Step.....	91
7.3	Third Step.....	92
7.4	Fourth Step.....	93
7.5	Fifth & Sixth Step .....	94
7.6	Plume Software Analysis .....	95
7.6.1	PICPlus Simulations.....	96
7.6.2	Max Solar Array Electron collection from High Power Thruster Plume..	99
7.7	Seventh & Eighth Step .....	100
7.8	Study on the Katz Constant.....	102
8	Future Works.....	104
9	Conclusions .....	107
10	Bibliography.....	110
	Appendix A .....	116
	CASE 1 .....	116
	CASE 2.....	117
	CASE 3.....	118

Appendix B .....	120
Appendix C .....	124
Code description .....	124
Part One .....	124
Part Two .....	124
Part Three .....	124
Matlab Codes .....	126
Matlab Codes in relation with PICPluS Study .....	129
Appendix D .....	132
Results tables .....	132
Appendix E .....	135
PICPluS Basic description .....	135
PICPluS features .....	136
Algorithms .....	136
Outputs .....	137
The Program .....	137

# Premessa

Da tempo ormai si ritiene che la propulsione elettrica sia una tecnologia fondamentale per il futuro dell'esplorazione spaziale.

I vantaggi nei consumi di propellente e i continui miglioramenti nelle prestazioni l'hanno resa una valida alternativa alla propulsione chimica. In particolare, l'uso di sistemi EP a bordo di satelliti di telecomunicazione geostazionari di nuova generazione porta a risparmi sostanziali nella massa del propellente.

La propulsione elettrica non si basa, in generale, sulla natura reattiva dei propellenti per dare energia al flusso, ma accelera il propellente per mezzo di sistemi elettrici di svariata natura.

Uno dei processi accelerativi più promettenti è quello della corrente di Hall. I propulsori ad effetto Hall rappresentano una soluzione versatile, grazie alla loro scalabilità e alle elevate prestazioni in termini di efficienza di spinta e impulso specifico. Usati fin dagli anni '60 per operazioni di station keeping a bordo di satelliti Russi, con il crescere della potenza disponibile i propulsori Hall stanno trovando sempre maggiore applicazione, riaccendendo l'interesse della comunità scientifica. In particolare, nell'arco dell'ultimo decennio, numerosi progetti sono stati avviati per lo sviluppo di sistemi di alimentazione con potenze superiori al centinaio di chilowatt.

Un'interessante applicazione di questi sistemi propulsivi (ad alta potenza) consiste nella realizzare di un veicolo di trasporto, uno space tug, che alimentato a celle solari permetta di portare un payload da orbite basse terrestri a orbite più alte per poi tornare indietro, fornendo un servizio "taxi" per satelliti o cargo.

La combinazione di propulsori ad effetto Hall e di tecnologia Direct Drive (collegamento diretto tra sistema propulsivo e pannello solare ad alto voltaggio) con i miglioramenti nel campo dei pannelli solari rendono possibile questa missione.

Questo studio vuol valutare come l'accoppiamento di diverse tecnologie all'avanguardia possa influire sulle architetture di sistema e sugli scenari di missione.

Nei primi capitoli si introduce brevemente il lettore ai concetti base della propulsione elettrica e della fisica del motore HT20k progettato da SITAEL. (Questo motore sarà la base di tutte le nostre simulazioni).

Studiati i vari vincoli e requisiti di uno space tug, definiremo la missione di trasporto e forniremo simulazioni preliminari per diversi sotto-casi. Svolgeremo nel dettaglio lo studio di una configurazione.

I capitoli successivi presenteranno l'analisi del problema del caricamento elettrostatico (charging) delle superfici del veicolo spaziale a contatto con il getto di plasma (plume) uscente dal propulsore.

Una schematizzazione del problema, dopo aver presentato la teoria della guaina (sheath theory), ci permetterà di scrivere un codice Matlab per arrivare a conoscere correnti e voltaggi sulle singole parti dello spacecraft, in modo da apportare modifiche alla configurazione e prevenire danni strutturali.

Lo studio è stato poi affiancato a simulazioni, attraverso codici numerici di tipo Particle-In-Cell (PIC), dell'andamento del getto di plasma, al fine di conoscere temperatura e densità locali.

Gli ultimi capitoli sono dedicati alle conclusioni e a suggerimenti per sviluppi futuri.

Le appendici riportano i programmi realizzati sulla base dei modelli proposti, alcuni esempi di sistemi dimensionati con questi programmi e le simulazioni svolte durante l'analisi della missione.

# Abstract

Electric propulsion has long been believed to be a key technology for the future of space exploration.

The advantages in fuel consumption and the continuous improvements in performance have made it a worthy alternative to chemical propulsion. In particular, the use of EP systems on new generation geostationary telecommunications satellites leads to substantial savings in the propellant mass.

The electric propulsion is not based, in general, on the reactive nature of the propellants to give energy to the flow, but accelerates the propellant by means of electric systems of various nature. One of the most promising acceleration processes is that of Hall current.

Hall effect thrusters represent a versatile solution, thanks to their scalability and high performance in terms of thrust efficiency and specific impulse.

Used since the 60s for station keeping operations onboard of Russian satellites, with the increase of available power the Hall engines are finding more and more application, they are rekindling the interest of the scientific community. In particular, over the last decade, numerous projects have been launched for the development of power systems with powers exceeding one hundred kilowatts.

One of the most interesting applications is to create a transport system that is powered by solar cells and allows a payload to be brought into higher energetic orbits by providing taxi service.

The combination of Hall Effect thrusters and Direct Drive technology with innovations in the field of the solar array makes this mission not only possible but also desirable.

This study aims to evaluate how the coupling of various cutting-edge technologies can influence system architectures and mission scenarios.

In the first chapters, the reader is briefly introduced to the basic concepts of electric propulsion and the physics of the HT20k engine designed by SITAEL. (This engine will be the basis of all our simulations).

Having studied the various constraints and requirements of a space tug, we will define the transport mission and provide preliminary simulations for different sub-cases. We will carry out a detailed study of a configuration.

The following chapters will present the analysis of the problem of electrostatic charging of the surfaces of the spacecraft in contact with the plasma plume coming out of the propeller.

A schematization of the problem, after presenting the sheath theory, will allow us to write a Matlab code to forecast currents and voltages on the individual parts of the spacecraft, so as to make changes to the configuration and prevent structural damage.

The study was then joined to simulations, through a numerical Particle-In-Cell (PIC) code, of the plasma plume, in order to know the local temperature and density.

The last chapters are dedicated to conclusions and suggestions for future developments.

The appendices show the programs realized on the basis of the proposed models, some examples of systems sized with these programs and the simulations carried out during the mission analysis.

# List of Figures

<b>Figure 1</b> Optimization of the value of the effective exit velocity to obtain the minimum mass of the propulsion system. For lower exhaust velocity, the advantage established by the propellant mass reduction is lost, while for higher values the mass of the power supply can become dominant, strongly affecting the total mass budget.....	8
<b>Figure 2</b> Guiding centre drift due to electric and magnetic fields.....	14
<b>Figure 3</b> Deflection of main electron drift direction due to collisional events (credit by [2]). .....	15
<b>Figure 4</b> A schematic side section of an axisymmetric Hall thruster of the SPT type is shown. The cross-section view is showing the main components: an extended insulator channel, showing the external cathode, the internal anode, the radial magnetic field and typical particle trajectories (credit by [9])......	16
<b>Figure 5</b> Typical architecture of an orifice hollow cathode. ....	17
<b>Figure 6</b> Scheme illustrating the general principle of a closed-drift thruster. The left part is an axial-radial ( $x,r$ ) view of the device while the right part is a radial-azimuthal ( $r,\theta$ ) view, showing the radial magnetic field and the Hall current (credit by [9]). ....	18
<b>Figure 7</b> Electrons become “trapped” in spiral paths (credit by [9]).....	19
<b>Figure 8</b> Schematic representation of the acceleration and ionization regions and of the radial magnetic field profile. ....	19
<b>Figure 9</b> HT20k mounted on the thrust stand for the first campaign (left), firing during characterization (right), (credit by [20]).....	21
<b>Figure 10</b> CAD drawing of the HT20k and HC60 (centrally-mounted), (credit by SITAEL).....	21
<b>Figure 11</b> Expected performance map HT20k (credit by SITAEL).....	23
<b>Figure 12</b> Relationship between T/P and specific impulse (credit by SITAEL). ....	24
<b>Figure 13</b> Orbiting Maneuver Vehicle with crew concept. ....	25
<b>Figure 14</b> Orbit Insertion.....	30
<b>Figure 15</b> Eutelsat 172 B.....	31
<b>Figure 16</b> Initial (left) and final (right) orbit in the GTO to GEO transfer (credit by [20]). .....	33
<b>Figure 17</b> OTIS simulation for GTO to GEO transfer. It is a three-dimensional transfer from GTO to GEO the visualization requires views from three views (X-Y, Y-Z, and Y-Z).	

The white portions of the plot are when the system is not thrusting as it is in shadow (credit by [29]).....	33
<b>Figure 18</b> Evolution of SEPTD MISSION spiral trajectory from LEO at 28.5 to geo, the geo to LEO at 0 deg. Top: oblique view, bottom: side view; illustrated with a higher thrust to power than realistic to reduce the number of spirals and make them visible. The upper part shows the spiral trajectory outbound leg in dark blue with red, the light blue is the spiral inbound. Total transfer time 10 months (credit by [26])......	36
<b>Figure 19</b> STK ideal spiral orbit result of the simulation.....	38
<b>Figure 20</b> Concept of propulsion assembly (credit by [27]). .....	45
<b>Figure 21</b> Typical solar electric propulsion mission schematic (credit by [35])......	47
<b>Figure 22</b> SEP tug concept base on ESPA ring (credit 29). .....	49
<b>Figure 23</b> General configuration (right), direct drive configuration (left).....	51
<b>Figure 24</b> The formation of plasma sheaths: (a) initial ion and electron densities and potential; (b) densities, electric field and potential after formation of the sheath (credit by [2])......	60
<b>Figure 25</b> Qualitative behaviour of sheath and pre-sheath in contact with a wall.....	61
<b>Figure 26</b> Definition of voltage and current for a Langmuir probe (credit by [2]). .....	65
<b>Figure 27</b> When the probe voltage is positive with respect to the plasma, electrons are accelerated to the probe, while the ions are repelled. The collected ion current is smaller and smaller as the probe voltage is increased. The maximum electron flux is given by the thermal flux which enters the sheath around the probe, hence, the electron current flattens at highly positive values of $VB$ , the so called electron current saturation ( $A$ ). It is customary to plot $I - V$ curves with $I_e$ positive and $I_i$ negative (credit by [50])......	66
<b>Figure 28</b> Electrostatic charging mechanism credit by [54]......	71
<b>Figure 29</b> Evaporation of polymer and metal due to discharge in electron-irradiated aluminized Kapton (credit by [54]). .....	71
<b>Figure 30</b> Reference scheme of the problem.....	74
<b>Figure 31</b> The thruster neutralizer hollow cathode generates a plasma typically 10 to 20 V above the cathode common (credit by [2]). .....	76
<b>Figure 32</b> Spacecraft chassis current collection. Potential with respect to S/C and with respect to space plasma (credit by [51])......	77
<b>Figure 33</b> Ion collection area is on S/C chassis and on the lowest side of the array. Plasma potential is indicated by the dashed horizontal line and the current loop is shown by the grey ellipse (credit by [51])......	79

<b>Figure 34</b> Charge transfer from neutral plasma plume of the thruster to solar array surface (credit by [56]).	79
<b>Figure 35</b> A simplified diagram of a Hall thruster system is shown. Note that the thruster body is connected to spacecraft chassis ground (credit by [51]).	79
<b>Figure 36</b> Linearly charged solar array.	82
<b>Figure 37</b> An idealized I-V curve. The red current is expanded 10X to show the ion current (credit by [50]).	85
<b>Figure 38</b> Current loop through thruster body closes in the plume plasma (credit by [51]).	85
<b>Figure 39</b> I-V curve on the thruster body, plotted with the Matlab code in Appendix C. When the potential difference between TB and plasma is zero the curve enters in the saturation region.	86
<b>Figure 40</b> Schematic model with current direction evaluation.	87
<b>Figure 41</b> Thruster body isolated. Cathode grounded with a potential difference respect to the plasma of 15 V (credit by [51]).	92
<b>Figure 42</b> In order top-down are shown the: Gmsh model in the far field environment, the mesh on the model of the tug and the model of HT20k near the solar panel.	97
<b>Figure 43</b> The computed plume in a clipped section of Tecplot evaluation on the surfaces of the elements of the mesh. Density decreases as we move away from the thruster (credit by SITAEL).	98
<b>Figure 44</b> The plume is computed 2D in terms of single (top) and double (down) charged ions distributions measured in number density (nd). $Xe^{++}$ are concentrated in the axial region of the plume (credit by SITAEL).	99
<b>Figure 45</b> Collection of electron current with extraction of local number density and temperature of the plasma.	102
<b>Figure 46</b> Future study on the beam stray current in different environment: spacecraft PPU in flight (top), spacecraft DDU in flight (middle), vacuum chamber (bottom).	106
<b>Figure 47</b> Tetrahedral schematic.	136
<b>Figure 48</b> Deposition of silver after one panel revolution in 3600s. Result of a simulation re-deposition of sputtered material - Tecplot.	137
<b>Figure 49</b> Main GUI window.	138
<b>Figure 50</b> Geometry of the thruster affection area obtained through the Gmsh geo file.	138
<b>Figure 51</b> An example of satellite model computed with Gmsh. Here the 2D mesh is visible.	139

**Figure 52** Computed number density (left) and axial speed (right) - Tecplot. .... 139

# List of Tables

<b>Table 1</b> Classification of the electric thrusters by accelerating method. ....	5
<b>Table 2</b> Performance of the HT20k development model up to 20kW.....	22
<b>Table 3</b> Major classes of potential space tug missions. ....	26
<b>Table 4</b> Initial parameter of a GTO – GEO mission transfer. ....	30
<b>Table 5</b> Information on STK model and simulator.....	37
<b>Table 6</b> Orbit raising LEO – GEO input data per STK. ....	38
<b>Table 7</b> Case 1. ....	39
<b>Table 8</b> Case 2. ....	39
<b>Table 9</b> Case 3. ....	39
<b>Table 10</b> Simulations Results. ....	41
<b>Table 11</b> Effects on the basic mission concept and key requirements. ....	44
<b>Table 12</b> Power generator data. ....	46
<b>Table 13</b> Strictly comparison (advantages and disadvantages) in the installation of a PPU or a DDU.....	52
<b>Table 14</b> Design impact of bus voltage on EPS. These data refer to a study carried out by Kerslake at the NASA Glenn Research Center [41] which analyzes a GEO spacecraft equipped with a 10 kW HET and systems at the base voltage of 28V.....	56
<b>Table 15</b> Input case for A and B resistances. Inf stay for 106Ω. ....	91
<b>Table 16</b> Input case for A and B power supply. ....	93
<b>Table 17</b> Summary of the different dry mass % for each subsystem in each case. ....	120
<b>Table 18</b> Case with 2 thrusters and 2 PPU. The base structure is the ESPA. In this configuration, only two tanks of propellant are necessary to perform also the return from GEO. ....	121
<b>Table 19</b> Case with 2 thrusters and 2 DDU. The base structure is the ESPA. In this configuration, three tanks of propellant are necessary to perform also the return from GEO. The mass benefit from Direct Drive configuration affects the component of the power and propulsion module causing the additional propellant to be less severe on the payload mass. ....	122
<b>Table 20</b> Six tons tug with 4 thrusters and 4 DDU. The base structure is the ESPA. In this configuration, 7 tanks of propellant are necessary to perform also the return from GEO. The mass benefit from Direct Drive configuration affects the component of the power and	

propulsion module causing the additional propellant to be less severe on the payload mass.  
..... 123

**Table 21** Results with plasma 0 V,  $\Delta V1 = 100 V$ ,  $\Delta A = 1100$ , CRP = -15V..... 132

**Table 22** Results with spacecraft grounded at 0 V,  $\Delta V1 = 100 V$ ,  $\Delta A = 1100$ , CRP = -15V..... 132

**Table 23** Results with plasma 0 V,  $\Delta V1 = 100 V$ ,  $\Delta A = 1100$ , CRP = -15V, Box A and B are power supply. .... 133

**Table 24** Results with plasma 0 V,  $\Delta V1 = 300 V$ ,  $\Delta A = 1100$ , CRP = -15V..... 133

**Table 25** Results with plasma 0 V,  $\Delta V1 = 100 V$ ,  $\Delta A = 110000$ , CRP = -15V. .... 133

**Table 26** Results with plasma 0 V,  $\Delta V1 = 300 V$ ,  $\Delta A = 110000$ , CRP = -15V. .... 134

**Table 27** Results with plasma 0 V,  $\Delta V1 = 100 V$ , with Picplus evaluation of I2, (\*)the last column is the second iteration..... 134

**Table 28** Results with plasma 0 V,  $\Delta V1 = 300 V$ , with Picplus evaluation of I2, (\*) the last column is the second iteration..... 134

# List of Acronyms and Abbreviations

AED	Advanced Electric (propulsion) Diagnostics
AOCS	Attitude and Orbit Control Subsystem
AS	Anode Supply (Main Supply)
AVUM	Attitude and Vernier Upper Mode
BC/DR	Battery Charge/Discharge Regulator
BOL	Beginning Of Life
BS	Battery System
CDH	Command Data Handling
D2 or DD	Direct Drive
DDCU	Converter Unit
DDT&E	Design, Development, Test & Engineering
DDU	Direct drive unit
Delta-V	Change in velocity (of spacecraft)
DRM	Design Reference Mission
EM	Electro Magnetic
EMIF	Electro Magnetic Interference Filter
E-M L1	Earth moon Lagrange point 1
EMS	Electro Magnets Supply
EOL	End of Life
EOR	Electric Orbit Rising
EP	Electric Propulsion
EPS	Electrical Power System
FCU	Fuel Control Unit
GEO	Geostationary Earth Orbit
GNC	Guidance, Navigation and Control
GTO	Geosynchronous Transfer Orbit
HEO	High earth orbit
HET	Hall Effect Thruster
HS	Heater Supply
HVB	High Voltage Bus

IKS	Igniter-Keeper Supply
ISP	Specific impulse (of EP thruster)
ISS	International Space Station
I/V	Current / Voltage
LEO	Low Earth Orbit
MEO	Medium Earth Orbit
MGSE	Mechanical Ground Support Equipment
OMV	Orbital Maneuvering Vehicle
PDU	Power Distribution Unit
PGS	Power Generation System
PiC	Particle-in-Cell
PMAD	Power Management and Distribution
PPU	Power Processing Unit
Ref	Reference Document
RPC	Remote power controller
RPOD	Rendezvous Proximity Operations and Docking
RVD	Rendezvous
SA	Solar Array
S/C	SpaceCraft
SDC	Step-Down Converter
SEP	Solar Electric Propulsion
SK	Station Keeping
SLA	Stretched Lens Array (Entech Technology)
SOA	State Of the Art
TB	Thruster Body
TCS	Thermal Control System
TTC	Tracking Telemetry and Command
TDM	Technology Demonstration Mission
TSD	Thruster Steering Device
TU	Thruster Unit
XFC	Xenon Feed Control

# Chapter 1

Introduction to space propulsion and presentation of some fundamental concepts of electric propulsion in order to provide a solid background.

## 1.1 Space Propulsion

The position and motion of a spacecraft on orbit can be determined by defining a state vector. By generating thrust, a space propulsion system allows the state vector of a spacecraft to be changed in accordance with an intended orbital manoeuvre. Nevertheless, whether or not a specific manoeuvre can be performed depends on the capabilities of the propulsion system onboard. As a result, a general overview of the concepts of propulsion allows defining figures of merit to compare different propulsion technologies and to eventually highlight the reasons why electric propulsion systems are suitable options for a wide variety of mission scenarios.

Consider the one-dimensional flight of a rocket-propelled spacecraft as a function of time  $t$  with mass  $M(t)$  and velocity  $v(t)$  in the absence of gravitational forces. From conservation of momentum, the acceleration of the spacecraft results from the application of the thrust  $T$ , given by the product of the mass flow rate and effective exhaust velocity relative to the rocket  $c$  [m/s] of the propellant

$$M(t) \frac{d}{dt} v(t) = T = \dot{m}c. \quad 1.1$$

The expulsion of propellant reduces the mass of the spacecraft over time. The spacecraft mass is

$$M(t) = M_o - \dot{m}t. \quad 1.2$$

Considering  $M_o$  the initial mass of the spacecraft and the mass flow rate constant.

After the substitution of Eqn.1.2 into the following differential equation,

$$M \frac{dv}{dt} = - \frac{dM}{dt} c. \quad 1.3$$

The delete of time differentials and the integration over some initial to final spacecraft velocity and mass lead to an expression for the ratio of final to initial vehicle mass, as a function of the velocity increment  $\Delta V$  and  $c$ .

$$\frac{M_f}{M_o} = e^{-\frac{\Delta V}{c}} \quad 1.4$$

This formula can be turned to know the necessary velocity increment of a rocket (once the mission is established  $\Delta V$  is the goal to reach in order to be able to accomplish that mission), and the exit velocity (often used as a first-order criterion in space vehicle design)

$$\Delta V = c \ln \frac{M_o}{M_f}. \quad 1.5$$

Also known as the rocket equation, this equation was first derived by Konstantin Tsiolkowsky in 1895. The term Delta-V is the magnitude of velocity increment due to the ejection of a certain mass of propellant

$$M_{prop} = M_o - M_f.$$

where the final mass is the sum of the structural mass and the payload mass

$$M_f = M_s + M_{pl}.$$

The propellant mass for a specific mission or manoeuvre is then

$$\frac{M_{prop}}{M_o} = 1 - e^{-\frac{\Delta V}{c}}. \quad 1.6$$

Eqn.1.5 illustrates the impact of exhaust velocity on the mass ratio of a spacecraft. High effective exhaust velocity allows to considerably reduce the amount of propellant that must be brought on board, in this resides the main advantage of the electric propulsion with respect to the chemical one.

Another important parameter is the  $T_s$  [ $N/W$ ] thrust per unit of power

$$T_s = \frac{T}{W_{in}} = \frac{\dot{m} \cdot c}{W_{in}}.$$

For a given  $T_s$  and knowing the available power on board ( $W_{in}$ ), the thrust range within which the thruster can operate is obtained immediately and consequently the time necessary to accomplish certain maneuvers or missions.

To characterize the performance of a thruster is better to introduce two more parameters. The total impulse [Ns] delivered to a spacecraft is the thrust integrated over time and is often used to report rocket lifetime.

$$It = T\Delta t = \int_0^{t_b} T dt \quad 1.7$$

The other parameter is the specific impulse[s]; it is the total impulse per total consumed propellant weight. This definition refers to is a kind of average specific impulse, whereas  $I_{sp}$  is an instant parameter. The common definition of  $I_{sp}$  is: thrust per propellant consumption rate (considering constant thrust and flow rate are to be able to bring thrust and mass flow rate out of integral)

$$I_{sp} = \frac{\int_0^{t_b} T dt}{\int_0^{t_b} \dot{m} g_0 dt} = \frac{T\Delta t}{\dot{m} g_0 \Delta t} = \frac{It}{M_{prop} g_0} = \frac{c}{g_0}. \quad 1.8$$

Here  $g_0$  is the gravitational acceleration at sea level and  $t_b$  is the burning time.

Specific impulse is a measure of efficiency in terms of propellant consumption.

If the thrust and mass flow rate is constant over the thrust time, specific impulse reduces to the latest equality in Eqn. 1.8, in this case, it is roughly one-tenth of the effective exit velocity.

Using the new definition of the exhaust velocity

$$c = \frac{T}{\dot{m}} = I_{sp} \cdot g_0$$

is possible to rewrite the rocket equation (Eqn.1.5)

$$\frac{M_f}{M_o} = \exp\left(-\frac{\Delta V}{I_{sp} g_0}\right). \quad 1.9$$

In order to accomplish a mission the higher the  $I_{sp}$ , the lower the total propellant mass will be. With the purpose to reduce the needed propellant mass and therefore increase the payload mass, this relation takes to a simple conclusion that the thrust should be achieved via a high exhaust velocity, rather than a high ejection of mass.

## 1.2 Electric Propulsion

The increasing use of electric propulsion for many space applications derives from the capacity of the thrusters to provide very high effective exhaust velocity, even of an order of magnitude greater than the one provided by chemical propulsion<sup>1</sup>.

These kinds of thrusters cannot be used for launcher stages, but they have the possibility of multiple re-ignitions (pulsed mode) and can operate at constant thrust or vary the thrust on demand over relatively wide intervals, which allows them to have applications for tasks such as stationkeeping, orbit rephasing, and orbit transfer.

R. G. Jahn in [1] defines electric propulsion as:

*“...the acceleration of gases for propulsion by electrical heating and/or by electric and magnetic body forces.”*

The way through which the acceleration of the flow is obtained, as well as the systems for generating the required electric power, can be different from each other. They have been tested on ground and in space since the 1960s, and a wide variety of system types is available now.

A classification, adopting the previous definition, is used in order to better understand this variety. The thrusters are divided by the means in which the working fluid is accelerated up to the exhaust velocity.

*Electrothermal propulsion:* acceleration of a propellant gas by electrical heat addition by means of a resistance and expansion through a convergent/divergent nozzle.

*Electrostatic propulsion:* acceleration of an ionized propellant gas by the application of electric fields.

*Electromagnetic propulsion:* acceleration of a plasma<sup>2</sup> by the application of both electric and magnetic fields that generate a Lorentz force.

In Tab.1 the engines according to the subdivision are shown. Descriptions of each thruster type, flight data, and development trends can be found in [2] [10].

---

<sup>1</sup> The main limitation of the electric engines resides in the relation depicted in Eqn.1.9, with high specific impulses; the thrust levels obtainable are very low, leading to very long transfer times.

<sup>2</sup> A detailed definition of plasma will be provided at the beginning of Chapter 5.

---

*Electrostatic*

---

- Ion Bombardment
  - Colloid ion
  - Contact ion
  - Field Emission (FEEP)
  - Microwave or Radiofrequency ion
  - Plasma separator ion
  - Radio-isotopic ion
  - Hall effect:
    - o SPT
    - o TAL
- 
- 

---

*Electromagnetic*

---

- Magnetoplasmadynamic
    - o Steady state
    - o Self-field & Applied-field
  - Pulsed plasma
  - Helicon plasma
  - Inductive pulsed plasma
  - Electron-cyclotron-resonance
  - Variable specific-impulsive plasma
- 
- 

---

*Electrothermal*

---

- Resistoject
  - Arcjet
    - o DC vs AC vs Pulsed
  - Electrothermal hydrazine
  - Microwave electrothermal
  - Pulsed electrothermal
- 
- 

**Table 1** Classification of the electric thrusters by accelerating method.

In a chemical rocket, the dependence on internal energy limits the maximum specific impulse to about 450 s, whereas in electric rockets specific impulses of over 17,000 s have been obtained in laboratory.

Unlike a chemical rocket, which relies on the stored internal energy in the molecular bonds of its propellant, in an electric spacecraft, the energy is obtained from an external power

source and it is used to generate electric and magnetic fields, necessary for ionization and acceleration of the plasma.

The known sources of energy are solar arrays (photovoltaic cells), gas turbines, nuclear reactors, batteries, radioisotope generator and fuel cells. It is correct to underline that only a few of them are today feasible alternatives.

Since external power sources are required, the high-specific impulse capabilities of electric propulsion come at the expense of power and mass of the power supply. This “penalty” puts an emphasis on maximizing the specific power [ $W/kg$ ] (or minimizing the specific mass [ $kg/W$ ]) of power supplies.

For missions that require a high  $\Delta V$ , where therefore the mass of the propellant has a greater importance than the mass of the engine, it will be necessary to try to maintain the values of  $c$ . It is therefore seen that the objective is not simply to maximize the effective exhaust velocity (as in the chemical propulsion), but to determine the value of  $c$  which optimizes the mission overall.

Depending on the mission and due to the power system, for electric thrusters an  $c_{opt}$  exists which minimizes the total mass (the sum of the propellant mass and power supply mass).

$$M_{tot} = M_g + M_{prop}$$

It is possible to demonstrate that by setting the partial of the  $M_{tot}$  to zero. To do that is necessary to rewrite any mass as a function of the thrust  $T$ .

For a given mission, the exhaust beam power is the measure of how efficient the propellant is accelerated.

The power needed for the thrust under the condition of constant thrust and mass flow rate can be written as,

$$P_{thrust} = \frac{1}{2} \dot{m} c^2 = \frac{1}{2} \frac{M_{prop}}{t_b} c^2 = \frac{Tc}{2}. \quad 1.10$$

Electric thrust efficiency understood as the ratio between jet power and electric power used indicates the efficiency in the conversion of provided electric power  $P_{electric}$  to exhaust kinetic power

$$\eta_T = \frac{P_{thrust}}{P_{electric}} = \frac{\dot{m} c^2}{2W_{in}} = \frac{Tc}{2W_{in}} = \frac{T^2}{2\dot{m}W_{in}}.$$

In turn, electric power can be expressed

$$P_{electric} = \frac{Tc}{2\eta_T} \quad 1.11$$

from this, it is straightforward to rewrite the expression for electric thruster effective beam velocity

$$c = \sqrt{\frac{2\eta_T P_{electric}}{\dot{m}}}$$

Considering the mission performed with a constant thrust level  $T$  and for a certain firing time  $t_b$ , and constant mass flow rate (or constant exhaust velocity) the total mass of the propellant used is

$$M_{prop} = \dot{m} \cdot t_b = \frac{Tt_b}{c}$$

Power system mass scales monotonically with the power supplied. The  $\alpha$  coefficient is the specific mass of the power generator [ $kg/W$ ]<sup>3</sup>.

$$M_g = \alpha P_{electric} = \alpha \frac{P_{thrust}}{\eta_T} = \frac{\alpha Tc}{2\eta_T} = \frac{\alpha \dot{m}c^2}{2\eta_T} = \alpha \frac{c^2}{2\eta_T t_b} M_{prop} \quad 1.12$$

With an assigned thrust  $T$ , the mass of the energy source is proportional to  $c$ , therefore increasing the exhaust velocity, the mass of propellant is reduced but the mass of the engine is increased. In Fig. 1 this concept is depicted.

The optimal  $c$  is acquired replacing  $M_{prop}$  and  $M_g$  in Eq. 1.13.

$$M_{tot} = M_g + M_{prop} = \frac{\alpha Tc}{2\eta_T} + \frac{Tt_b}{c} \quad 1.13$$

$$\frac{\partial M_{tot}}{\partial c} = \frac{\alpha T}{2\eta_T} - \frac{Tt_b}{c^2} = 0$$

---

<sup>3</sup> It can also be found that  $\alpha$  is defined as specific power, that is, the electrical power obtainable per unit mass of the energy source, we can then determine the mass of the energy source required as  $\alpha = P_{electric}/M_g$ .

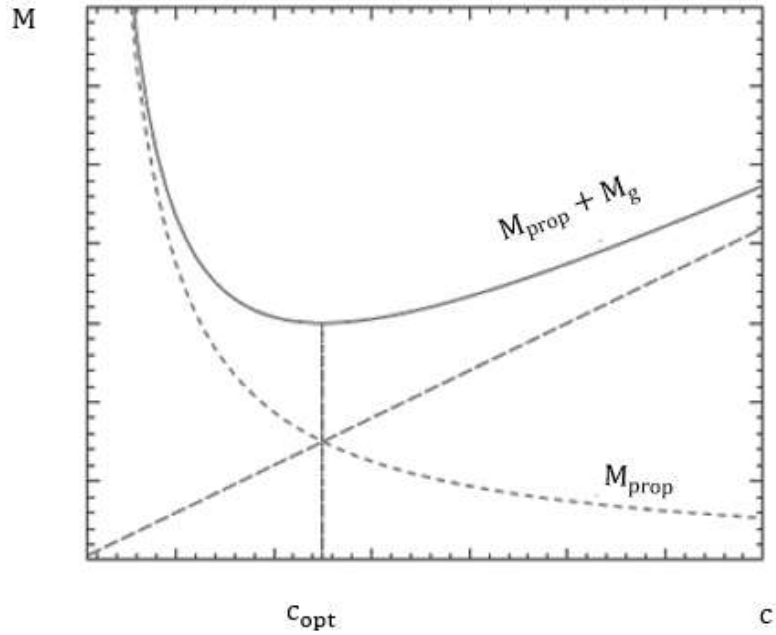


**Figure 1** Optimization of the value of the effective exit velocity to obtain the minimum mass of the propulsion system. For lower exhaust velocity, the advantage established by the propellant mass reduction is lost, while for higher values the mass of the power supply can become dominant, strongly affecting the total mass budget.

$$(c)_{opt} = \sqrt{2\eta_T \frac{t_b}{\alpha}} \approx g_0 (I_{sp})_{opt} \quad 1.14$$

Consequently, an optimal specific impulse also exists.

$$(I_{sp})_{opt} = \frac{(c)_{opt}}{g_0}$$

### 1.3 Electrostatic Propulsion

Currently, the most promising technology for future missions is represented by Hall Effect thrusters, which allows relatively high thrust efficiencies and thrust density.

Some authors classify Hall Effect thrusters (HET) as electromagnetic propulsion systems, rather than electrostatic.

Therefore, it is worth analyzing the basic concepts of electrostatic thrusters before moving on to the detailed HET description relied on Chapter 2.

Their technology can be briefly explained presenting some basic concepts: electron bombardment, neutralization, and Hall current.

### 1.3.1 Electron Bombardment

Bombardment produces positive ions by striking neutral propellant atoms in a discharge chamber with thermionically excited electrons.

Heating of the axial cathode produces thermionic emission of electrons at a low amperage voltage, which discharges toward the anode. A magnetic field is typically applied in the discharge chamber to reach a higher collision probability.

In some configurations grids held at different potentials near the exhaust port allow the plasma to be accelerated to exhaust velocities.

### 1.3.2 Neutralization

These systems use positively charged ions as the primary working fluid.

After the ions reach the exit of the thruster they are neutralized by a spray of electrons from a neutralizer cathode to prevent a potential difference from pulling ions back to the engine.

### 1.3.3 Hall Current

If any electromagnetic accelerator is operated at low plasma density or with a high magnetic field, the current passing through it will diverge from the alignment with the electric field applied, to acquire a component in crossed electric and magnetic fields ( $\vec{E} \times \vec{B}$ ) direction as a consequence of the known "Hall effect". Low-density Hall-current accelerators exploit this effect by providing channel and field geometries that block the plasma electrons into a nearly collisionless cross-stream drift, which leaves the positive ions free to accelerate downstream under a component of the applied electric field. Such devices are hybrid electrostatic-electromagnetic accelerators.

Electrostatic propulsion uses a high voltage electrostatic field to accelerate ions to large exhaust velocities. By choosing a potential difference  $V_D$  is possible to design the value of the ion velocity after they reach the exhaust,

$$u^+ = c = \sqrt{\frac{2qV_D}{\mu}}$$

where  $q$  is the electric charge constant.

To maximize the output speed it is appropriate to adopt ions with a low mass/charge ratio ( $\mu/q$ ), a similar choice leads to low propellant masses.

The ions generated by the thruster create a current. This is the electric beam current and it is given by the product.

$$I_{beam} = \dot{m} \cdot \frac{q}{\mu} \quad 1.15$$

from which is deduced the mass flow, which allows the rewriting of the thrust

$$T = \dot{m}c = I_{beam}\sqrt{2V_D}\sqrt{\mu/q}.$$

From this equation, it can be seen that in order to obtain a high thrust with the same electric current and voltage, it is advisable to adopt ions at a high charge to mass ratio.

The current tendency is to use of the xenon because it does not lead to operational problems despite being heavy and expensive, but the search for alternative propellants is always current.

# Chapter 2

This chapter is an immersion inside the Hall thruster technology: story, physics and design are here exposed. Section 2.3 gives a brief overview of the basic physics principles about charged particles motion, while Section 2.4 describes how they contribute to thrust generation.

## 2.1 Development History of Hall Thrusters

The Hall propulsion was independently studied in the United States and the Soviet Union in the late 1950s and early 1960s. Deriving from research on magnetrons and other cross-field plasma sources, the first working devices were reported by Americans which, however around 1970, decided to focus on the development of gridded ion thrusters.

The concept of an engine based on the Hall Effect was improved in the Soviet Union with the first in-flight tests.

URRS developed two types of Hall thrusters<sup>4</sup>:

- Stationary Plasma Thruster (SPT)<sup>5</sup> at Design Bureau Fakel.
- Thruster with Anode Layer (TAL) at the Central Research Institute for Machine Building (TsNIIMASH).

The first design of the SPT is largely due to the work of A.I. Morozov and the first model to operate in space was the SPT-50, aboard the Russian satellite *Soviet Meteor* in December 1971.

With the fading of the Cold War, Russian Hall thrusters were first mounted on a western satellite. On October 3, 1998, the Naval Research Laboratory STEX spacecraft flew the Russian D-55 anode layer thruster for military research.

---

<sup>4</sup> Both types lay on the same basic principles for ionizing and accelerating the propellant. In SPT, the plasma acceleration zone is more extended and enclosed in a ceramic channel while in TAL, the same zone is narrower, the anodes are located downstream and the ion production region is positioned more externally.

<sup>5</sup> Also called magnetic layer thruster (MLT) but that convention will be avoided to differentiate thrusters of this type from those marketed by Fakel (e.g. the SPT-100 where the number after the initials indicates the outer diameter of the acceleration channel).

The first Hall thruster to be used outside Earth orbit as a primary propulsion system was on the SMART-1 mission of the European Space Agency (ESA). On September 28, 2003, the spacecraft started its journey to the Moon using a Snecma PPS-1350-G thruster, a derivative of the SPT-100.

The first American Hall thruster to fly in space was the Busek BHT-200 on TacSat-2 technology demonstration spacecraft. The first flight of an American Hall thruster on an operational mission was the Aerojet BPT-4000, which launched on the military Advanced Extremely High-Frequency GEO communications satellite.

In the past forty years, over two hundred missions were performed with Hall thrusters without ever having registered a failure on orbit. In the meantime, Europe and Japan have emerged with their own versions of the technology qualified for commercial uses.

## 2.2 Application and Present Capabilities

Since pioneering flights (on Soviet satellites for telecommunication, weather control or military surveillance), HETs have been typically used for station keeping and orbit maintenance tasks, orientation and attitude control and correction manoeuvres.

The use of non-Keplerian orbits and the continuous electricity generation progress allow to include among the tasks also the primary propulsion. After the success of the SMART-1 mission, new applications are expected for electric propulsion systems especially in the field of interplanetary missions.

Low-power Hall thrusters are well suited for drag compensation of observation satellites that operate on a low-altitude orbit. Also with the rapid spread of microsattellites and nanosatellites, the demand for small, reliable and good-performing thrusters is increasing. High-power Hall thrusters (higher than 5 kW) have long been considered as a leading solar electric propulsion (SEP) candidate because of the high performance and reliability, reduced consumption and the possibility of grouping together several units in a single propulsion block (clustering). The wide range of applications includes manned Mars scenarios, reusable tugs for LEO to GEO transportation and journeys towards asteroids. Recent studies [12] have also identified high power Hall propulsion systems as a valid technology for various space telescope missions that require near-space to libration point transfers or other delicate manoeuvres which before were entrusted exclusively to chemical propulsion.

The evolving mission requirements and higher onboard power availability drive the expansion of the EP power range, particularly for ion and Hall thrusters.

Recent works have demonstrated Hall thruster operation at power levels as low as 100 W and as high as 100 kW.

A Hall engine typically operates at 50 - 60% of the thrust efficiency and provides a specific impulse from 1000 to 2000 seconds and powers from 1 to 5 kW.

In ground tests, the range of the specific impulse is wider, between 500 s and 5000 s, with thrust-on-power ratios of 10-70  $mN/kW$ . These values depend mostly on the kind of propellant that is used for the test. As the mass of ionized gas is low, total thrust is low (from tens of micro-Newton up to 3 N).

## 2.3 Particle Motion and Hall Parameter

In this section is presented a brief description of the motion of a charged particle of mass  $m$  and charge  $q$  in the presence of an electric ( $\vec{E}$ ) and magnetic fields ( $\vec{B}$ ). Here concepts and factors will be introduced that allow us to explain the acceleration process. For a complete explanation, we recommend [2] [3] [9].

The classical theory shows that the motion of a particle subject to the action of a magnetic field is a uniform circular motion in the plane perpendicular to the field lines. In this case, we introduce a frequency (called “cyclotron frequency”) defined as

$$\omega_c = \frac{qB}{m}.$$

The radius of the circular orbit is called “Larmor Radius” and its value is

$$r_L = \frac{mv_{\perp}}{qB}, \tag{2.1}$$

where  $v_{\perp}$  is the velocity perpendicular to the magnetic field lines.

In the particular case in which an electric field  $\vec{E}$  is applied orthogonal to  $\vec{B}$  the particle is subjected to a drift motion characterized by drift velocity

$$\vec{v}_d = \frac{\vec{E} \times \vec{B}}{B^2}.$$

The overall result is that the ion has a cycloidal trajectory. An accelerated motion in the direction of  $\vec{B}$  overlaps this cycloidal motion.

When an ion moves along the direction of the electric field, it accelerates and its Larmor radius increases, when the ion moved against the field, the Larmor radius decreases. The guiding centre drifts perpendicularly to both  $\vec{E}$  and  $\vec{B}$  as shown in Fig. 2.

Electrons have a smaller Larmor radius than ions due to their lower mass.

The behaviour of an assembly of particles can be described by the Boltzmann equation. A description in terms of average behaviour can be sufficient for a global collective behaviour of the various components. This is usually done by taking the first three velocity moments of the Boltzmann equation, thus obtaining the mass, momentum and energy conservation equation for each species. These equations are generally called fluid equations. Once they are combined with the Maxwell equations and with appropriate constitutive relations, the fluid equations provide a complete description of the collective behaviour. In other words, even in the presence of a bulk flow, a particle has a  $\vec{E} \times \vec{B}$  drift.

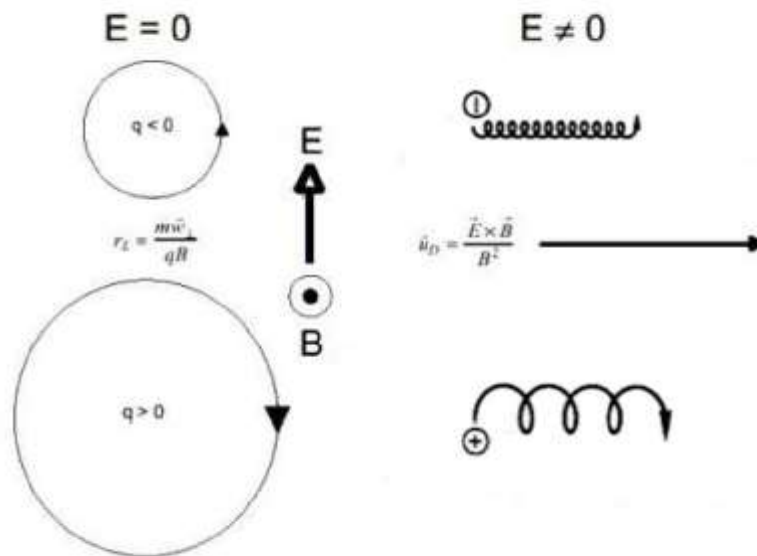


**Figure 2** Guiding centre drift due to electric and magnetic fields.

In a real plasma, collisions occur between particles. Collisions disturb the helical motion of the particles, by forcing them to diffuse in the  $\vec{E}$  direction; this is because every time an electron collides with a heavy particle (an ion or a neutral), it is supposed to stop and then is accelerated again by the electric field.

Fig. 3 shows the drift direction modified by collisional events.

The angle  $\theta$  is a function of collisional ( $\nu_c$ ) and cyclotronic ( $\omega_c$ ) frequencies according to the following expression

$$\Omega = \tan \theta = \frac{\omega_c}{\nu_c} = \frac{qB}{m\nu_c}. \quad 2.2$$

Where  $\Omega$  is called ‘‘Hall parameter’’ and is a measure of the collisional behaviour of the plasma<sup>6</sup>.

The higher the  $\Omega$ , the more ideal the process of ion acceleration is. It is possible to reach that with a strong magnetic field.

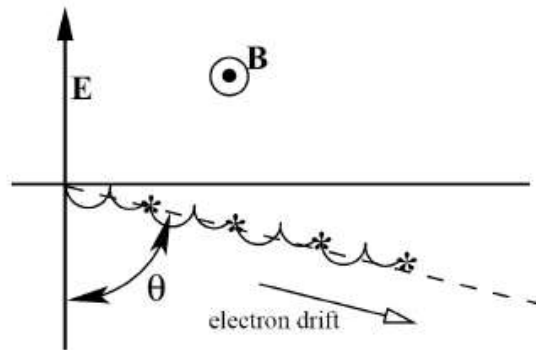


**Figure 3** Deflection of main electron drift direction due to collisional events (credit by [2]).

## 2.4 General Scheme and Acceleration Process

Hall thrusters<sup>7</sup> involve a diversification in terms of size and performance, but roughly, a great number of them shares the same configuration presented in Fig. 4.

The thruster assembly consists of several elements.

The *anode* is a metallic annular assembly, which provides uniform propellant distribution through a series of small orifices. It is located at the upstream end of a coaxial dielectric channel that confines the discharge.

---

<sup>6</sup> The Hall parameter is an indication of how many oscillations occur around the magnetic field during the characteristic time absent from collisions.

<sup>7</sup> Hall-effect thrusters (based on the discovery by Edwin Hall) are sometimes referred to as Hall thrusters or Hall-current thrusters.

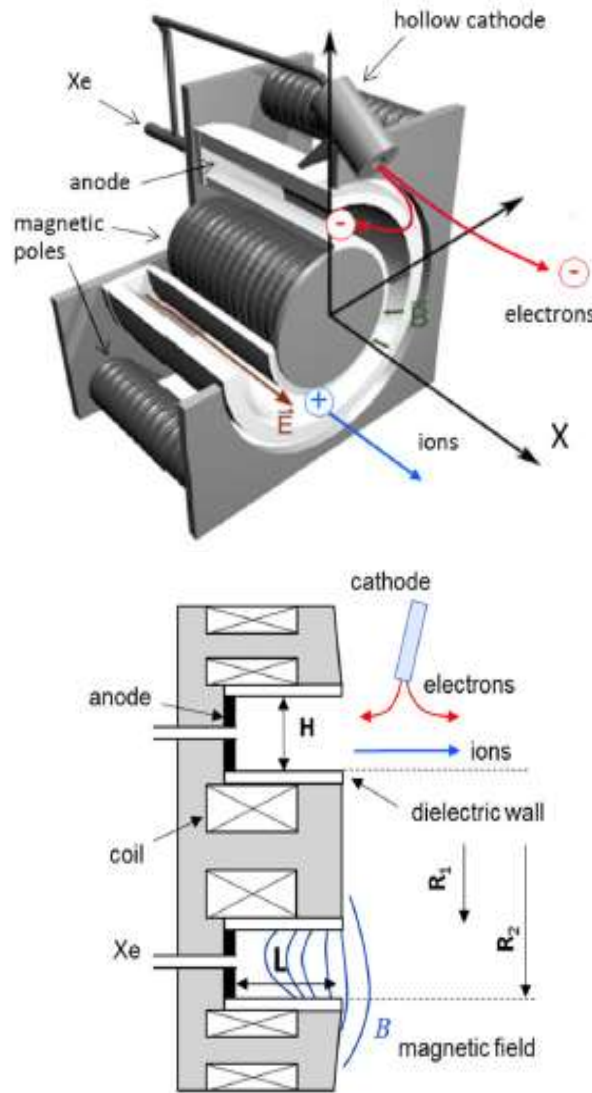


**Figure 4** A schematic side section of an axisymmetric Hall thruster of the SPT type is shown. The cross-section view is showing the main components: an extended insulator channel, showing the external cathode, the internal anode, the radial magnetic field and typical particle trajectories (credit by [9]).

The anode gas injector and the propellant feeding line are biased at a potential  $V_d$  (usually 300V) and are isolated from the inlet gas supply line through electrical isolators.

The *discharge chamber* is an annular “U” shaped canal made of ceramic Boron Nitride and Silicon Dioxide mix ( $BNSiO_2$ ), which separates the thruster body from the plasma. It is in this channel that the acceleration process takes place.

The *magnetic system* consists of internal and external electromagnetic coils (a set of solenoids is schematically shown in Fig. 4), and of a magnetic permeable circuit to produce the radial magnetic fields ( $\vec{B}$ ) in the discharge chamber.

*Ferro-magnetic screens* drive magnetic field lines approximately in order to have a strong radial field with a small axial component near the channel exit.

A variety of alternative *propellants* such as argon, krypton, bismuth, zinc, magnesium, oxygen and iodine can be used, but most Hall thrusters operate on the noble gas xenon, which is inert, heavy (high atomic weight), and has a low ionization potential.

The *quasineutral plasma* is created within the discharge chamber by means of the electron bombardment of the neutral xenon gas. The cathode provides the electrons.

Typically one or two of *hollow cathodes* (schematized in Fig. 5) are located outside the thruster body. Each of this includes:

- a getter that traps all the oxygen in the xenon before feeding the high temperature;
- a heating coil used during the start-up phase to bring the device to the necessary temperature;
- a thermal emitter which, when heated to a high temperature, enables electron emission;
- thermal screens positioned around the high temperature cathode core;
- an igniter used to initiate the discharge.

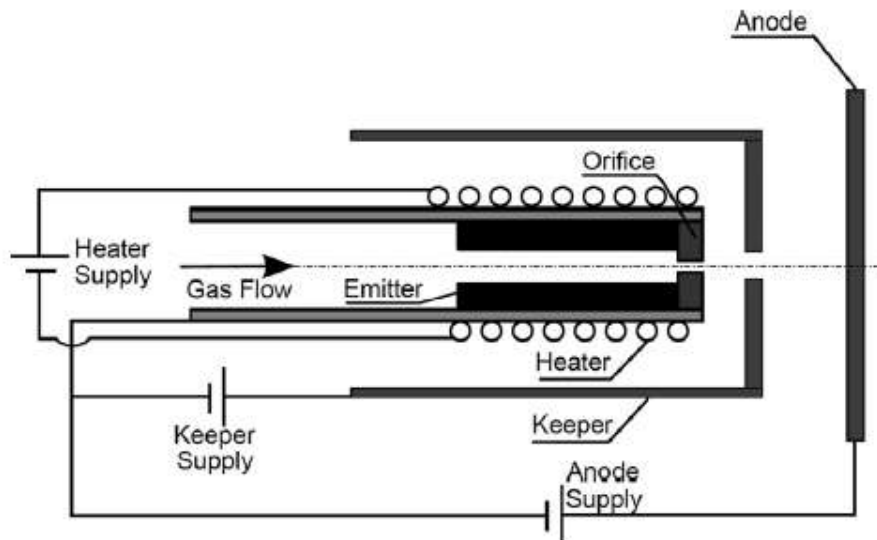


**Figure 5** Typical architecture of an orifice hollow cathode.

## 2.4.1 Generation of the Thrust

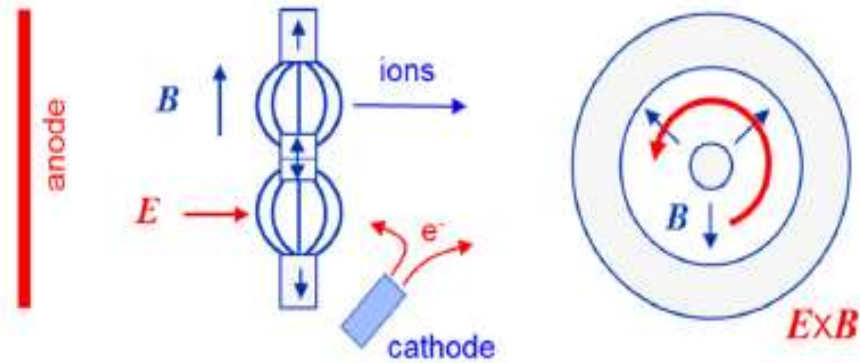


**Figure 6** Scheme illustrating the general principle of a closed-drift thruster. The left part is an axial-radial ( $x,r$ ) view of the device while the right part is a radial-azimuthal ( $r,\theta$ ) view, showing the radial magnetic field and the Hall current (credit by [9]).

The acceleration principle is based on a significant drop in electronic mobility at the channel's exit.

The cathode emits free electrons that are attracted in part by the discharge potential  $V_d$ . These electrons, once in the discharge chamber, are subjected to the radial magnetic field (of about 0.01–0.03 T) and become “trapped” in spiral paths, as depicted in Fig. 7. They are subjected to the previously described azimuthal drift in the crossed radial magnetic field and axial electric field<sup>8</sup>.

The electrons then induce an electric field that presents a peak at the exit of the channel, and during their motion, electrons collide with the neutral gas particles injected into the chamber.

This results in the creation of positively charged xenon particles (and electrons)<sup>9</sup>.

The strength of the magnetic field is sufficient to decrease the electron conductivity but it does not significantly affect the trajectory of the ions due to their greater Larmor radius (Eqn. 2.1). The ions are directly accelerated by the axial electric field and are thus expelled from the thruster<sup>10</sup>.

---

<sup>8</sup> The crossing of these fields create the Hall current from which the device gets its name.

<sup>9</sup> This is the ionization process, which gives the characteristic luminescence to the engine.

<sup>10</sup> The corresponding induced local axial electric field has two main effects. First, it drives a high electron azimuthal drift. Second, it accelerates ions out of the channel, which generates the thrust.

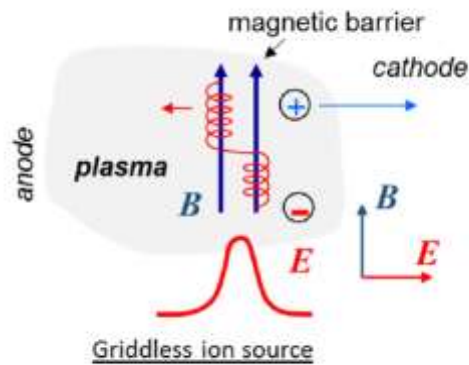


**Figure 7** Electrons become “trapped” in spiral paths (credit by [9]).

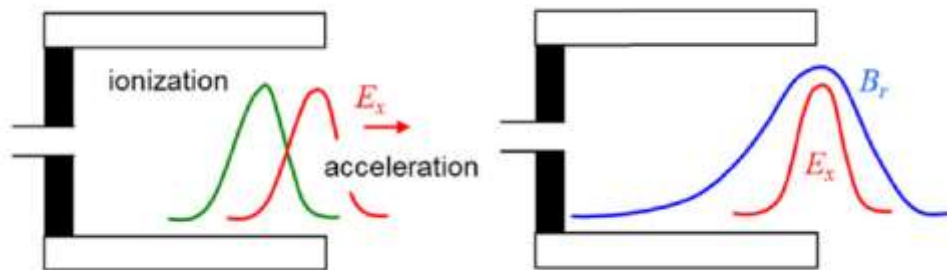


**Figure 8** Schematic representation of the acceleration and ionization regions and of the radial magnetic field profile.

The axial electric field profile is schematically shown in Fig. 8 together with the ionization rate and radial magnetic field profiles.

The ion beam is neutralized by a fraction of electrons emitted from the hollow cathode, creating a plasma plume. Hence, the hollow cathode is used to provide both the electrons for the main discharge plasma and the neutralizing electrons.

## 2.4.2 Internal Currents

Collisions with walls or other particles allow some of the electrons to drift towards the anode.

This current that passes through the anode is the *discharge current*  $I_D$ .

It is the same current that goes out from the cathode  $-I_D$ .

Most of the electrons supplied by the cathode must neutralize ( $I_N$ ) the ion beam outside the channel, which in turn creates a current  $I_{beam}$ .

$$I_{beam} = J_{i+} = \frac{\dot{m}_+ q}{m_+} \quad 2.3$$

$$I_N = -I_{beam}$$

Another part of the electrons (20-30%) goes into the channel (driven by the potential fall between anode and cathode) and contributes to the ionization of the propellant. This electron current, called trigger current, is indicated with  $J_e = I_{trig}$ .

The discharge current is the sum of these two currents.

$$-I_D = I_{trig} + I_N \quad 2.4$$

The discharge current that enters the anode is composed of the  $I_{trig}$  and of the electrons that are formed during the ionization process. This last one is equivalent to the current  $J_{i+}$ . The relation in Eqn. 2.4 can be used to describe also the “positive” discharge current

$$I_D = I_{trig} + J_{i+}. \quad 2.5$$

## 2.5 HT20k Performance



**Figure 9** HT20k mounted on the thrust stand for the first campaign (left), firing during characterization (right), (credit by [20]).

In Europe, development activities on high-power Hall thrusters are currently being performed by SITAEL, which in the past three years designed, manufactured and tested a first development model of the HT20k, a 20 kW-class Hall thruster together with a high current hollow cathode, the HC60.

The HET design is based on the extensive experimental and theoretical heritage of SITAEL in the field of electric propulsion. The main project drivers of the HT20k were compact design, high veratility in terms of specific impulse and power levels, reduced mass and volume and capability of having acceptable performance with alternative propellants.

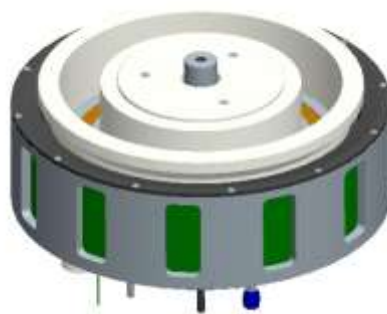


**Figure 10** CAD drawing of the HT20k and HC60 (centrally-mounted), (credit by SITAEL).

The HT20k thruster design incorporates magnetic coils, screens, pole extensions, and a discharge channel made of boron nitride.

A theoretical scaling methodology has been used to size the HT20k and for the preliminary evaluation of its performance map.

The geometry was obtained by means of broadly validated scaling methodologies, in which the SPT-100 was assumed as reference thruster thanks to its high efficiency in a wide range of operating conditions<sup>11</sup>.

The hollow cathode has been designed to be coupled with HT20k. The cathode, called HC60, was designed to provide currents up to 60 A at mass flow rates between 2 to 6 mg/s. The cathode lifetime is expected to be higher than 10<sup>4</sup> hours. The cathode mass, is about 450 grams without cables<sup>12</sup>.

In particular, at a discharge power of 20 kW, the thruster has a thrust efficiency higher than 60%, about 1 N of thrust, a specific impulse of 2500 s and a total impulse greater than 30 MNs.

The range of performance can be seen in Tab. 2, as whereas the expected performance map is presented in Fig. 11-12.

*HT20k characteristics*

<i>Parameter</i>	<i>Value</i>
Outer channel diameter	254 mm
Voltage	300 V – 1000 V
Discharge Power	10 kW – 20 kW
Anodic Efficiency $\eta$	up to 68%
Thrust $T$	300 mN – 1100 mN
Specific Impulse $I_{sp}$	2000 s – 3800 s
$\frac{\eta}{\eta_{SPT-100}}$	~1.25

**Table 2** Performance of the HT20k development model up to 20kW.

<sup>11</sup> The channel walls of the HT20k were made of BN-SiO<sub>2</sub>. The same material showed a good behaviour in terms of secondary electron emission and resistance to environmental testing.

<sup>12</sup> The cathode has a lanthanum hexaboride (LaB<sub>6</sub>) emitter, selected based on its features of longer expected lifetime and lower evaporation rate at the required discharge current despite higher work function compared to the traditional dispenser emitters.

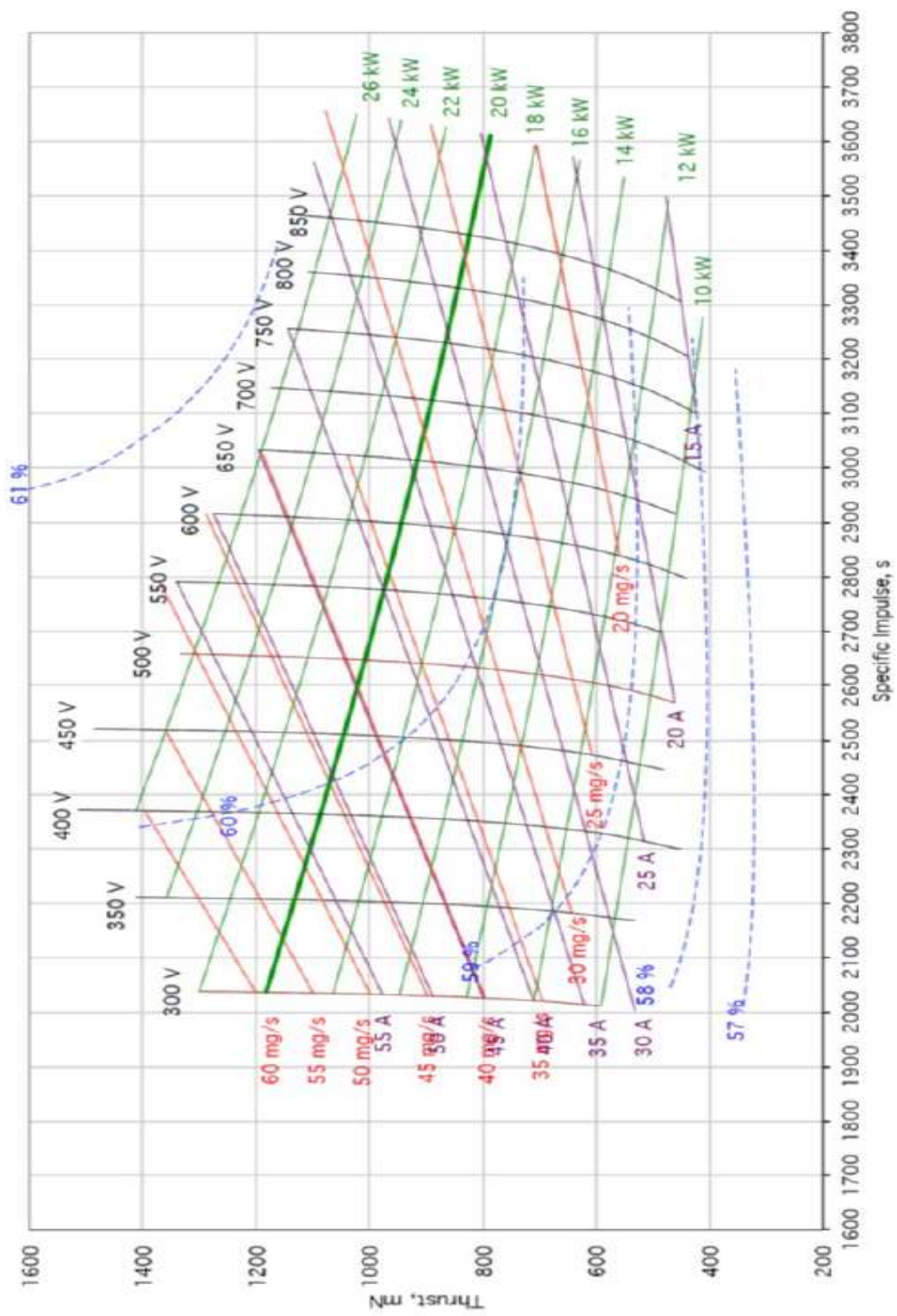
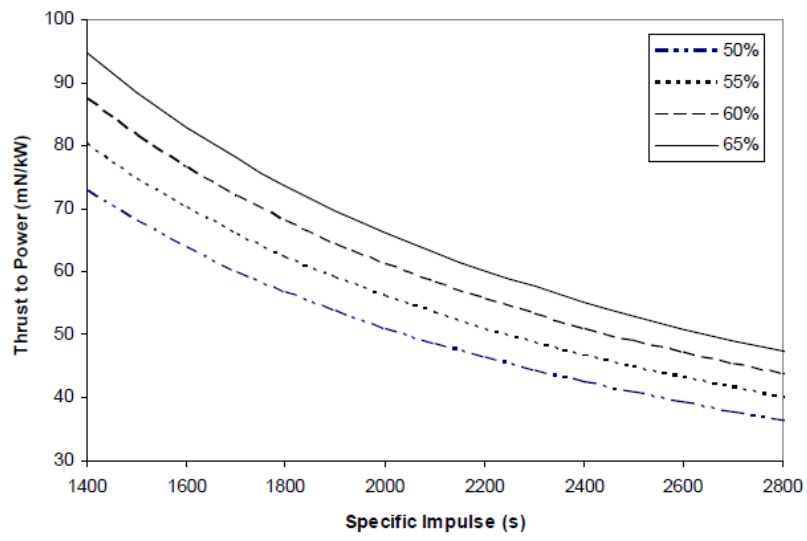


Figure 11 Expected performance map HT20k (credit by SITAEI).



**Figure 12** Relationship between T/P and specific impulse (credit by SITAEI).

## Chapter 3

As mentioned in the Abstract the mission we are considering is that of a space tug moved via electric propulsion. Before penetrating the merits of the mission, for the sake of comprehension is useful to describe and underline what are the properties of a space tug, the problems that we have to face with this kind of architecture, and the goal that a S/C like this could achieve. This will help us to trace the profile of an ideal mission, to study it and to simulate it.

### 3.1 Space Tug Surroundings

The *space tug* was first conceived in the post-World War II era as a support vehicle for a permanent Earth-orbiting space station. It was used as the title for science fiction novel by Murray Leinster published in 1953.



**Figure 13** Orbiting Maneuver Vehicle with crew concept.

In subsequent years a reusable space tug was studied by NASA as part of a reusable Space Transportation System. NASA's Orbital Maneuvering Vehicle (OMV) had a different design. The OMV's role would have been a reusable space vehicle that would service uncrewed orbital platforms, for repair or to retrieve satellites.

With the term "space tug", we commonly refer to a vehicle that is designed to rendezvous with a specific target (cargo or satellite), make an ascertainment of its current position, orientation and operational status, capture it, and then move it to a different orbit with a subsequent release.

This OMV can be treated as an upper stage on the launch vehicle, an orbital transfer vehicle part of the mission, or both.

This transportation vehicle is a propulsive secondary payload adapter that can simplify many of the mission needs, such as power and propulsion, to enable payloads and/or spacecraft to remain smaller, simpler and often with a lower cost. The advantage of separating the requirements from either the launch vehicle or the payload is that each section can focus on a single element of the mission. The launch vehicle provider can focus on low-cost access to a few identified orbits, the spacecraft can focus on the needs of the payloads rather than the capability to achieve a given orbit, and the tug can act as a bridge between these two system elements by focusing on the orbit adjustment.

The major cases for which a space tug can be useful are listed in Tab. 3.

Projects mentioned therein differ by missions and technical parameters but their analysis allows identifying common features [14]. General tendencies in the development and technical problems have to be studied and resolved.

<i>Identified problems</i>	<i>Missions</i>
1. Satellite reaching suboptimal orbits.	1. Rescuing.
2. Heavy payload transfer to GEO and beyond.	2. Taxi service.
3. Demand uncertainty for constellations.	3. LEO constellation reconfiguration.
4. National security.	4. On-demand military satellite manoeuvring.
5. Satellite lifetime limitations and retirement.	5. GEO satellite retirement boost maneuver.
6. Crowding, collisions.	6. Selective orbital debris removal.
7. Running out of supplies.	7. Refuelling/ resupply.
8. Servicing (maintenance).	8. Repair.

**Table 3** Major classes of potential space tug missions.

## 3.2 Tug Properties

In 90's cost-inefficiency was the reason why most space tug projects were abandoned. *Flexibility* and *reusability* are the keys to mitigate the costs of an OMV over a range of missions. However, these two requests are not easy to accomplish, as they require timeliness, good mating capabilities and high Delta-V range.

The transfer time for many missions listed in Tab. 3 can be months, regardless of the type of strategies or technologies we adopt. The idea of having one “universal” tug that can cover the entire Near-Earth space and perform many types of tugging missions in sequence (without refuelling) is not a viable option. Evidently, multiple round-trips between different orbits would not be possible without refuelling and maintenance.

The time in which the transportation service will be operational will, therefore, be much lower than the response time. To lower the response time, we should consider the use of a family of smaller and simpler tugs that operate locally.

Other specific requirements to be stressed besides the flexibility concerns the good mating capabilities. This performance metric is driven by the degree of autonomy and control used for grappling a target and the tender's hardware complexity. The sophistication in the mating capability drives mass and cost.

In addition, the rendezvous manoeuvres need an adequate propulsion system, then more thrusters and propellant onboard.

High Delta-V are achieved with high  $I_{sp}$ . It is necessary to manage mass and propellant consumption by selecting the optimal propulsion technology (electric, chemical or hybrid). A change in each of these variables produces a different architecture in the trade-space. However, the discriminating factor is the exponential increase of the fuel fraction with linearly growing Delta-V requirements. This could lead to design a “one-way trip” instead of a reusable tug.

A number of recent technological trends warrant a fresh look to briefly presented problems. For large Delta-V manoeuvres, the overall thrust level becomes important to minimize the transfer time, for both radiation and time to revenue considerations. Therefore, high power solar electric propulsion (HP-SEP) is suggested<sup>13</sup>.

The concept of SEP-based transportation vehicle coupled with Hall Effect Thruster gives transfer capabilities to both large and small payload [18] [25] [29].

Electric Orbit Raising (EOR) mission is the ideal candidate to evaluate the malleability of the HP-SEP.

---

<sup>13</sup> For high power, we mean higher than 20 kW of available power.

### 3.3 Electric Orbit Raising

It is easy now to define the purpose of an OMV. Once injected in LEO orbit, the tug has to exploit the electric propulsion to reach high altitude orbits such as MEO, GEO, HEO or even L2 orbits and, after unloading the payload, it has to return to the starting orbit. It is also possible to extend the mission. Instead of turning back, the tug can go to new orbits or stay in a place of destination and perform removal service<sup>14</sup> of dying satellite or debris. The platform payload could be either a satellite or a cargo module<sup>15</sup>.

The usefulness of having a satellite (telecom for example) as a payload of the OMV would be to lighten its weight. It would remove the encumbrance of a primary propulsion system that would become unused once finish the transfer and reached the target orbit.

With the reduction in launch mass that full electric orbit raising allows, regular missions above 10 kW with lower launch costs (i.e. including Ariane lower position or Falcon 9), or extremely powerful missions can be offered with payloads of typically 15kW/1500 kg for (i.e. including the Ariane upper position).

High power electric propulsion systems have a cost such that electric satellites are rather more expensive than their chemical counterparts are. There are also some constraints related to the EOR phase, the severity of which is related with the duration. This means that electric orbit raising pays off when the reduction in launch cost or additional mission capabilities more than compensate for the extra cost, deferred revenues and other constraints.

A key element, then, is the use of reliable solutions that keep overall system costs under control and reduce the duration of orbit raising.

There are two possible orbit-raising strategies with electric propulsion if we aim for a geostationary orbit (they will be described in detail in the next sections).

- GTO (Geo Transfer Orbit) – GEO (Geosynchronous Earth Orbit).
- LEO (Low Earth Orbit) – GEO.

In both, major problems are due to the prolonged duration of the trip. Many electric propulsion systems, in fact, require times to GEO of more than six months due to low thrust.

---

<sup>14</sup> At the end of operational life, geostationary spacecraft should be placed in a disposal orbit that has a perigee at least 300 km above the geostationary orbit. If tugging services are available, GEO satellites do not have to use their own propellant to move to such a graveyard orbit, thus lengthening their effective design lives. Estimates of the amount of “wasted” lifetime for GEO satellites vary between six months to two years.

<sup>15</sup> In this case, the mass of the cargo container counts.

The high power Hall thruster lifetimes and the solar array degradation strongly limit the operational life of the reusable tug.

In Eclipse, commonly the thrusters are turned off. The continuous re-ignition after the shadow zones fatigues the engine, which is designed to withstand a limited number of cycles. This is combined with problems due to temperature switch and occultation.

Higher levels of radiation due to several months through Van Allen belts<sup>16</sup> are also a concern.

The first type of EOR (GTO-GEO) is safer because it exceeds the altitude of 20000 km in relatively short times (less than two months) and there the particle density is not so high.

For the second type of transfer, the repeated transitions through the Van Allen belt is a more serious problem because it takes more time.

Fortunately, there are multiple solar array technologies under development that, with minimal loss of conversion efficiency, could lead to the needed specific power and radiation tolerance [35].

To achieve faster EOR, as long as the cost remains reasonable, more powerful thrusters or more numerous thrusters are used. Another option is to consider a mix of chemical propulsion for the first part of orbit raising, followed by EOR for the remaining part (orbit topping).

We now focus on the description of the two mission strategies we have mentioned.

### 3.4 GTO – GEO

A very high power HET could be used in large GEO platforms ( $\geq 5000kg$ ) to perform GTO to GEO transfer. The transfer orbit is accomplished by a wide range of missions, especially those with chemical propulsion and it consists of an elliptical trajectory (typically called Hohmann transfer). Tab. 4 collects few data referring to the whole mission. After deciding the launch site and the vector rocket (i.e. Atlas II, Falcon 9, Ariane 5...), the mission starts when the upper stage of the rocket places the spacecraft in a less inclined elliptical orbit with the apogee above geosynchronous orbit and the perigee just above the proton radiation belts, as shown in Fig. 14.

---

<sup>16</sup> Van Allen belts: they are two internal and external, the first stable and the second unstable and composed of high-energy electrons. They are in a band extended to 65 degrees north and south of the celestial equator. The first band ranges from 1000 to 6000 km, but can also be found in LEO at 200 km. The outer band passes from 10000 to 65000 km with a very high density between 14000 and 19000 km.

<i>Features</i>	<i>Details</i>
GTO	185 ÷ 400 km to 37576 km (respectively perigee and apogee altitude).
Eccentricity	~ 0.73
Radius apoapsis (TO = GEO)	42158 km after circularization maneuver.
Inclination	From 28.5 to 0 depending on the launch site.
Transfer duration (one way)	5/6 months in average (45 days with chemical to accomplish the Hohmann transfer).
Delta-V (one way)	2.8 ÷ 3 km/s

**Table 4** Initial parameter of a GTO – GEO mission transfer.

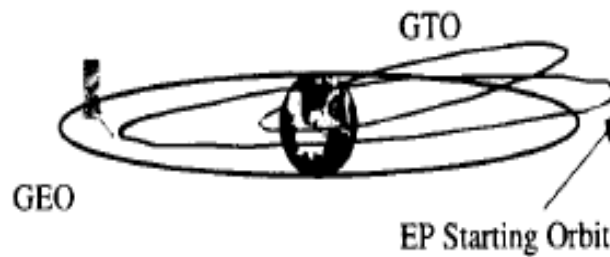


**Figure 14** Orbit Insertion.

Once in GTO, after an initial check of all the onboard systems, spacecraft starts the orbit raising thus limiting radiation exposure. This phase consists in a continuous thrust strategy, initially along the velocity vector, later thrusting perpendicularly to the position vector, except during the eclipses (the maximum eclipse lasted about 2h 15min), when the engine is switched off.

Analysis of this type of manoeuvres is not easy and completely different from the chemical approach. Specific software uses Edelbaum equations or simplifications of these, like Pollard's equations, to optimize and define the manoeuvres<sup>17</sup>.

---

<sup>17</sup> The fundamental strategy for the change of plans at low thrust is also described in [22] [23] with further details about Pollard and Edelbaum approximation and steering solutions.

The same studies have been done for the SMART-1 mission and for recent satellites that rely on electric propulsion to reach GEO. Most of them are telecommunication satellites based on LORAL SSL 1300, Alphabus SES or Eurostar E3000 platforms.

Examples of full EP satellites are Eutelsat 115 West B, Eutelsat 117 West A and Eutelsat 172B<sup>18</sup>. The latter, equipped with a cluster of SPT140D Hall thrusters, is the biggest one and holds the record of complete EOR in 4 months [19].

Under many aspects, it represents a remarkable result not achievable with chemical propulsion.



**Figure 15** Eutelsat 172 B.

---

<sup>18</sup> Eutelsat 172 B is based on the Eurostar 3000 European platform (with HETs) and is was launched in 2017 on Ariane 5 lower position. The mass at launch was about 3500 kg for a maximum power available of 13 kW. The EP system will be used to perform the EOR, NSSK/EWSK, momentum damping, station relocation and final re-orbitation.

For better understanding these aspects, a general problem is presented that has already been studied through the in-house (SITAEL) SATSlab software.

The results are here compared with NASA's software OTIS [29]. Both these programs are capable of calculation of difficult thrusting strategies for different mission profiles. SATSlab is dedicated to the complete analysis of spacecraft status during low thrust missions, including the interaction of orbital and attitude dynamics, onboard power production and subsystem energy consumption (see Fig. 16).

The OTIS software provides plots of the transfers that can be used to visualize it.

The software is able to compute the thrusting strategy as well as the eclipse time when the thruster/s would be switched off. Last, the software is also able to simulate the atmospheric drag, the effect of earth oblateness and third body perturbations (see Fig. 17).

Input parameters are introduced considering the European Ariane 5 ECA as launcher. It is able to put 9300 kg in a Geosynchronous Transfer Orbit (GTO) of 250x35786 km with 6 degrees of inclination. Moreover, the final GEO orbit, with  $i = 0$  and  $r_a = 42164$  km was imposed<sup>19</sup>.

The Delta-V using an impulsive manoeuvre is calculated considering a Hohmann transfer with a plane change occurring at the apogee  $r_a$ . The propellant mass is estimated using the Tsiolkovsky equation (Eqn. 1.6) with a specific impulse of 320s. As results, with an initial spacecraft mass of 6500kg, more than 2450 kg of propellant are needed for GTO to GEO orbit raising using chemical rockets.

In the light of comparison, thrust levels of 1N and a specific impulse of 2500 s are compatible with the orbit raising of large electric platforms now available on the market. Considering no third body effects, the total transfer time is 169.5 days with the thruster/s operating for 3978 hours resulting in 584 kg of propellant consumed. The great difference in propellant mass can be exploited in increasing the payload fraction or decreasing the total mass of the spacecraft while keeping the same payload mass. The latter option seems to be encouraging in terms of transfer time using low thrust electric propulsion.

---

<sup>19</sup> The tug reaches an altitude of 35758 km that is equivalent to the semi-major axis of the 42765 km orbit when the circularization is ended by subtracting the terrestrial radius (6371 km).

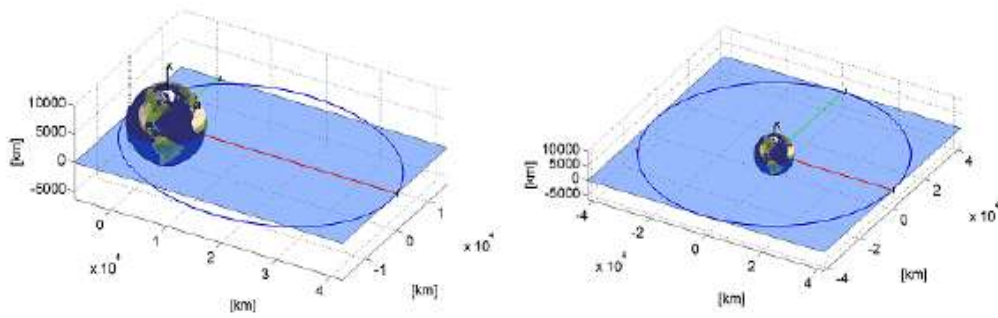


**Figure 16** Initial (left) and final (right) orbit in the GTO to GEO transfer (credit by [20]).

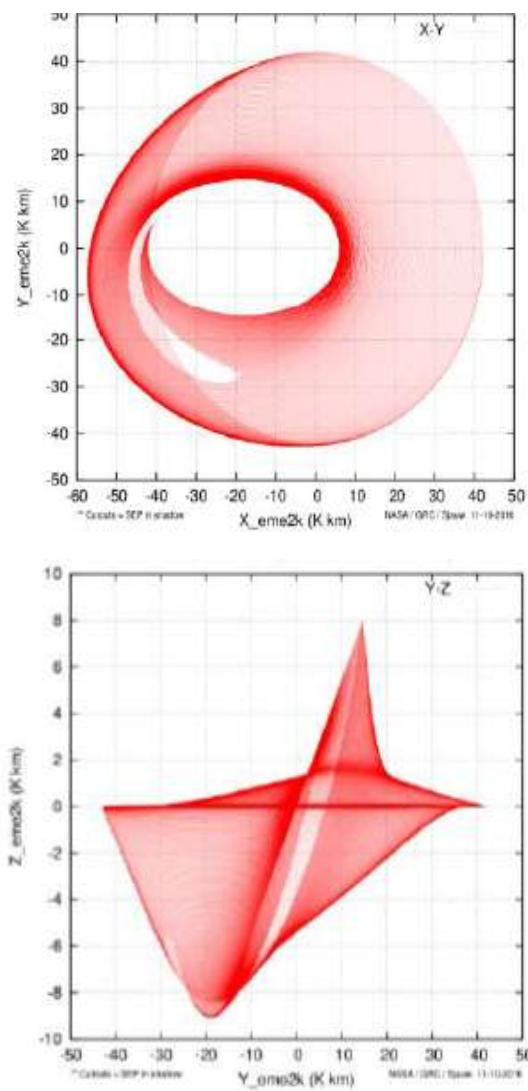


**Figure 17** OTIS simulation for GTO to GEO transfer. It is a three-dimensional transfer from GTO to GEO the visualization requires views from three views (X-Y, Y-Z, and Y-Z). The white portions of the plot are when the system is not thrusting as it is in shadow (credit by [29]).

### 3.4.1 GTO to GEO Tug

A typical GEO spacecraft will be launched into GTO and then use an onboard chemical propulsion system to circularize the orbit (reduce eccentricity) and reduce inclination (possibly near zero degrees).

On a geo satellite using only chemical propulsion, and weighing six tons at launch, roughly two tons of propellant (fuel and oxidizer) are needed for initial orbit raising (three to five maneuvers performed in about one week) and 1 ton is needed for station keeping (small periodic maneuvers all along several years of mission). If one or both types of manoeuvre are performed, using electric propulsion, less propellant is needed and accordingly, the satellite is lighter. The gain is significantly higher when both orbit raising and station keeping are done with electric propulsion, compared to when only station keeping uses electric propulsion [19].

An intermediate OMV specifically designed for this type of transfer and tasks would allow a further mass gain for a simpler primary spacecraft.

The primary propulsion system after one week into GEO is often not used again, it seems a reasonable solution separate it from the spacecraft. This would not only reduce the amount of propellant onboard but it would avoid larger spacecraft structure increasing in mass and cost, no longer worsening on processing facility, test chamber, and transportation system sizes.

## 3.5 Spiral LEO – GEO

The same considerations regarding mass gain are also valid for the other type of EOR. In this, the achievement of a GEO occurs through the continuous growth of geocentric circular orbits starting from LEO altitudes (between 185 and 400 km). Clearly, this type of spiral manoeuvres is slower than GTO and therefore even more dangerous (spending more time in hostile areas of space). The required Delta-V is 4.6 km/s for one way and 6.2 km/s if we consider a return in LEO (possible rendezvous manoeuvres are considered negligible).

Moreover, the spacecraft that have been tested to date are small ( $\ll 5000$  kg), it is a manoeuvre suitable for low-weight cargo spacecraft without urgency to arrive at the target orbit. A tug could also be suitable for this type of EOR.

The idea is to use a cheap launcher such as VEGA or adding an electrical kick stage to a conventional architecture chemically propelled (a shared launch) to carry the tug into orbit. Once launched in LEO and acquired an ideal payload in the same orbit (via V-bar approach) the OMV would begin a slow spiral manoeuvre at very low eccentricity, inclinations

between 6 and 0 degrees with the  $r_a = 42158 \text{ km}$ , and then come back to LEO after delivering the payload in GEO.

The times considering round trip are around 12 months with the use of low power engines. With the use of HP-SEP considerable reductions in times could be achieved.

Times that depend on a multitude of factors such as the date of departure, the eclipses, the thrust to mass ratio, the inclination of the orbit and the various perturbations that can be encountered. It is therefore difficult to have correct estimates when we try to calculate the preliminary duration of the whole mission.

We face the same complications on the orbital propagations faced in previous simulations. Lots of programs are used for this kind of mission details evaluation: SEPSPOT, the NASA Glenn Variant of the Solar Electric Control Knob Setting Program by Optimal Trajectories (SECKSPOT), The Mission Analysis Low-Thrust Optimization (MALTO) program, Spacecraft N-Body Analysis Program (SNAP), and Copernicus [28] [29].

In [26] [27] a baseline mission, which includes two spiral transits through the radiation belts (Fig. 18), is analyzed using these tools. Minimum Delta-V to perform a geocentric orbit transfer can provide the mass fraction that is combined with flow rate calculations and duty cycle estimates for trip-time approximations. Are presented also the exact duration for a low thrusting strategy LEO – GEO using HET and a deep analysis of eclipse frequency and duration. A large number of trades cases and point designs have been analyzed for requirements development, system sizing, and concept of operations definition.

The range of tools is appropriate for geocentric optimization, interplanetary transits, low-thrust spirals, and N-body analysis.

However, all of them present a much-refined model and a computational cost beyond the purpose of this work. Besides, a full N-body calculation is usually not performed for trajectory optimization.

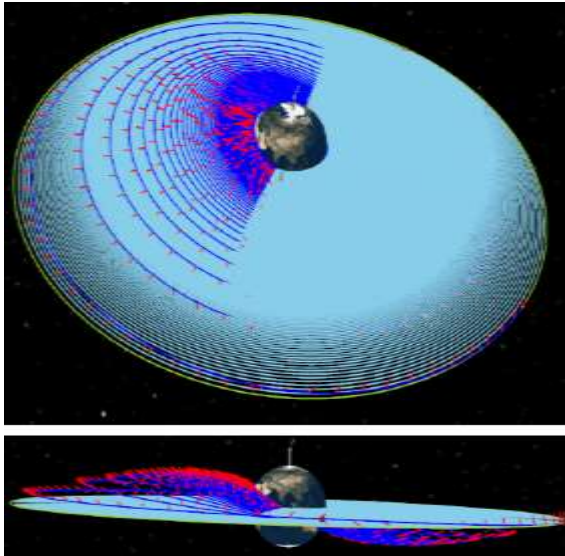


**Figure 18** Evolution of SEPTD MISSION spiral trajectory from LEO at 28.5 to geo, the geo to LEO at 0 deg. Top: oblique view, bottom: side view; illustrated with a higher thrust to power than realistic to reduce the number of spirals and make them visible. The upper part shows the spiral trajectory outbound leg in dark blue with red, the light blue is the spiral inbound. Total transfer time 10 months (credit by [26]).

### 3.5.1 STK Study

We propose here the examination of the second type of EOR with the software STK [21]. Systems Tool Kit (*STK*) is the premier software for providing four-dimensional modelling, simulation, and analysis of objects from land, sea, air, and space, developed by *AGI*.

We have availed ourselves of the help of two tools in particular:

- Space Environment and Effects Tool (SEET) designed for use by spacecraft designers, analysts, and operators to evaluate the effects of the space environment on their spacecraft.
- Space Event Generator (SEG) allows non-expert operators to quickly develop accurate, physics-based scenarios of common space events, from single object manoeuvres to complex, linked, multi-object interactions, using simple, GUI-based operator workflows.

More specifications are inserted in Tab. 5.

Nevertheless, it is fair to say that STK is not the perfect software to analyze SEP missions. The results provided would, therefore, have to be taken into consideration keeping in mind the actual constraints placed to facilitate convergence and lighten the computational cost, and the effective limitations of the program.

The transportation trajectory is mainly driven by the control gravity field of the Earth, but several others orbital perturbations might significantly modulate the time and even the effort ( $\Delta V$ ) devoted to bringing each satellite to its slot. Examples of this are higher order harmonics of the Earth gravity field, Sun and Moon gravity pool (3<sup>rd</sup> body problem), Sun radiation pressure and atmospheric drag.

As far as we are concerned, we will only take into account two bodies (Earth and spacecraft), adding perturbations due to Earth oblateness (J2), but plane changes and steering strategies will be ruled out from our analysis.

All the critical issues and requirements due to hypothetical RDV manoeuvres and mating phases are avoided. We neglect also the solar array degradation and the decrease of available power with distance from the Sun.

The eclipse periods, which would be present especially in the early phases of this hypothetical mission, will be taken into account neither. In fact, the topic should be analyzed by evaluating the power budget.

Thrusters, that normally operate while the Space Vehicle is in the Sun, here are always on. The values of variable vehicle acceleration in eclipses were considered as neglected. However, observations on eclipses phase are collected in Section 3.5.3 at the end of the chapter.

All this afflicts above all the estimate of the duration of the transfer. For this reason, we opted for a simplified mission to analyze, in order to make the results as less as possible divergent from those of a “real” mission.

Propagator model used	Earth_HPOP_Default_v10
Model of instabilities	Astrogator
Maneuver Direction Specification	Thrust Vector (updated during manoeuvre)
Number of manoeuvres	1
Number of propagations	1
Max iterations before the stop	500

**Table 5** Information on STK model and simulator.

Therefore, we analyze a one-way transportation mission of a TUG that starts from orbit LEO and arrives in GEO. The mission launches into a 400 km and 0-degree orbit, a likely orbit for a staging location or departure orbit for a SEP tug.

During all operations, the space vehicle orientation is maintained such that the electric thrusters are pointed along the velocity vector (the tug has to perform no orbital plan change) while the single-axis of articulated solar arrays parallels the orbit normal and the arrays stay sun-pointed.



The optimization of the  $I_{sp}$  has been put aside; the engine in each configuration is set to produce the maximum possible thrust with the purpose of spending as less time as possible in the Van Allen bands. It was also decided to study the advantages and changes due to a configuration in Direct Drive (DD) of the OMV and to see how much these two technologies (engine and configuration) could be advantageous once combined.

PPU (eff = 95%)	
Power	23,75 kW
HET number	2 (only 1 working)
Thrust at 23 kW	1,1 N
T/P	47 mN/kW
$I_{sp}$	2800 s
Efficiency	60%
Current	50 A
Mass flow	50 mg/s
Potential	550 V

**Table 7** Case 1.

DD (eff = 100%)	
Power	25 kW
HET number	2 (only 1 working)
Thrust at 23 kW	1,45 N
T/P	63 mN/kW
$I_{sp}$	2000 s
Efficiency	60%
Current	55 A
Mass flow	60 mg/s
Potential	300 V

**Table 8** Case 2.

DD (eff = 100%)	
Power	50 kW
HET number	4 (only 2 working)
Thrust at 23 kW	2,9 N
T/P	63mN/kW
$I_{sp}$	2000 s
Efficiency	60%
Current	55 A
Mass flow	60 mg/s
Potential	300 V

**Table 9** Case 3.

### *Case 1*

To do this we have defined three different architectures, each with a specific thruster operating point. The three operative points, described in Tab. 6, 7 and 8 respectively, define the three case studies.

The architecture is that of a small tug (under 3000 kg) not in DD configuration. Consider using the maximum throttle available during the trip with an installed PPU with 95% yield affecting the onboard power. The thrust is thus limited. The high specific impulse value suggests us reduced consumption but higher travel times. The data of the operating point of the engine used for the first simulation are in Tab. 7.

### *Case 2*

The architecture is that of a small tug (under 3000 kg) in DD where the 300 V grounded thruster is connected directly to the solar array at 300 V too. The thrust is considerably increased according to the engine performance map (in Section 2.9). Consider using the maximum throttle available, thanks to the DD we can use all the available power (set at 25kW). Times are reduced but the lowering of the specific impulse leads to an increase in the necessary propellant. The data of the operating point of the engine used for the second simulation are in Tab. 8.

### *Case 3*

To evaluate the complete extension of the advantages of the DD configuration and of the High Power Hall thrusters, this configuration brings the maximum weight of the space tug and payload to 6 tons. Available power and number of Hall engines are doubled, as well as the thrust. It is the only case in which two high-powered engines work at the same time. Usually for missions of this type is not recommended a single engine (even if at high power), it is preferable to use a cluster of smaller engines. The data of the operating point of the engines used for the third simulation are in Tab. 9.

To start the simulation it is also necessary to fix a maximum mass of the satellite and estimate a capacity for the tanks (these values with those of the resulting dry mass are shown in the first three lines of Tab. 10).

If the simulation reaches the convergence within a certain number of iterations, the software provides automatically a detailed report and 3D visualization of the orbit (see Appendix B for STK reports).

Then a quick analytical study of the configurations was carried out in case they had to perform a return in LEO orbit.

### 3.5.2 STK Results

With STK we have simulated the one way trip to GEO of the three cases. To verify the goodness of the results, the values of the propellant mass used have been compared with those calculated analytically by means of the Eqn. 3.1, once the reports have been drawn up.

$$m_{prop} = m_{drytot} \left( e^{\frac{\Delta V}{g^{Isp}}} - 1 \right) \quad 3.1$$

	<i>Case 1</i>	<i>Case 2</i>	<i>Case 3</i>
Max total mass (kg)	2800	2800	6000
Dry mass STK (kg)	2200	2200	4500
Max propellant STK (kg)	600	600	1500
Prop. mass one way STK (kg)	430,97	583,94	1.251,93
Prop. mass one way (analytic) (kg)	400,51	580,16	1187,41
Transfer duration (s)	1,08E+07	7,90E+06	8,47E+06
Transfer duration (days)	125	92	98
Dry mass with return in LEO (kg)	2200	1990	4110
Max propellant with return in LEO (kg)	600	810	1890
Prop. mass for LEO-GEO-LEO (kg)	556,16	738,68	1526,19

**Table 10** Simulations Results.

In Tab. 10 is possible to notice that the software results are more conservative than analytical ones.

Transfer duration is defined as the time required to the OMV to transfer the specific cargo from the platform parking orbit to the target orbit.

The average duration is more than 5 months but there is only 3 to 4 months.

Cases with DD allow direct transport in less than 100 days; this is less than a casual GTO duration<sup>20</sup>.

In Case 2 is possible to arrive in GEO a month before Case 1 at the cost of only 150 kg of extra propellant.

---

<sup>20</sup> The times reduced or even halved with respect to the average may be due to two factors before others, to the fact that we do not consider the eclipses and the fact that we use high power motors, while for previous studies low power motors were used.

For completeness, it has been tried to configure the masses for a possible return to LEO. The part of the way back orbit and the consumption including the return were calculated analytically by formulas.

It is obvious that return will be even faster; the satellite will certainly have less propellant but it will also have released the payload in GEO.

Case 1 is the only one that keeps the same configuration of the masses for both mission options, an  $I_{sp} = 2800$  s allows to increase the Delta-V from 4.58 km/s to 6.2 km/s (for the reusable configuration) without lading a new tank.

For other cases the lowering at 2000 s of the  $I_{sp}$  and the exponential growth of the  $m_{prop}$  force to change the amount of available propellant on board. Lower travel times compensate the lower dry mass requirement.

With the third Case, on the other hand, it is possible to see that with two 20 kW Hall thrusters we bring into GEO orbit twice the weight with a difference of one week if compared to Case 2.

### 3.5.3 Eclipses Considerations

When the mission starts in LEO, a large fraction, of the orbit is in shadow. As the Space Vehicle transits to a higher altitude, the mission duration in shadow will be reduced.

Frequency and duration of occultation are dependent on altitude, inclination, and has a seasonal dependence.

Eclipse durations vary from 33 to 43 minutes at orbital altitudes up to ~12,500 km. Eclipse durations fall off very rapidly and go to zero at ~13,000 km so operations at higher altitudes do not have eclipse-induced SEP operations shutdowns.

HETs includes up to ~1100 sun/eclipse cycles with thruster on-time per orbit varying from ~50 minutes to tens of hours as altitude increases.

Eclipse cycling does not stress the electric propulsion system since it is designed to experience >10,000 cycles.

# Chapter 4

A natural continuation of the precedent chapter is the analysis and description of the OMV for all the cases evaluated. A brief description of principal systems and subsystems will allow us to discuss the design in terms of mass and dimensions.

We will focus on the propulsive system and on the power system in two different conditions, in nominal drive or in direct drive. The latter will be deeply investigated.

## 4.1 Mission Concept

The tug can provide high Delta-V capability at relatively low cost, at the penalty of relatively slow transfer time. The development, as said before, is focus on SEP by employing:

- An integrated Space Vehicle with no complex docking, rendezvous or separation events. The concept will be developed with launch vehicle flexibility in mind<sup>21</sup>.
- Spacecraft bus dedicated to SEP propulsion function.
- Simple orbital operations with relaxed pointing requirements for system attitude control.
- No critical events following launch and solar array deployment.
- Prime purpose is to move mass from point A to B in space.
- No focus on instruments or small attached payloads.
- Very high EP power levels.

Key requirements for systems can be extracted from the analysis of the mission concept. These have been grouped together in the Tab. 11. The same list is also a series of challenges that require cutting-edge technology to be implemented.

## 4.2 System Design

Through the use of appropriate approximations, a simple system overview and analysis can be performed for all the three cases taken into account in the previews chapter.

---

<sup>21</sup> A shared (dual) launch on a Falcon 9 or Ariane 5 is assumed.

<i>Effects</i>	<i>Key requirements</i>
Release orbit for the cargo module (a 400 km circular orbit) target orbit for payload (a 42000 km circular orbit).	In compliance with the currently available launch vehicles and launch site.
Dwell in radiation belts during spiral orbit transfer and repetition (Plasma environment problems).	Employ electronics and system implementations that tolerate total ionizing dose and single event effects. Use design methods to overcome effects of space charging and sustain operations.
Large, distributed inertia space vehicle in varying orbital environments.	Size attitude control system to handle disturbance torques and aero-drag during LEO operations.
Large, high voltage, high power subsystem to support SEP power.	Size power generation, control, and distribution to safety and reliability operate EP system.
The range of thermal control regimes/orbit from LEO through GEO.	Size thermal control provisions to handle the full range of albedo and eclipse durations.
Repeated eclipse cycles that interrupt power production	Guarantee performance through the design and test of better thrusters in terms of lifetime and number of stress cycles.
Long-term SEP operations.	Size solar panel BOL properly, design for refuelling and maintenance.

**Table 11** Effects on the basic mission concept and key requirements.

Space-tug can be considered as a geostationary satellite except for:

- the need of payload regulation, because there is no telecommunication payload (except for Telemetry, Tracking and Control),
- if several travels (for instance LEO/GEO) are planned for the same space-tug during its lifetime, the Solar Array has to be sized according to expected total radiation dose during the mission.

Therefore, both power architectures of a space-tug and a geostationary satellite are very close and could be identical with limited impacts to get common developments for units compatible of both uses [32] [40]. A modular design of power units is a way to adapt them to the telecom satellite power range.

Subsystems can be modelled at different levels of detail, but their design is strongly influenced by the presence of electric thrusters.

In particular, the subsystems that are most influenced by the adoption of electric propulsion (EP), substantially affected by the adoption of high power HETs, are the Electrical Power Subsystem (EPS) and the Thermal Control Subsystem (TCS).

Indeed, the EPS is in charge of conditioning, controlling, distributing and storing electrical power, whereas the TCS shall maintain all spacecraft and payload components within proper temperature boundaries, balancing the heat emitted by the spacecraft as infrared radiation against the heat dissipated by its internal components plus the heat absorbed from the environment.

Because of the long time in spiral orbit, robust GNC capabilities will be needed. The Attitude and Orbit Control Subsystem (AOCS) will aim to the stabilization and proper orientation of the spacecraft despite the external disturbance torques.

Moreover, the functional analysis highlighted the need to include also the following subsystems.

TTC, providing carrier tracking, command reception and detection, telemetry modulation and transmission, ranging and housekeeping functionalities.

CDH, aiming to the reception and distribution of commands, the collection, formatting and delivery of telemetry for standard spacecraft and payload operations.

STR&MEC, subsystem, which supports all other spacecraft subsystems, attaches the spacecraft to the launch vehicle and provides for ordnance-activated separation.

HARN, connections provided by cables and harnesses.

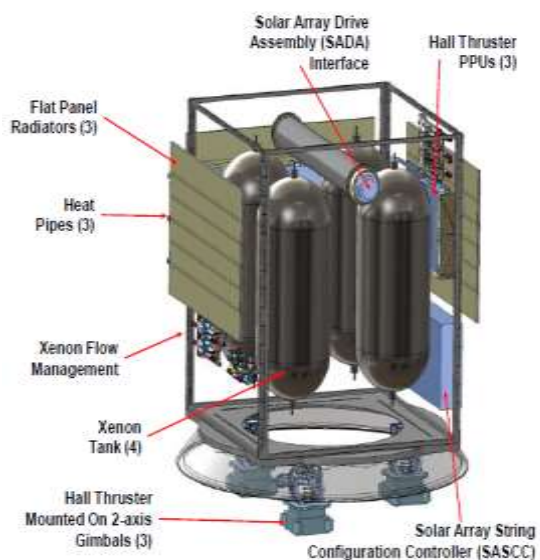


**Figure 20** Concept of propulsion assembly (credit by [27]).

#### 4.2.1 Electric Propulsion Subsystem (EP)

Going into the details, the propulsion subsystem includes on one side the AOCS actuators and on the other side the EP subsystem for primary propulsion. EP subsystem design will drive the sizing of the solar array and PMAD current/voltage. The main elements are:

- HETs cluster. The Thruster Unit (TU) consists of an HT20k equipped with at least one high-current hollow cathode (CAT) centrally or externally mounted, and a

Pointing Mechanism (PM) which provides the thruster with steering capabilities for modifying thrust direction<sup>22</sup>;

- A Fluidic Management System (FMS), composed by Pressure Regulators (PRs), Flow Control Units (FCUs) and tanks (up to 1890 kg of Xe), which aims to regulate the propellant pressure and distribute it to TU;
- In nominal drive a Power Processing Unit (PPU) and in direct drive condition a DDU, which provides electrical power supply, control, monitoring and electrical protection for all the EP components.

#### 4.2.2 Electrical Power System EPS

Adopting high-power electric propulsion has a strong impact on the design of the platform also from a power point of view. Following these considerations, the power budget for the platform has been implemented for a 25kW energy demand with a PPU efficiency of 95%. The total power demand is used to size the main components of the EPS.

This subsystem includes deployable solar panels for power generation and secondary batteries for energy storage. A preliminary sizing is obtained, defining geometry, mass and specific power (see Tab. 12).

Power generation	2x ROSA wings	12.5 kW per wing 125 m <sup>2</sup> 156.25 kg	29.5% efficiency, GaAs o ZTJ cells, 160 W/kg and 200W/m <sup>2</sup> Wing size 3x20,8 m
------------------	---------------	---	---

**Table 12** Power generator data.

---

<sup>22</sup> Hall thruster strings which can be operated singly.

### 4.2.3 Solar Array

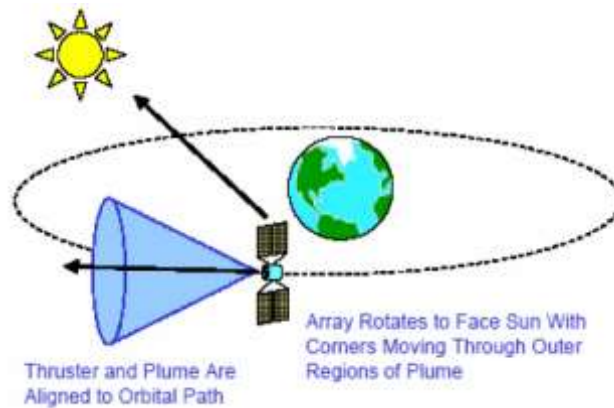


**Figure 21** Typical solar electric propulsion mission schematic (credit by [35]).

Considering the data in table 12 in order to produce 25 kW of power, more than 150 kg of solar panels would be needed. Apart from the power to mass ratio, we consider also a state of the art specific power of 200W/m<sup>2</sup> for a rectangular shape wing. These two constraints led to the conclusion that the Deployable Space Systems (DSS) Roll-Out Solar Array (ROSA) is the best option for this system.

Solar panels will have to face multiple issues, which must be taken into consideration for future analyzes.

Some of them are explained below.

- The long spiralling trajectories deteriorate the cells due to the long stay in the Van Allen belts. This topic becomes even more complicated in case of multiple travels. Power produced by solar panels is reduced inversely proportional to the square of the distance from the Sun.
- The fraction of solar energy not converted into electrical energy must be deployed in space through radiators to avoid the uncontrolled growth of the spacecraft temperature.
- The array will constantly point toward the sun while the spacecraft orbits the earth (see Fig. 21), and some interaction will take place between the array and the HET thruster plume, especially at the inner corners of the array as this move through the outer regions of the plume.

The radiation is largely due to proton fluence; both multi-junction and thin film solar cells are much more susceptible to ion fluence than electron fluence. In this case, GaAs cells would require at least 12 to 20 mils of cover glass, adding significant mass, to reduce

radiation-induced degradation. CIGS cells degrade significantly in a high proton flow but the damage is annealed out at the operating temperature of about 70°C. The result is that the cells maintain about 80% of their original output power without added cover glass protection at cost of lowering the cell efficiency.

The issue of spacecraft charging and solar array arcing is a serious design problem<sup>23</sup>.

The cover glass also serves as insulator for the surface but interconnections between cells would remain conductive. Rather than exposed metallic interconnects, the arrays could use wrap-through interconnects that are not exposed to the surrounding plasma like the ones in the ISS.

Another solution is the use of light concentrators. The concentration allows the use of reduced solar cell and cover glass mass although the concentrator and heat rejection of the magnified cells adds mass back to the solar array module.

This allows the cover glass thickness to be increased with a lower mass penalty than with non-concentrator arrays. The thicker cover glass and additional protection that form the concentrator lens provide increased protection to the solar cells.

### 4.3 Structural Design

Structurally the system takes inspiration on the EELV Secondary Payload Adapter (ESPA) here reported in Fig. 22. The core structure of the OMV is a resembling of the ESPA ring which provides a flexible and adaptable structure also for rideshare missions. This structure provides a simple and easily adaptable method of packaging all the required equipment [28] [29].

The upper portion of the tug provides a method of carrying up deployable payload (from 600 kg to almost 2 tons for Case 3).

The building blocks of the principal structures allow for a system to be developed without prior knowledge of the primary payload or secondary payloads. This increases the attributes of elasticity and versatility required by the type of mission.

---

<sup>23</sup> High voltage array design guidelines: for instance, the employment of welded-through interconnections, the use of coverglass sheets that shield more than one cell in order to reduce the number of cell sides that can collect electrons, the encapsulation of solar array conductors and cell edges. The string arrangement should also be designed in such a way that the maximum voltage difference between two adjacent cells is approximately equal to the measured arc voltage threshold.



**Figure 22** SEP tug concept base on ESPA ring (credit 29).

The structures were designed to be cost-efficient and easy to fabricate with all of the elements made of some form of aluminium and there are no expensive materials such as carbon fibre composites or titanium.

The other structural parts are made from composite sandwich structure with aluminium face sheets & aluminium honeycomb core.

The original system is designed to hold up to seven Xenon propellant tanks (total 1890 kg) mounted vertically and internally.

The original circular shape of the structure has been modified in a more squared shape according to the trend of geostationary satellites, to allow easier casing and study.

Dimensions for Case 1 and 2 are  $3 \times 3 \times 3.6$  m.

## 4.4 Introduction to Direct Drive

In the last two decades the photovoltaic technology development, in addition to the similarity in AS and SA V-I characteristics, leads to substantial research upon the possibility of powering the HET directly from SA, leading to the so-called "direct drive" architecture for HET (DHET)<sup>24</sup>. The Direct-Drive allows the anode supply (AS) removal, which is the most invasive element of the Power Processing Unit (PPU) in terms of mass, complexity and thermal burden.

A Direct Drive allows also the reduction of EMIF mass and possibly a different integration of TCS. Important mass savings can be also exploited in an indirect way.

The fact that the solar array must provide power to the thruster at high voltage (about 300 V) gives the opportunity to design a high voltage bus. This leads to substantial benefits

---

<sup>24</sup> The first studies on DD date back to the early 1970s.

regarding the Power Management and Distribution System (PMAD) in general, but extending also to the entire electric power system [42].

Of course, the type of mission has to be considered (orbit, payload, duration, etc.), but it has been already demonstrated that the high voltage bus arrangement could lead to substantial mass benefits (e.g. GEO) [37 – 39].

#### 4.4.1 Differences

Present Hall thruster systems use conventional power processing units in combination with standard solar arrays operating from 28 V to 120 V. For low power levels these systems are ideal and the use of a PPU brings many benefits to a Hall thruster system, such as:

- isolation of the thrusters system from the spacecraft power bus and solar arrays,
- control of the thruster discharge current and voltage which are directly related to the thrust and  $I_{sp}$ ,
- the ability to operate over a wide input voltage range associated with traditional arrays.

However, for future high power (hundreds of kilowatt to megawatt) systems the present output voltage levels associated with today's solar arrays require unacceptable current levels leading to excessive cable masses as well as high losses.

To minimize these disadvantages, several researchers [42 – 45] have investigated the option of creating high voltage solar arrays, operating at voltages above 300 V, and directly connecting them to the input of the Hall thruster, increasing the overall PPU efficiency.

In these direct-drive EP systems, the PPU can be simplified into a direct-drive unit (DDU) made up by two components. The first is a Low-Voltage Power Unit (LVPU), and the second is a Thruster Control Unit (TCU). The LVPU is used to down-convert the high voltage from the solar array bus to a voltage level more typical of existing spacecraft buses<sup>25</sup>.

The function of the TCU is very similar to a conventional PPU in that it is used to interface with the onboard spacecraft computer, process commands associated with the thruster by controlling the propellant flow, the cathode heater and keeper as well as the thruster

---

<sup>25</sup> This allows existing spacecraft components such as star trackers, on-board computers, etc., to be used without having to be re-designed and re-qualified for the higher input voltage.

magnets. The TCU or Controller/Interface Unit (CIU) is also responsible for acquiring and processing the telemetry data.

Hall effect thrusters will not require voltage conversion for sustaining the discharge, however, are subject to large-amplitude discharge current oscillations; so, the Direct-Drive system is configured to connect directly the solar array to the thruster through an EMI filter<sup>26</sup>.

Fig. 23 depicts schematically the two different configurations highlighting the main differences between them.

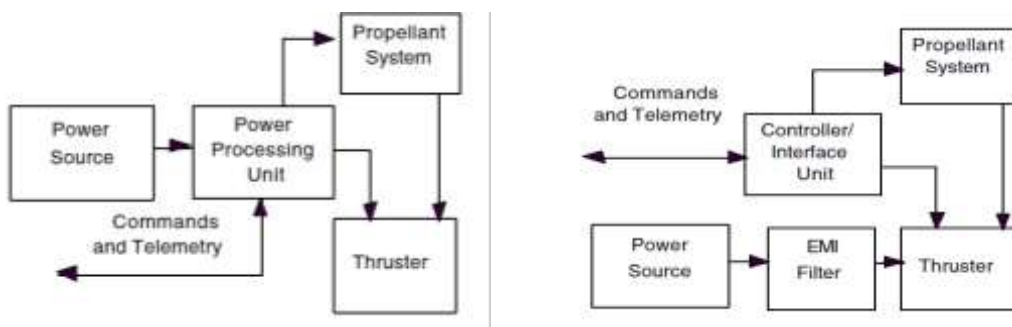


Figure 23 General configuration (right), direct drive configuration (left).

In Tab. 13 the fundamental features of the two configurations are summarized. On a practical level, the choice of one or the other implies advantages or disadvantages.

Unfortunately, the efficiency gains of operating at high voltage can be offset by spacecraft charging problems. Nowhere this trade-off between system efficiency and spacecraft charging is more evident than in the case of high voltage solar arrays operating in a plasma environment.

However, the high voltage solar arrays in a DD system must be capable of operating in the charge exchange plasma that is generated in the HET plume.

In the Direct Drive implementation there also other issues (the regulation of the thruster performance and problems regarding the thruster's startup, voltage adaption for spacecraft payload and other subsystems) but these will not be taken into account in this writing.

---

<sup>26</sup> Without a regulated discharge power supply, a direct-drive thruster's acceleration potential will change with the solar array voltage fluctuations.

<i>PPU efficiency ~95%</i>	<i>DDU efficiency ~99%</i>
-	Significant EPS mass savings. PMAD mass saving.
Electronic parts for PPU and PMAD are commercially available. PMAD must deliver predetermined I/V range to PPU.	Electronic parts for DDU and PMAD mostly are not available. 300 V technical challenges include higher electron collection current. 300 V class solar array design consistent with derated performance of service-oriented architecture electronic parts, insulators, gimbal, etc.
-	Higher specific power (kg/kW). Superior power efficiency.
Multitude is available. Discharge voltage and current (mass flow rate) can be varied and there is a possibility to provide the modes with a different combination of $I_{sp}$ and thrust.	Only discharge current (mass flow rate) can be varied. Mode regulation possibly is limited $I_{sp}$ cannot be regulated.
-	Significantly less thermal load
Single thruster operation is isolated from the EPS. Decoupling, galvanic isolation between the source (array) and thruster.	Single thruster operation is not isolated from the EPS. Bus voltage control is primarily tied to electric propulsion thruster
Simplification of ground testing of individual components (solar array, EPS, electric of solar array electric propulsion subsystem). Simplification of the design of solar array electrical simulator. Prevention of interactions of multi-thrusters through the power bus.	Additional research needed for thruster stable operation and electric propulsion startup/shutdown and transition modes.
-	Cathode current sharing for multi-thruster operation. Effective grounding schemes.

**Table 13** Strictly comparison (advantages and disadvantages) in the installation of a PPU or a DDU.

## 4.5 Direct-Drive Mass Benefits

The study carried out wants to enlighten the mass benefit due to Direct-Drive configuration in missions equipped by high-power HET.

There are studies [43] [44] that prefer to divide the advantages deriving in *direct* and *indirect*.

The direct advantages can be divided into two main blocks. Therefore the first part of the mass saving concerns the discharge supply removal and the filters lightening. The second

block of mass reduction involves the thermal control system dedicated to removing the PPU waste heat.

Indirect advantages can be exploited by adopting the high voltage bus configuration. It ensures an improvement in the electric power system which leads to mass benefits.

These mass savings can be leveraged in many ways including reduction of spacecraft mass, reduced launch vehicle requirements, increased on-orbit lifetime or increased payload.

## 4.6 Direct Advantages

In order to evaluate the benefits of a Direct-Drive implementation, it is necessary to compute the mass reduction that this configuration can introduce.

Direct advantages have been defined as those strictly related to the adoption of DD, that allows mass reduction due to the PPU architecture modifications, and the side-effects due to a higher efficiency.

### 4.6.1 PPU Reduction

The elimination of AS leads to a lower DDU mass and a higher efficiency, compared to the baseline conventional PPU. This is clear considering the power and mass fractions of AS over the whole PPU processed power and mass.

The AS occupies an estimate of  $\frac{m_{AS}}{m_{PPU}} \geq 50\%$  mass fraction inside a PPU. Thus AS removal means a substantial reduction in PPU mass.

Being the AS removed, EMI Filter is reduced to the matching network between the thruster's anode and the SA, performing a similar function compared the one it has in the PPU but with a simpler architecture, leading to an EMI Filter mass reduction up to 50%. This filter cannot be completely removed because it provides protection of the spacecraft power bus and arrays from the current oscillations produced by the Hall thrusters.

In general DDU boxes, harness and remaining control electronics permit an 18% mass benefit compared to original PPU mass.

In literature [37] [46] parametric equations have been deduced for the estimate of PPU and DDU mass variation with power, along with estimations for a net mass benefit in the PPU to DDU transition.

Since no flight-model PPU has been developed for thruster at this power level (25kW) its mass has been estimated through a linear relation suggested by J.R.Brophy et al. [36] [37]

which relates the PPU input power ( $P$ ) to its mass ( $m_{PPU}$ ). The relations, obtained by curve fitting of existing PPU data, are:

$$m_{PPU} = 1.7419 \cdot P + 4.654 \quad 4.1$$

$$m_{DDU}^{sav} = 1.7P + 1.6 \quad 4.2$$

Here they are shown with the usual notation, with mass expressed in kg and power in kW.

#### 4.6.2 Thermal Control System

The other direct advantage is the mass reduction concerning the thermal control system of the PPU. The efficiency of the PPU is 95 % whereas the efficiency of the Direct-Drive is supposed to be 99% this implies a lower waste of heat.

Nowadays, the state-of-the-art for deployable radiators considers an average specific mass lower than 10 kg/kW<sup>27</sup>.

Another side-effect of high efficiency is the lower power requested to the SA, and this permits further mass savings because of reduced array area.

#### 4.7 Indirect Advantages

They are called “indirect” because HVB can be adopted regardless of the DD implementation.

For the indirect advantages a quantitative estimate cannot be performed in general terms since the system mass benefits are dependent on the spacecraft configuration (bus voltage, payload, eclipse period, etc.); so only a qualitative analysis is carried out.

In a high voltage bus configuration batteries, shunt regulators, PMAD cabling and all their housings can be scaled down depending on the above mission features.

A quantification of the mass benefits due to the bus voltage increment is shown in Tab. 14.

---

<sup>27</sup> According to J.R. Brophy et al. [36], future very high-power missions must meet the requirement of a TCS specific mass lower than 25 kg/kW.

### 4.7.1 Solar Array Active Area Reduction

It has been proved that, if applicable, a higher voltage bus can lead to substantial mass benefit because of the reduction in current level i.e. in power losses (proportional to the current squared  $P = RI^2$ ) [41].

In fact, cables size, solar cells number and their ancillary structure can all be decreased.

For instance, the harness cables mass varies approximately inversely with the square of the bus voltage ( $V$ ) according to the relation  $\alpha \left(\frac{P}{V}\right)^2$  where  $P$  is the bus power.

Lower power system losses due to high voltage bus allow for a lower power to be produced and thus a reduction in the solar array active area involving a reduction in cells number and in their support structures. This mass benefit is the most significant and its impact is enhanced as the spacecraft power increases<sup>28</sup>.

Conservatively, this benefit is not assessed here. We already choose state of the art power density and efficiency for sizing the SA.

### 4.7.2 Shunt Regulator

Another source of mass reduction due to high voltage bus concerns the shunt regulators of a Direct Energy Transfer (DET) technique.

When a spacecraft device (thrusters, payload, heaters, etc.) is turned off, shunt regulators dissipate the excess power produced by the solar arrays.

As the overall system efficiency is increased the power provided by solar panels to operate the devices is lower and consequently, during the non-operational period, the amount of power to be shunted is lower. A shunt regulator that has to dissipate less power is, of course, less massive and thus it is advantageous from a mass reduction standpoint. An estimation arisen from the papers says that at most can save 10 kg of mass.

### 4.7.3 PMAD

Another source of mass reduction involves the PMAD cabling. As already stated, a migration towards high voltage bus allows a sensible scaling of the harness size. Power losses are proportional to the current square; the mass of PMAD cabling varies with the inverse squared voltage [49].

---

<sup>28</sup> It has been also demonstrated that in a geosynchronous telecommunication satellite the solar array size reduction due to the adoption of high voltage bus is much more significant than the array reduction due to Direct-Drive application.

#### 4.7.4 Battery

Due to its higher energy density, a migration towards 300 V could actually save significant additional mass relative to the baseline batteries at a lower voltage. However, apart from that, the increased efficiency attainable with the high voltage bus allows to further reduce the mass of the battery.

The assessment of the mass benefit can be carried out using the information in the study of Kerslake [41], assuming that the mass of the batteries scales directly with the energy they can store.

#### 4.7.5 Further Mass Reductions

As a consequence of the mass and size reduction of components such as PMAD cables and shunt regulators also their housings are cut down in terms of dimensions and consequently in mass.

Less significant mass benefits can be obtained also from the attitude control system. The total mass reduction, in particular, the ones regarding solar array, entail a spacecraft's moment of inertia decrease.

The requirements for the reaction wheel and the thrusters can be lightened leading for example to propellant and tankage saving. The calculation presupposes the precise knowledge of the spacecraft configuration and the attitude control strategy.

	<i>Bus voltage</i>				
	28 V kg	50 V %/kW	120 V %/kW	300 V %/kW	300 V DD %/kW
SA	126.6	-1.8	-2.7	-3.2	-3.6
BS	17.6	-1.1	-3.6	-4.7	-4.7
PMAD boxes	102.6	-1.8	-2.9	-3.3	-5.8
PMAD cabling	24.5	-5.1	-7.2	-7.7	-7.7
TOT	271.3	-2.0	-3.2	-3.8	-4.9

**Table 14** Design impact of bus voltage on EPS. These data refer to a study carried out by Kerslake at the NASA Glenn Research Center [41] which analyzes a GEO spacecraft equipped with a 10 kW HET and systems at the base voltage of 28V.

### 4.8 Mass evaluation

The subsystem mass breakdown is shown in Appendix B in three different tables. The various hardware masses are technology dependent, and the throughput is based on mission analysis.

The mass benefit of the DD is clearly visible by observing the first two architectures. For a 25 kW tug, the adaptation to a direct drive condition involves an overall mass reduction of 120 kg more or less (4.3% of the total mass).

The change in the operating point of the thruster involves, as seen in Chapter 3, a propellant increase of 270 kg. The mass gain is therefore not used to increase the payload available but to increase the performance of the propulsion system.

The major benefit comes from the change in the PPU in DDU. To estimate it we used Eqn. 4.1 and Eqn. 4.2.

A nominal input power of 23 kW corresponding to a  $m_{PPU}$  of 44.1 kg and a possible  $m_{DDU}^{sav}$  of 40.7 kg, it is 92% of each processor. This lead to a total mass saving of 81.4 kg (two DDU weight only 6.8 kg).

In the third case, where the mass of the tug reaches 6 tons and a power level of 50kW, the 4 installed DDUs have a saving superior to 160 kg (2.7% of the total mass).

The results are in terms of the increase in payload delivered to GEO orbit, almost 2 tons, which could be used to carry a cargo or even a satellite, thus sparing it the transfer.

For the case with total mass is less than 3 tons, the payload is 817 kg for the case with PPU, and of 754 kg for the case with DDU, however sufficient for the transport in GEO orbit of a small satellite or a Cubesat fleet.

It is to be remarked that this result represents a preliminary analysis conducted on the basis of available information, and assumptions have been made to replace insufficient data.

More mass savings for the SEP vehicle can be achieved by continuing to develop: advanced solar array technologies, cryogenic storage of the xenon propellant, direct drive power electronics, new compact thruster designs and lightweight radiators.

# Chapter 5

The topic of this chapter is the plasma and how it behaves when it comes into contact with surfaces at a different potential. Descriptions, formulas and theory are the basis of the problem presented in the next chapter and of the Matlab code used to solve it. Plasma definitions

The term *plasma* was coined by Langmuir and Tonks (1929) “to designate the portion of an arc-type discharge in which the densities of electrons and ions are high but substantially equal”.

Literature gives different definitions of plasmas.

In [7] F. F. Chen and M. D. Smith define the plasma as an ionized gas composed of positive and negative charges (and possibly neutral atoms and molecules) of almost equal charge density. At least one kind of charge is mobile.

For J. A. Bittencourt [3], a plasma is a macroscopically neutral substance containing many interacting free electrons and ionized atoms or molecules, which exhibit collective behaviour due to the long-range electromagnetic forces.

The most common type of plasma is a gas of such a high temperature that is ionized, i.e. a gas in which an appreciable number of atoms have been stripped of at least an electron and have become positive ions. Because of its free electrical charges, a plasma differs from ordinary gases because it is subject to electric and magnetic forces.

Plasmas are often called the fourth state of matter. In the next sections, we will assume the following features:

- charged particle collisions with neutral gas molecules are important;
- there are boundaries at which surface losses are important;
- ionization of neutrals sustains the plasma in the steady state;
- the electrons are not in thermal equilibrium with the ions.

## 5.1 Sheath Theory

At the edge of a bounded plasma, a potential exists to contain the more mobile charged species. This allows the balancing of flows to the wall. Even though the plasma consists of an equal number of positive ions and electrons ( $n_i = n_e$ ), the electrons are far more mobile

than the ions. Because of the difference in mass ( $\frac{m_e}{m_i} \ll 1$ ) and temperature ( $T_e \geq T_i$ ), the thermal velocities result not equal

$$v_e = \left(\frac{eT_e}{m_e}\right)^{1/2} \neq v_i = \left(\frac{eT_i}{m_i}\right)^{1/2}. \quad 5.1$$

This would make impossible to maintain the assumption of quasi-neutrality.

The plasma will, therefore, charge positively with respect to a grounded wall<sup>29</sup>. The non-neutral potential region between the plasma and the wall is called *sheath*<sup>30</sup>. The thickness of this layer is typical of the order of some Debye lengths (see Eqn. 5.2).

In other words, this boundary layer exists generally when a material body is immersed in a plasma due to an external biasing of the body surface or to ambipolarity diffusion in case of an insulated body.

### 5.1.1 Plasma between two Walls

Let us consider a plasma confined between two walls, with  $n_i = n_e$  and  $\phi = 0$  the potential of the grounded wall. Because of zero net charge density  $\rho = e(n_i - n_e)$ , the potential and the electric field  $E_x$  are null everywhere.

However, the electrons are so fast that some are lost to the walls. They lead to the situation in Fig 25. A membrane layer is then formed close to the wall in which the density  $n_i \gg n_e$ . The net positive  $\rho$  in the sheath region traces the potential profile  $\phi(x)$ , which is positive within the plasma and falls sharply to zero near both walls.

In order not to collect a net electrical current, the wall spontaneously acquires a potential difference (with respect to the plasma), by collecting the proper charged particles.

This acts as a confining potential: a “valley” for electrons and a “hill” for ions because the electric fields point from the plasma to the wall.

Thus, the force  $-eE_x$  acting on the electrons is directed into the plasma; this reflects the electrons traveling toward the walls back into the plasma. Conversely, ions from the plasma that enter the sheaths are accelerated towards the walls.

---

<sup>29</sup> The potential gradient in the plasma and at the plasma boundary is a natural consequence of the different temperatures and motilities of the ions and electrons.

<sup>30</sup> It is divided into two zones. Adjacent to the surface is the Child-Langmuir (CL) sheath, where the electron density is negligible. Next is the Debye sheath, in which the electron density drops exponentially with  $\phi$ .

### 5.1.2 Pre – Sheath

Plasmas can have different ionization degrees. In the less ionized, electrons have temperatures of a few eV while the ions are cold. In this situation, the ions are accelerated through the sheath potential, while the electron density decreases according to the Boltzmann factor.

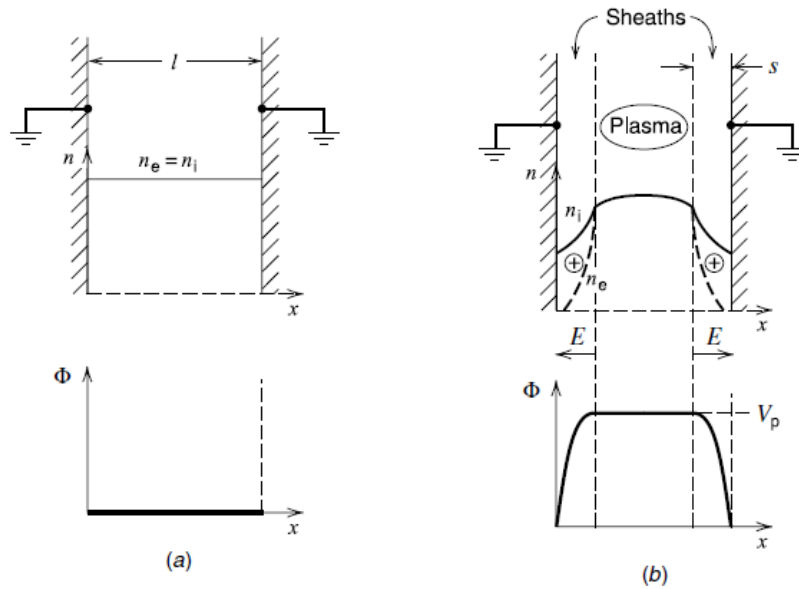


**Figure 24** The formation of plasma sheaths: (a) initial ion and electron densities and potential; (b) densities, electric field and potential after formation of the sheath (credit by [2]).

The electron density would then decay far from the walls, at a distance of the order of a Debye length ( $\lambda_D$ ), to shield the electrons from the wall.

$$\lambda_D = \sqrt{\frac{\epsilon_0 T_e}{n_s e^2}} \quad 5.2$$

It is necessary to prove that there is also a transition or pre-sheath zone between the neutral and the non-neutral sheath's plasma in order to maintain continuity in the ion flow.

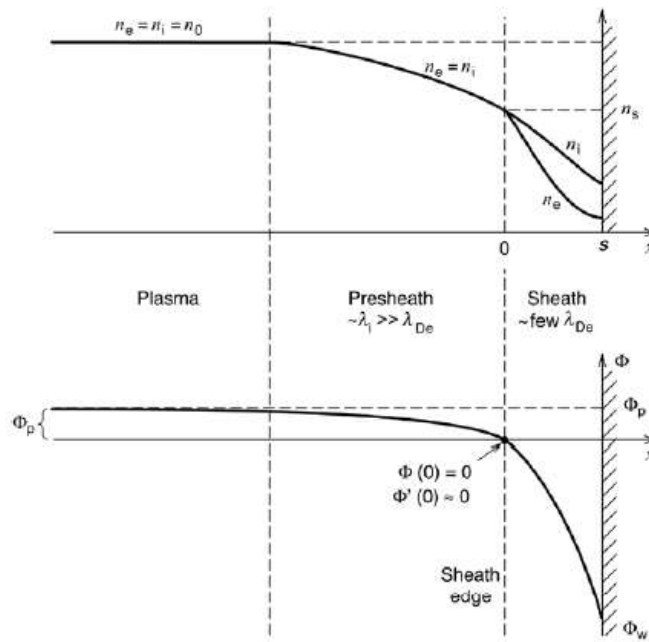


**Figure 25** Qualitative behaviour of sheath and pre-sheath in contact with a wall.

If the wall is biased with a high negative voltage with respect to the plasma, the current to the wall is almost all ion current. Provided the ion motion in the sheath is collisionless, then the steady self-consistent ion density is not uniform, but rather is described by the Child-Langmuir law of space-charge-limited current in a planar diode.

The ideal conditions described are not always achieved.

Situations that differ from the basic theory arise due to collisional effects in the sheath region; in this case, the ion flow is impeded.

In some cases, the temperature of the ions cannot be ignored with respect to the electron temperature and the electrons distribution could not be assumed as a Maxwellian distribution.

### 5.1.3 Collisionless Sheath

To demonstrate what has been theorized we assume:

- I. Maxwellian electrons at the temperature  $T_e$ .
- II. Cold ions  $T_i = 0$ .
- III.  $n_e(0) = n_i(0)$  at the plasma sheath interface, between neutral and non-neutral region at  $x = 0$ .

As seen in Fig. 26, i.e. we assume that the potential is zero when  $x = 0$ , and that the ions have velocity  $u_s$ .

Starting from the energy conservation equation for ions, we obtain

$$\frac{1}{2}Mu^2 = \frac{1}{2}m_i u_s^2 - e\phi(x). \quad 5.3$$

The law of continuity in the flow (no ionization in the sheath) leads to

$$n_i(x)u(x) = n_{is}u_s \quad 5.4$$

$$n_i = n_{is} \left(1 - \frac{2e\phi}{m_i u_s^2}\right)^{-1/2} \quad 5.5$$

with  $n_{is}$  ion density at the edge of the sheath. The number density of electrons is given by the Boltzmann relation instead ( $T_e$  is in eV)

$$n_e(x) = n_{es} \exp\left(\frac{e\Delta\phi(x)}{T_e}\right) \quad 5.6$$

Since  $n_{es} = n_{is} = n_s$  at the edge of the sheath, we replace  $n_i$  and  $n_e$  in the Poisson equation (Eqn. 5.7)

$$\frac{d^2\phi}{dx^2} = \frac{e}{\epsilon_0}(n_e - n_i). \quad 5.7$$

and we obtain

$$\frac{d^2\phi}{dx^2} = \frac{en_s}{\epsilon_0} \left[ \exp\left(\frac{\phi}{T_e}\right) - \left(1 - \frac{\phi}{\mathcal{E}_s}\right)^{-1/2} \right], \quad 5.8$$

where  $\mathcal{E}_s = \frac{1}{2}m_i u_s^2$  is the initial ion energy.

Eqn. 5.8 is the nonlinear equation at the base of the potential distribution of the sheath and of the ionic and electronic density. However, as we shall see in the next section, it has a stable solution only for sufficiently large  $u_s$ , created in an essentially neutral pre-sheath region.

#### 5.1.4 The Bohm Sheath Criterion

In order for the sheath equation to have a physically plausible solution at the boundary with the plasma, a criterion is necessary.

A first integral of Eqn. 5.8, can be obtained by multiplying by  $d\phi/dx$  and integrating over  $x$ .

$$\int_0^\phi \frac{d\phi}{dx} \frac{d}{dx} \left( \frac{d\phi}{dx} \right) dx = \frac{en_s}{\epsilon_0} \int_0^\phi \frac{d\phi}{dx} \left[ \exp \frac{\phi}{T_e} - \left( 1 - \frac{\phi}{\mathcal{E}_s} \right)^{-1/2} \right] dx \quad 5.9$$

Cancelling  $dx$  and integrating with respect to  $\phi$  we obtain

$$\frac{1}{2} \left( \frac{d\phi}{dx} \right)^2 = \frac{en_s}{\epsilon_0} \left[ T_e \exp \frac{\phi}{T_e} - T_e + 2\mathcal{E}_s \left( 1 - \frac{\phi}{\mathcal{E}_s} \right)^{\frac{1}{2}} - 2\mathcal{E}_s \right], \quad 5.10$$

where we have set  $\phi = 0$  and  $d\phi/dx = 0$  at  $x = 0$ , corresponding to a field free plasma. Eqn. 5.10 can be integrated numerically to obtain  $\phi(x)$ . However, the right member of the equation should be positive; physically this means that the electron density must always be less than the ion density in the sheath region. The same part of the equation is then translated into Taylor series to obtain

$$\frac{1}{2} \frac{\phi^2}{T_e} - \frac{1}{4} \frac{\phi^2}{\mathcal{E}_s} \geq 0, \quad 5.11$$

which is satisfied with  $\mathcal{E}_s \geq \frac{T_e}{2}$ .

Replacing we find the Bohm velocity  $u_B$ .

$$u_s \geq u_B = \left( \frac{eT_e}{m_i} \right)^{\frac{1}{2}} \quad 5.12$$

A potential difference at least  $T_e/2$  accelerates the ions to the Bohm velocity.

This result is known as the Bohm sheath criterion:  $u_s/u_B \geq 1$ .

Ions that enters into the sheath have a velocity at least equal to the Bohm velocity [4] [7] [8].

This calls into question the existence of a pre-sheath that correlates speeds. In a quasi-neutral and collisionless plasma, there are no means for the ions to obtain the drift velocity  $u_B$ . How do the ions acquire this velocity?

There must be a finite electric field in the plasma over some region, typically much wider than the sheath, called pre-sheath.

The typical dimensions of the pre-sheath region are  $\sim 100\lambda_D$ , the quasi-neutrality condition holds and ionization processes and collisions need to be included in the model.

Hence, the region presented is not field free, although  $E_{(x<0)}$  is very small there. At the interface ( $x = 0$ ) there is a transition from subsonic to supersonic ion flow, where the

condition of charge neutrality must break down. The transition can arise from the geometric concentration of plasma, from ion friction forces in the pre-sheath, or from ionization in the bulk plasma.

The matching of the sheath and pre-sheath models is still a debated issue, the problem is that in the description of the pre-sheath region a singularity arises where  $u_s = u_B$ . From the pre-sheath point of view, the electric field diverges as we approach the plasma-sheath interface. On the other hand, from the sheath perspective, the electric field becomes zero as we move near the interface.

### 5.1.5 Collisional Plasmas

As we have seen, for the collisionless case, a unique Bohm velocity can be defined at the position where the quasi-neutral pre-sheath solution becomes singular.

For weakly collisional plasmas, a unique edge position is not exactly defined, and approximate methods of separating the plasma and sheath regions become more subtle.

## 5.2 Langmuir Probe

The sheath theory is at the base of the charging of the surfaces of a satellite but also of an important plasma diagnostic tool, the Langmuir probe.

Parallelism is actually simple<sup>31</sup>, a single Langmuir probe is nothing but a piece of conductive material (a tungsten rod or sphere) that is immersed in a plasma and biased at different voltages.

In both cases, the surface and the probe, a current is collected. In the first case, the current has to be evaluated for security or structural reason, in the other one, the current is used to obtain information about the conditions of the plasma as temperature and number density. The observations on the I-V curves can be easily adapted to both cases.

Metal probes, inserted in a discharge and biased positively or negatively to draw electron or ion current, are usually quite small and, under suitable conditions, they produce only a minor local perturbation of the plasma.

---

<sup>31</sup> This similarity is valid both in vacuum chamber and in space.

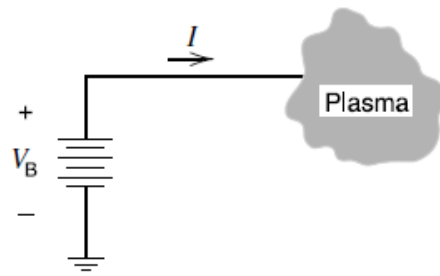


**Figure 26** Definition of voltage and current for a Langmuir probe (credit by [2]).

The probe is biased to a voltage  $V_B$  with respect to ground, and the plasma is at a potential  $\phi_P$  with respect to ground<sup>32</sup>.

If  $V_B = \phi_P$ , the probe is at the same potential as the plasma and draws mainly current from the more mobile electrons, which is designated as positive current flowing from the probe into the plasma [50].

For increasing  $V_B$  above this value, the current tends to saturate at the *electron saturation current*, but depending on the probe geometry, it can increase due to increasing effective collection area.

Looking at Fig. 27, for  $V_B < \phi_P$ , electrons are repelled according to the Boltzmann relation. For  $V_B = \phi_f$ , the probe is sufficiently negative with respect to the plasma that the electron and ion currents are equal such that  $I = 0$ .  $\phi_f$  is known as the *floating potential*, because it is the potential at which an insulated electrode, which cannot draw net current, will float. The floating potential is always lower than the plasma potential.

As the probe potential is lowered below  $\phi_P$ , electrons begin to be repelled while the ions start to flow to the probe surface. The collected current then decreases.

Where the curve shows a “knee” the probe is at the same potential as the plasma  $V_B = \phi_P$ . When the probe voltage is deeply negative with respect to the plasma voltage  $V_B < \phi_f < \phi_P$ , the current is increasingly ion current (negative into the plasma). In this condition, most of the electrons are repelled, tending to an *ion saturation current* that may also vary with voltage due to a change of the effective collection area (i.e. dimensions of the collection area and degree of conductivity of the material).

The magnitude of the ion saturation current is much smaller than the electron saturation current due to the much greater ion mass.

---

<sup>32</sup> Depending on the situation the “plasma potential” could be replaced with “space potential”.

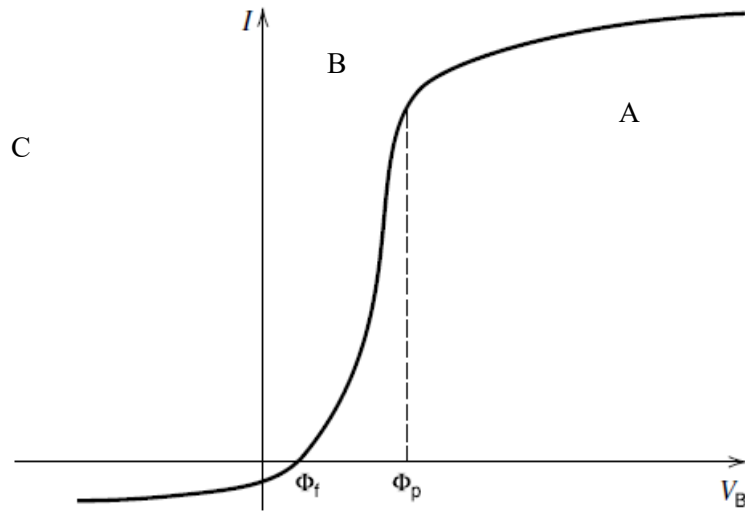


**Figure 27** When the probe voltage is positive with respect to the plasma, electrons are accelerated to the probe, while the ions are repelled. The collected ion current is smaller and smaller as the probe voltage is increased. The maximum electron flux is given by the thermal flux which enters the sheath around the probe, hence, the electron current flattens at highly positive values of  $V_B$ , the so called electron current saturation (A). It is customary to plot  $I-V$  curves with  $I_e$  positive and  $I_i$  negative (credit by [50]).

The ion flow to the wall is determined by the Bohm condition at the sheath entrance, which only depends on  $T_e$ , and by the plasma density (if  $T_e$  is not in eV, the follow equations need the Boltzmann constant  $k_B$ )

$$j_i = \frac{n_S}{2} \sqrt{\frac{T_e}{m_i}}. \quad 5.13$$

The region C in Fig. 29, where almost all electrons are repelled and the ion current saturates, is called the ion saturation region<sup>33</sup>.

In the other two regions (A, B), the electric current is

$$I_e = n_S v_e A \exp\left(\frac{e(V_B - \phi_P)}{T_e}\right) \quad 5.14$$

$$I_e = n_S v_e A \text{ if } (V_B > \phi_P). \quad 5.15$$

---

<sup>33</sup> The collected ion stream is also called *Bohm current*.

### 5.3 A Couple of Probes

The configuration of the double Langmuir probe is the one that more than others approaches what we will study in the next chapter, two bias surfaces that do not collect a current but more currents and the set floats with respect to the plasma.

These are two probes biased with respect to each other but insulated from the ground, so that the entire system is floating with respect to the plasma, following the changes of plasma potential [8].

Let us consider the case of two probes with the same area  $A_p$  and suppose that a voltage difference  $\Delta\phi = \phi_1 - \phi_2$  is applied between them.

As electrons are much more mobile than ions, both probes are in general negative with respect to the plasma

When there is no applied voltage, i.e.  $\phi_p = 0$ , there is no net current between probes, i.e.  $I = 0$ .

If a voltage difference  $\Delta\phi > 0$  is applied between the two probes  $\Delta\phi + \phi_2 = \phi_1$ , the potential of probe 1 becomes less negative than probe 2 compared to plasma potential.

Consequently, probe 1 collects more electrons than probe 2, resulting in a net current  $I$  between the two probes.

The current that flows from the plasma to the probes is composed of electrons and ions since the probe assembly is floating, the same current collected by probe 1 must be balanced by an opposite current in probe 2,

$$I_1 = -I = I_{1i} - I_{1e} \quad 5.16$$

$$I_2 = I = I_{2i} - I_{2e} \quad 5.17$$

Since the maximum positive current is limited by the ion saturation current, the same limit applies to the current flowing between the two probes.

Defining the ion and electron currents to probe 1 and 2 as  $I_{1i}, I_{1e}, I_{2i}, I_{2e}$ , then the condition that the system float (no net current from the probe system to the plasma) is

$$I_{1i} + I_{2i} - I_{1e} - I_{2e} = 0$$

The loop current is

$$I = I_{1e} - I_{1i} = I_{2i} - I_{2e}.$$

For the electron current, we have

$$I_{1e} = A_1 j_{esat} e^{\frac{\Delta\phi_1}{T_e}}, \quad I_{2e} = A_2 j_{esat} e^{\frac{\Delta\phi_2}{T_e}}. \quad 5.18$$

As described by the sheath theory, the current collected by a probe at  $\phi < \phi_P$  defined as  $I = I_i - I_e$  of which we already know the equations,

$$I_i = I_{is} = e \frac{n_s}{2} A u_b, \quad I_e = e n_s A \bar{v}_e \exp\left(\frac{e(\phi - \phi_P)}{T_e}\right). \quad 5.19$$

Where  $u_b$  is defined in Eqn. 5.12 and  $\bar{v}_e$  is equivalent to

$$\bar{v}_e = \sqrt{\frac{eT_e}{2\pi m_e}}. \quad 5.20$$

# Chapter 6

In order to design a spacecraft to accommodate electric thrusters, it is necessary to understand how the thruster plumes interact with the spacecraft and its payloads.

The chapter highlights the most harmful relationships that may exist between plasma and spacecraft. In particular, it describes the problem of electrostatic charging. This is a dangerous phenomenon for the health of the S/C and involves a particular study in the design phase.

The problem that we are preparing to analyze is a part of this study, and once delineate the internal mechanics allows to predict currents and variation of potential in a simple system architecture and to draw conclusions that are a starting point for subsequent studies.

## 6.1 Plume Interactions

It is well known that Hall thrusters present special plume<sup>34</sup> problems that are not encountered with ordinary chemical propulsion systems. A list of the commonly identified issues is as follows:

- The ionized plume interference on spacecraft communications with ground stations that cause EMI compatibility issues;
- Spacecraft charging and electrostatic discharge;
- Erosion of surfaces (especially solar arrays) as a result of sputtering by the high energy ions;
- Contamination due to re-deposition of sputtered material;
- RF emissions from the plume interfering with payloads;
- Backflow ion impingement caused by charge exchange plasma collisions.

Thruster plumes affect the spacecraft immediately during their operation and by slow cumulative processes. The immediate interactions may affect spacecraft operations; the longer-term interactions may affect spacecraft life. Due to the increased application of electric propulsion the detailed investigation of the appearing plasma interactions is an issue of highest importance.

---

<sup>34</sup> Composed of energetic and charged particles, with a non negligible ion flux at high angles from the thrust axis.

## 6.2 Spacecraft charging

The moving charged particles create electrical currents. Moving electrons are negative current, and moving positively charged ions are positive current.

When a spacecraft orbits the Earth, some of the electrical currents will flow, from natural plasma or plume plasma to spacecraft resulting in charge accumulating on its exposed surfaces.

This phenomenon is known as spacecraft charging.

Spacecraft charging is caused by the unequal collection of negative and positive currents by spacecraft surfaces, it generates an electric force field that decelerates like-charged particles (negative), decreasing their current and accelerates charged particles (positive), increasing their current.

The charging process (see Fig. 29) continues until the accelerated particles can be collected rapidly enough to balance the currents. At this point, the spacecraft has reached its equilibrium charging level or floating potential ( $\phi_f$  presented in Section 5.3) and no more charge accumulates.

Understanding spacecraft charging is important because the effects attributed are a serious engineering problem<sup>35</sup>.

First, a distinction must be made between surface and internal charging.

Surface charging is defined as charging on areas that can be seen and touched on the outside of the spacecraft. It consists in charging at the surface of conductive materials or very close the surface of dielectrics.

Internal charging is a consequence of energetic electrons; they can penetrate the spacecraft enclosure and deposit charge very close a victim site [54].

They both can result in dielectric or metal arcing discharges, that can, in turn, result in some issues already listed in the previous paragraph.

---

<sup>35</sup> In 1957 when the first satellite, Spoutnik-1, was launched, charging of bodies in space began to be studied. Later on, the measurement of high-voltage charging on the satellite ATS-5 in 1969 has shown that hazardous voltages could buildup on geostationary satellites. The risk was proven by the loss of the DSCS-9431 satellite on June 2, 1973 on a power failure consecutive to an electrostatic discharge.

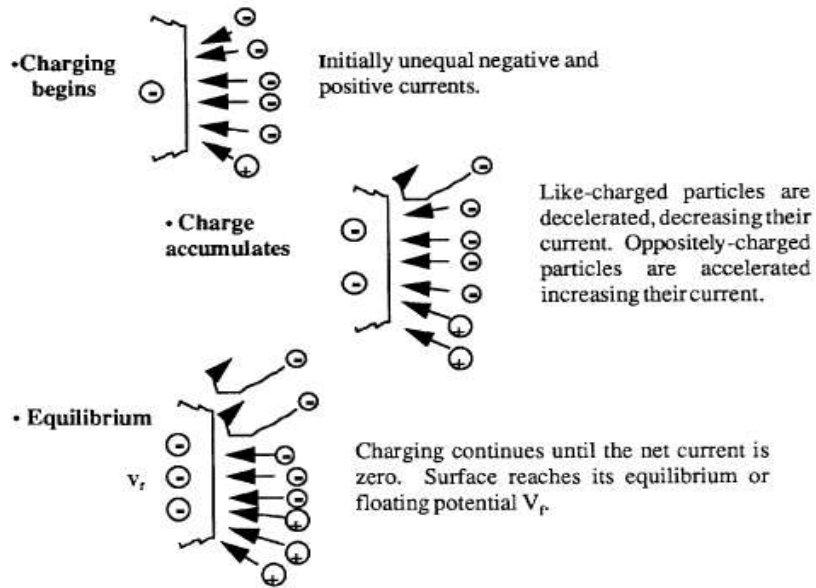


Figure 28 Electrostatic charging mechanism credit by [54].



Figure 29 Evaporation of polymer and metal due to discharge in electron-irradiated aluminized Kapton (credit by [54]).

## 6.2.1 Arc-Discharge

The primary mechanism by which spacecraft charging disturbs mission's activities is through arc-discharging.

Arc-discharging occurs when generated electric fields from differential charging exceed breakdown thresholds. The arc-discharge process rapidly releases large amounts of electric charge, which gives rise to currents flowing in the spacecraft structural elements. The arcing produces a broadband electromagnetic field, which can couple into spacecraft electronics and causes operational anomalies<sup>36</sup> ranging from minor irritations to the fatally catastrophic.

Besides generating electromagnetic interference that can couple with spacecraft electronics, arc-discharging leads to physical damage of affected surfaces (see Fig. 30)

Arc-discharging produces localized heating and ejecting of surface material from the arc-discharge site. The loss of material degrades spacecraft structural integrity and alters the properties of spacecraft surface materials. The ejected material is also a source of contamination for other surfaces through sputtering events.

## 6.2.2 Avoid Spacecraft Charging Effects

The results in [35] [53] indicate that the adverse impact of parasitic currents is substantially reduced by I) having low voltages on the parts of the array nearer to the thrusters exposed to the highest plasma current densities; II) insulating the low-voltage (<500 V) portion of the array (assuming that pinholes are not present in the insulation) and III) by maintaining the charge-exchange ion and neutralizer currents at the lowest levels compatible with the mission requirements of the thruster system.

Even so, the parasitic currents collected are a small fraction of the beam current and are even smaller fractions of the array-generated current.

To protect solar cells thicker cover glasses and oversized current and voltage capabilities must be used. For other spacecraft components, greater shielding, more robust electronics, and additional protective structures must be used, all of which reduce the potential mass savings acquired by using EP.

---

<sup>36</sup> Electric thruster plumes can carry currents between the thruster electrical power system and exposed electrical conductors such as solar array cell edges and interconnects. While the currents that flow through the thruster plumes are in general quite small, they may cause changes in subsystem potentials. These potential changes, if not anticipated, may be mistaken for system anomalies by spacecraft operators.

Lockheed Martin e EADS Astrium ([55] [56]) have conducted several studies and efforts to develop the analysis tools that were able to:

- *define the properties* of the plasma to which the spacecraft will be exposed, they evaluate the plume flow-field (through the creation of a Plume Model with PIC programs) to know ion current and plume energy;
- *develop design guidelines* with the purpose of reducing or eliminating the effects attributed to the spacecraft charging<sup>37</sup>;
- *create a sputtering database* and a characterization of the degradation to study erosion and contamination;
- *performing computer analyses* to model the charging level of the spacecraft.

Simulations have been carried out to infer the spacecraft potential equilibrium, not only simulating the natural space plasma but also the plume plasma; they have been compared with flight and ground data experiments. Principal and most used reference data came from the SMART-1 mission.

Our goal is precisely to trace these previous simulations. Starting from simpler configurations gradually more complex with the aim of getting as close as possible to the final structure of the presented tug. From the three cases described in Chapter 4, the second one is used for this purpose. Dimensions and components are necessary to evaluate how the 20 kW thruster plume interacts with the rest of the satellite (in particular its relationship with solar arrays).

There are two fundamental notes for the study that we are going to present.

A large part of this analysis took inspiration from the studies written by Ira Katz over the years but among all the ones presented at the *14th Spacecraft Charging Technology Conference* in 2016 [51]

The second is that, as already mentioned, the study is based on the sheath theory and on the behaviour of probes drowned in plasma.

---

<sup>37</sup> The computation of the reflected flow and further impacts (if any) is carried out with a Monte Carlo ray-tracing technique, based on the knowledge of normal / tangential / energy accommodation coefficients.

## 6.3 Schematic Model Introduction

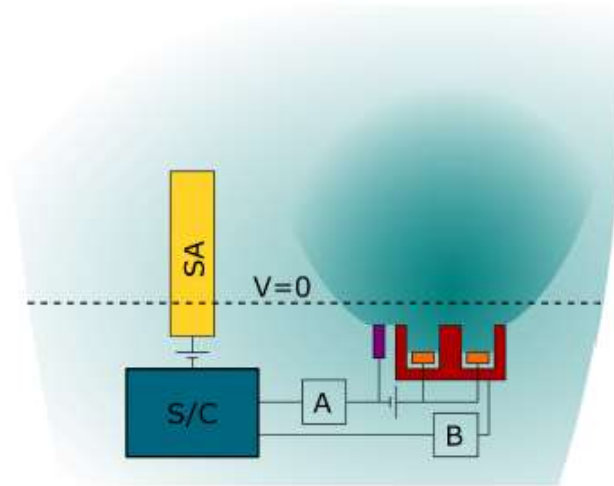


**Figure 30** Reference scheme of the problem.

Hall thruster plasma plumes connect thrusters electrically to the exposed spacecraft conducting surfaces.

In general, the interaction between the thruster plasma and the satellite is low but, if the solar arrays are close enough to the plume, they can collect an electron current from the cathode (see Fig. 35).

It is important to account for current paths through the plasma to prevent current loops or unintended propulsion system floating potentials.

Different currents are driven by different potentials. Electrons are attracted to potential positives. Ions are accelerated by potential negatives.

We will start from the simplest basics of plasma interactions and build up a complete model by adding the multiple components of a high power, Hall Effect thruster and solar electric spacecraft.

We then add solar arrays with exposed interconnects at a range of voltages.

Next comes the EP system generated plasma, followed by the resistor used to isolate the EP system power processing unit from spacecraft chassis ground.

The complete model proposed is schematized in Fig. 31. The fundamental elements are four<sup>38</sup>:

---

<sup>38</sup> Thruster unit (TU) is the union of cathode and thruster body.

- a thruster body (TB);
- a cathode;
- one solar array (SA);
- spacecraft chassis (S/C)

These are placed in a space composed of two different plasmas<sup>39</sup>. The plasma in the thruster plume has a higher density and temperature with respect to the space ambient plasma.

The boxes named A and B in the diagram could be resistances or power supplies, whose value is set arbitrarily. They can isolate an element or they can give a different grounding.

There are also two generators, the first is the one placed between spacecraft and solar panel ( $\Delta V_1$  is always known), the second is between anode and cathode in TU.

The problem could be solved using two different potential scales. The potentials with respect to spacecraft chassis ground

$$\text{Spacecraft Potential} = \phi_{sc} = 0 V$$

or alternately with respect to the local plasma. In this case, the plasma potential is assumed equal to zero everywhere<sup>40</sup>.

$$\text{Plasma Potential} = \phi_p = 0 V$$

The simple scheme proposed here aims to be first of all an exercise to evaluate the individual interactions between the various components, immersed in two different plasmas.

The final aim is to create a code, which provides current values and voltages for each component when the elements A and B vary.

## 6.4 Cathode

As discussed in Chapter 2, the sheath drop internal to a hollow cathode and orifice resistive heating produce energetic electrons that ionize the propellant gas and generate plasma. The

---

<sup>39</sup> Thruster plume plasma  $T_{e,th} = 3 eV, n_{th} = 10^{16} m^{-3}$ . Ambient plasma  $T_{e,pl} = 1 eV, n_{pl} = 10^{14} m^{-3}$ .

<sup>40</sup> It is a choice dictated by comfort, most of the texts still choose to set the plasma potential to zero and take the S/C potential as a reference.

combined insert and orifice potential drops are typically between 10 and 20 V, causing the external plasma to be about the same value above cathode common <sup>41</sup>, as illustrated in Fig. 32.

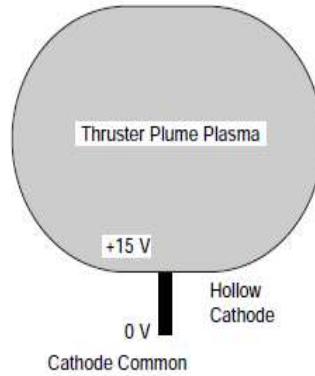


**Figure 31** The thruster neutralizer hollow cathode generates a plasma typically 10 to 20 V above the cathode common (credit by [2]).

The potential difference between the spacecraft chassis electrical ground and the hollow cathode usually referred to as "cathode common voltage" or CRP, is a good measure of the potential between the spacecraft and the plasma<sup>42</sup> [2].

$$\phi_P = V_{bias} + V_{HC} \quad 6.1$$

The plasma potential is the sum of bias voltage, our fixable CRP, and the  $V_{HC}$  linked to the phenomena of the sheath within the cathode.

According to Smart-1 flight experience, the cathode naturally stabilizes to a slightly negative potential with respect to the space plasma [51]. The cathode is fixed -15 V.

$$V_{cat} = CRP = -15 V.$$

---

<sup>41</sup> The hollow cathode generated plasma has an electron temperature of about 2 eV, typical of many laboratory plasmas.

<sup>42</sup> The resulting values of ion and electron currents depend on the cathode position, external or internal, and the presence of insulation on the pole covers or thruster surfaces.

## 6.5 Spacecraft Chassis and Theory of the Floating Potential

The spacecraft acts as a Langmuir probe in the thruster plume plasma and will float to a potential where the ion and electron currents from the plasma cancel each other.

*Electron current density > Ion current density*

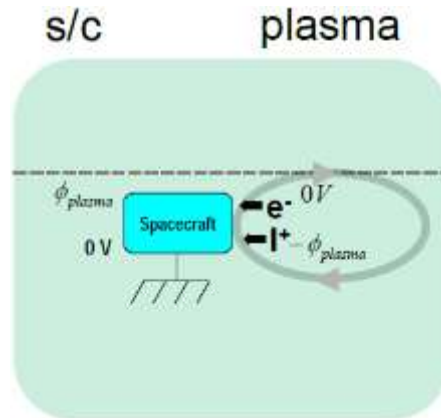


**Figure 32** Spacecraft chassis current collection. Potential with respect to S/C and with respect to space plasma (credit by [51]).

Since the ambient electron current density is much higher than the ion current density (as discussed in Chapter 5 plasma electron velocities are generally much higher than ion velocities), surfaces usually charge negative to repel most of the electron current.

This result is consistent with data from UARS [58] and SERT-II [59], two spacecraft instrumented to measure the spacecraft floating potentials with respect to the ionosphere.

Large negative floating potentials will lead to enhanced sputtering of pole pieces surfaces. They accelerate positive ions at high energies bringing them physically to remove the atoms on the surface once crashed.

Keeping in mind that in a thermal plasma, the current density decreases exponentially with potential<sup>43</sup>.

The floating potential on an insulating surface exposed to plasma currents is reached when the ion and electron current densities balance and there is no net current to the surface [51].

$$j_e(\phi) = j_e \exp\left(\frac{\phi}{T_e}\right)$$

<sup>43</sup> Ion current varies little with potential.

$$j_e(\phi_f) + j_i = 0 \quad 6.2$$

For conducting surfaces instead, the integral of the currents net is zero.

$$\int (j_e(\phi_f) + j_i) dA = 0 \quad 6.3$$

From these two equations is possible to obtain  $\phi_f$ .

## 6.6 Spacecraft and Solar Array

Because large areas of the solar array are at high potential and not completely insulated from the surrounding plasma, the array can, under some conditions, collect excessive electron currents from the plasma.

In normal flight conditions, the plasma plume does not directly hit the panel or the S/C, then for simple the configuration SA – S/C we take into consideration only the ambient plasma previously described.

Since solar array generated voltages are larger than either electron thermal or ion ram energies, we can assume that positive surfaces collect electrons and negative surfaces collect ions (see Fig. 34).

Spacecraft floating potential is ion current to the chassis balances electron collection to the solar arrays<sup>44</sup>.

Because the spacecraft body has significant exposed conducting surfaces connected to chassis ground, spacecraft with solar arrays float considerably less negative than solar arrays by themselves. The spacecraft will float between 0 V and  $-\phi_{SA}$ .

---

<sup>44</sup> Currents collected from the solar wind environment are negligible and are not further considered.

Because of the bias potential between them, it is possible to see this configuration as a double Langmuir probe.

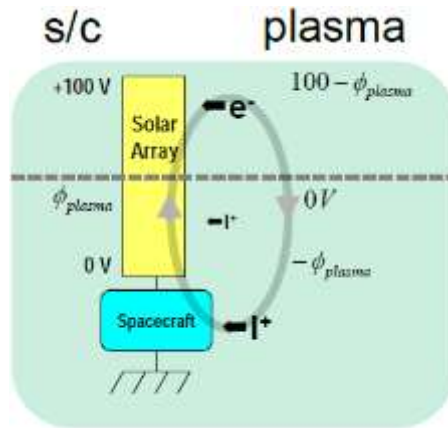


**Figure 33** Ion collection area is on S/C chassis and on the lowest side of the array. Plasma potential is indicated by the dashed horizontal line and the current loop is shown by the grey ellipse (credit by [51]).

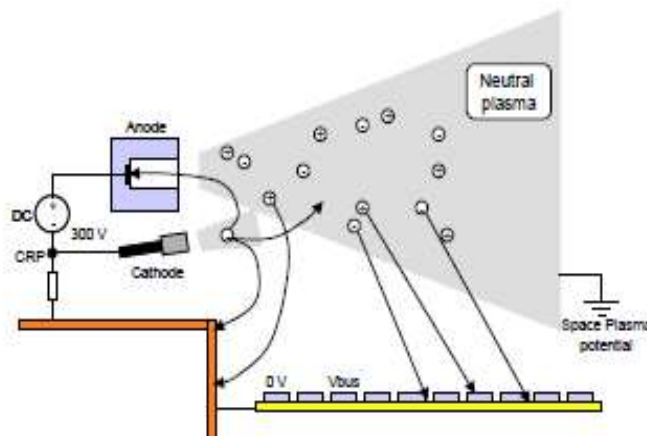


**Figure 34** Charge transfer from neutral plasma plume of the thruster to solar array surface (credit by [56]).

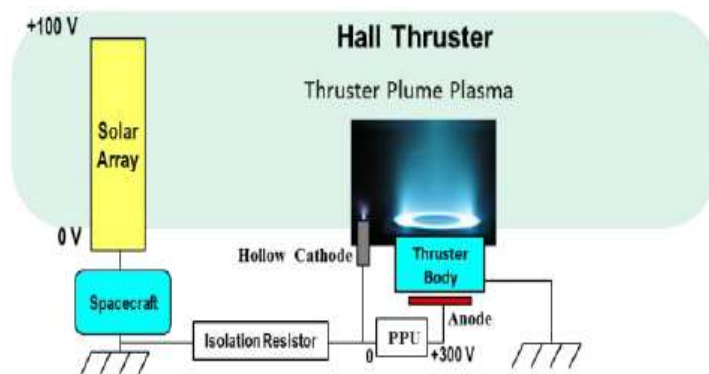


**Figure 35** A simplified diagram of a Hall thruster system is shown. Note that the thruster body is connected to spacecraft chassis (credit by [51]).

Remembering the equations of Section 5.3 and Eqn. 6.3 we now present the formulas to calculate the currents of ions and electrons on a generic element "z" of the problem.

$$I_z = I_{zi} - I_{ze} = \int (j_{zi} + j_{ze}) dA_z \quad 6.4$$

The current densities are integrated on the whole surface of each element.

$$\int (j_i + j_e(\phi)) dA_{SC} + \int (j_i + j_e(\phi)) dA_{SA} = 0 \quad 6.5$$

For each element, the current depends on the plasma (temperature and number density) that laps it. Each element collects both electrons and ions in a much larger quantity depending on the collection area. However, only the electron current depends significantly on the voltage of the surface (until it reaches the saturation zone). The ion saturation current density is the same everywhere (see Eqn. 5.13). This because the ion saturation region is reached almost instantly in every surface. Here because  $j_i = j_{is}$ .

The ion current can be written as

$$I_i = j_i * A = eA \frac{n_s}{2} u_B \quad 6.6$$

where  $A = A_{SA} + A_{SC}$ .

It depends<sup>45</sup> on the Bohm velocity derived in Eqn. 5.12.

The electronic velocity (Eqn. 5.20) gives the electronic current its greater magnitude compared to the ionic one.

$$I_e = \int j_e(\phi) dA = -e * n * \bar{v}_e * \exp\left(\frac{\phi - \phi_P}{T_e}\right) * A \quad 6.7$$

The area varies from element to element. We can use Eqn. 6.7 to calculate the current on all the bodies of the system, appropriately inserting surface and the potential difference with respect to the plasma.

$$I_{eSC} = \int j_e dA_{SC} = -e * n_s * \bar{v}_e * \exp\left(\frac{\phi_{SC} - \phi_P}{T_e}\right) * A_{SC} \quad 6.8$$

---

<sup>45</sup> The two denominator is explained by the pre-sheath theory (allows ion acceleration).  $n_s$  number density of reference outside the sheath  $n_{sheath} \approx 0.5 n_s$ .

$$I_{eSA} = -e * n_s * \bar{v}_e * \exp\left(\frac{\phi_{SA} - \phi_P}{T_e}\right) * A_{SA} \quad 6.9$$

We can use this formula for the solar panel if we assume that the entire panel is all at the same potential  $\phi_{SA} = \phi_{SC} + \Delta V_1$ .

Eqn. 6.5 can be turned in

$$I_i + I_{eSC} + I_{eSA} = 0. \quad 6.10$$

The total electronic current is the sum of the current to the spacecraft and the current from the solar arrays. Replacing the terms in the last equation we find

$$\frac{n_s}{2} e A u_B - e \cdot n_s \cdot \bar{v}_e \exp\left(\frac{\phi_{SC} - \phi_P}{T_e}\right) A_{SC} - e \cdot n_s \cdot \bar{v}_e \exp\left(\frac{\phi_{SA} - \phi_P}{T_e}\right) A_{SA} = 0. \quad 6.11$$

From this equation, is possible to derive the potential either of the plasma or the one of the S/C according to which we have decided to set 0 V as a reference point.

In case we want to get the plasma potential

$$\frac{1}{2} \frac{u_B}{\bar{v}_e} = \exp\left(\frac{\phi_{SC} - \phi_P}{T_e}\right) * \frac{A_{SC}}{A} + \exp\left(\frac{\phi_{SA} - \phi_P}{T_e}\right) * \frac{A_{SA}}{A}$$

$$\frac{1}{2} \frac{u_B}{\bar{v}_e} = \frac{\exp\left(\frac{\phi_{SC}}{T_e}\right)}{\exp\left(\frac{\phi_P}{T_e}\right)} * \frac{A_{SC}}{A} + \frac{\exp\left(\frac{\phi_{SA}}{T_e}\right)}{\exp\left(\frac{\phi_P}{T_e}\right)} * \frac{A_{SA}}{A}$$

$$\exp\left(\frac{\phi_P}{T_e}\right) = \frac{2\bar{v}_e}{u_B} * \left[ \exp\left(\frac{\phi_{SC}}{T_e}\right) * \frac{A_{SC}}{A} + \exp\left(\frac{\phi_{SA}}{T_e}\right) * \frac{A_{SA}}{A} \right]$$

and knowing that

$$\frac{2\bar{v}_e}{u_B} = \sqrt{\frac{2m_i}{\pi m_e}}$$

The plasma potential is then

$$\phi_P = \frac{T_e}{2} * \ln\left(\frac{2m_i}{\pi m_e}\right) + T_e * \ln\left(\exp\left(\frac{\phi_{SC}}{T_e}\right) * \frac{A_{SC}}{A} + \exp\left(\frac{\phi_{SA}}{T_e}\right) * \frac{A_{SA}}{A}\right). \quad 6.12$$

But for our problem, we have set the plasma potential to zero so the formula for tracing  $\phi_{SC}$  results

$$\phi_{SC} = \phi_P + T_e \ln \left( \frac{1}{2} \frac{u_B}{\bar{v}_e} \right) - \Delta V_1 - T_e \ln \left[ \frac{A_{SC}}{A} \exp \left( -\frac{\Delta V_1}{T_e} \right) + \frac{A_{SA}}{A} \right]. \quad 6.13$$

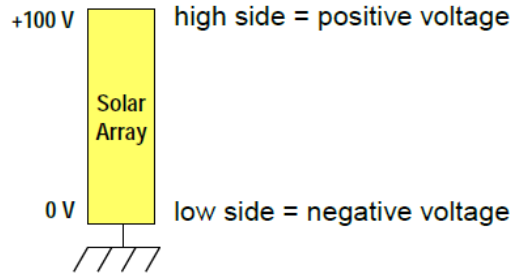
At this point, it is easy to get the solar array potential.

### 6.6.1 Linear Load Panel

If we assume that the solar arrays have a width  $w$  and a length  $L$ , (respectively 3 and 20.8 meters as shown in Chapter 4) and the surface potential varies linearly from  $\phi_{SC}$  to  $\phi_{SC} + \Delta V_1$  along the length of the solar arrays, i.e.

$$\phi_{SA}(y) = \phi_{SC} + \frac{\Delta V_1 \cdot y}{L} \quad \text{with } y = [0:L]. \quad 6.14$$

Figure 36 Linearly charged solar array.



Then the electron current collected by the solar arrays results

$$I_{eSA} = - \int_0^L e * n_s * \bar{v}_e * \exp \left( \frac{\phi_{SA}(y) - \phi_P}{T_e} \right) w dy \quad 6.15$$

which can be rewritten as

$$I_{eSA} = -en_s \bar{v}_e w * \exp \left( \frac{-\phi_P}{T_e} \right) \int_0^L \exp \left( \frac{\phi_{SC} + \frac{\Delta V_1}{L} \cdot y - \phi_P}{T_e} \right) dy.$$

$$I_{eSA} = -en_s \bar{v}_e w * \exp \left( \frac{-\phi_P}{T_e} \right) \frac{T_e * L}{\Delta V_1} \exp \left( \frac{\phi_{SC}}{T_e} \right) * \left[ \exp \left( \frac{\Delta V_1}{T_e} \right) - 1 \right]$$

$$I_{eSA} = -en_s \bar{v}_e w L \frac{1}{100} * \exp \left( \frac{-\phi_P}{T_e} \right) \frac{T_e}{\Delta V_1} \exp \left( \frac{\phi_{SC}}{T_e} \right) * \left[ \exp \left( \frac{\Delta V_1}{T_e} \right) - 1 \right] \quad 6.16$$

Remember that the bias potential  $\Delta V_1$  between the spacecraft chassis and SA is always known.

As Eqn. 6.9 the current collected from space plasmas by solar arrays determines not only the parasitic current power drain on the electrical system but also helps determine the potential at which the spacecraft will float, relative to the surrounding plasma.

We rewrite Eqn. 6.10 updating it with the new equation for the electronic current. With a plasma fixed to 0 V is possible to derive a new writer for the spacecraft potential.

$$\phi_{SC} = T_e \ln\left(\frac{1}{2} \frac{u_B}{\bar{v}_e}\right) - T_e \ln\left(\frac{A_{SC}}{A} + \frac{A_{SA}}{A} \frac{T_e}{\Delta V_1} * \left[ \exp\left(\frac{\Delta V_1}{T_e}\right) - 1 \right]\right) \quad 6.17$$

As a general rule, spacecraft with negative power system grounds and solar arrays with exposed cell interconnects may float up to 90% of the solar array string voltage negative of the plasma they are immersed in. This is because the net current to the spacecraft from the plasma must be zero, and the low mass electrons are easily collected at low positive potentials to balance the (comparatively heavy) ion current collected at high negative potentials.

## 6.6.2 Interconnects

A detailed and systematic investigation of the backflow currents has shown that small interconnector structures on the solar arrays biased to high positive potentials play a dominant role in the formation of spacecraft charging. These results will be a valuable input for the design of satellites.

The interconnects are conducting surfaces and act as biased plasma probes attracting or repelling charged particles.

The potential of the interconnects with respect to the satellite ground varies from approximately 0V at one section end to  $V_{bus}$  ( $\Delta V_1$ ) to the other end.

The contact with the far from the thruster body plasma is only dependent on the solar array cell interconnects.

So not all the surface of the solar array is conductive and able to collect electrons. We, therefore, introduce a first ratio<sup>46</sup>  $\theta = 1/100$  (seen in Eqn. 6.16) which we will multiply for the area of the solar panel.

---

<sup>46</sup> Later we will see that this area is even smaller.

$$A_{SA} * \theta = wL * \frac{1}{100}$$

This involves a limitation of the collected current and brings the results closer to the experimental ones preset by Katz [51]. In the same document is said that the spacecraft grounded conducting surface area usually much greater than the exposed metal area at positive potentials ( $A_{s/c}^{cond} \gg A_{array}^{cond}$ ).

The thing we do not know is precisely how much is inferior.

The balance condition occurs when a slight interconnect area is left at a slightly positive potential with respect to the space plasma; that area then attracts enough electrons to compensate the ions impacting the rest of the interconnects.

Such a phenomenon drives the spacecraft ground potential between floating potential to  $-(\Delta V_1 + \phi_{SC})^{47}$ .

At some location on the array, the generated voltage is equal to the space plasma potential (0 V)<sup>48</sup>.

The cell interconnects that are at voltages above the space potential will attract an electron current which depends upon electron number density in the environment and the voltage difference between the interconnect and the space plasma. Those interconnect that are at voltages below space plasma potential will repel electrons and attract ions current.

This flow of electrons and ions can be considered a current loop in parallel with the satellite electrical load. This parallel current represents a *power loss*.

### 6.6.3 Saturation Region

The saturation current is the maximum current that can flow into the plasma from the solar array circuit if the potential of the collecting solar cell is above the plasma potential.

From the point observed previously the electron current will be saturated<sup>49</sup>. The current will not be collected with the exponential function but it will be constant only and described by  $I_e^{sat}$ .

Equation 6.15 will be replaced by

---

<sup>47</sup> It clear that the variation of the  $\phi_{SC}$  cause the variation of the SA voltage ends.

<sup>48</sup> The problem is, in the complete configuration (Section 6.8), the null location in the code changes in every iteration because of the formulas used until the current equilibrium is found.

<sup>49</sup> When we have saturation? When the potential difference between plasma and surface becomes positive. Exactly at the point where the argument of the exponential ( $\phi_{SC} + \frac{\Delta V}{L} \cdot y - \phi_p$ ) is null, the transition begins.



The thruster body behaves like a probe; the characteristic curve is equal to the same seen in Chapter 5.

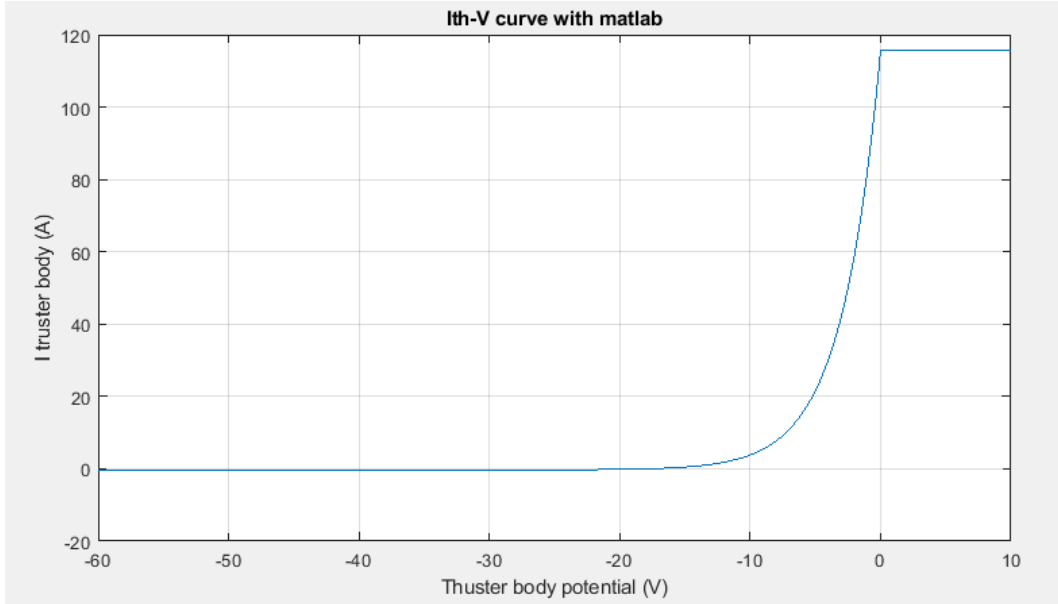


**Figure 39** I-V curve on the thruster body, plotted with the Matlab code in Appendix C. When the potential difference between TB and plasma is zero the curve enters in the saturation region.

For drawing these curves, we need to know both ion and electron current. In [51] the ion current is distinguished for two cases<sup>50</sup>. In case of insulating pole piece surfaces the ion current  $I_{is_{th}}$  is  $\sim 3$  mA but for conducting pole piece is almost 300 mA.

If we suppose to collect the same amount of current like having conducting pole piece, we are able to calculate the effective collecting area of the thruster  $S_{th}$ .

$$S_{th} = 300 \text{ mA} \div \left( e \frac{n_s}{2} u_B \right) = 0.2537 \text{ m}^2$$

Once achieved the surface is possible to calculate the electron current.

$$I_{e_{th}} = -q * n_{th} * \overline{v_{e_{th}}} * \exp\left(\frac{V_{th} - \phi_s}{T_{e_{th}}}\right) * S_{th}$$

---

<sup>50</sup> Laboratory data for magnetically shielded H6MS 6kW 300V 20° with centrally mounted cathode.

## 6.8 Non-Linear Equations System

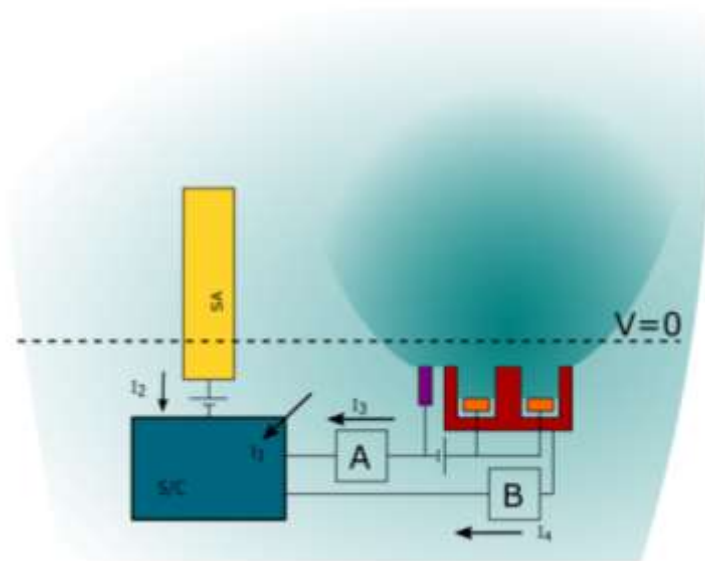


**Figure 40** Schematic model with current direction evaluation.

Each element collects currents. The whole system, however, must float with respect to the plasma, to do this the currents within it must balance themselves. The elements will go to different potentials to make the sum of the currents null.

We take the S/C chassis ground as a reference point and evaluate each current that it collects. In our configuration the currents are four (see Fig. 41):

- $I_1$  is the current between plume and S/C;
- $I_2$  is the current between SA and S/C;
- $I_3$  is the current between cathode and S/C;
- $I_4$  is the current between thruster body and S/C.

The direction of these currents must be clarified. Suppose positive all those that "enters" the spacecraft chassis. Current  $I_2$  is always negative and should be directed from S/C to solar array, being a current passing on a generator (not on a resistance) it remains directed towards the spacecraft.

We can then write an equation that serves as a rule: *the sum of the currents collected by the S/C must give zero so that the whole system can float with respect to the plasma.*

$$\sum_{z=1}^4 I_z = I_1 + I_2 + I_3 + I_4 = 0 \quad 6.19$$

Every single current is based on Eqn. 6.4.

$$\begin{cases} I_1 = I_{eSC} + Ii_{SSC} \\ I_2 = I_{eSA} + Ii_{SSA} \\ I_3 = \frac{(CRP - V_{sc})}{R1} \\ I_4 = -I_1 - I_2 - I_3 \end{cases} \quad 6.20$$

The current arriving from the TB can be also written as

$$I_4 = I_{eth} + Ii_{sth} = I_{eth} + 0.3 A$$

$$I_{eth} = I_4 - 0.3 A$$

$$[I_4 - 0.3] = -qS_{th}n_{th}\overline{v_{eth}} \exp\left(\frac{\phi_{sc} + I_4 * R_B}{T_{eth}}\right) \quad 6.21$$

Where 0.3 A is the collected current with conductive pole piece by the surface of the engine.

From the definition the potential drop on resistance  $R_B$  is

$$\Delta V_B = I_4 * R_B = \phi_{th} - \phi_{sc}.$$

The thruster potential is then

$$\phi_{th} = \phi_{sc} + (I_4 * R_B).$$

Being  $I_4$  function of  $I_2$  we can say that  $\phi_{th}$  is determined by the voltage drop across the isolation resistor from electron current collected by the solar arrays from the plasma plume.

We are now close to finding a solution to our problem.

Rewritten Eqn. 6.21 in the form of Eqn. 6.22.

$$K = q * S_{th} * n_{th} * \overline{v_{eth}}$$

$$\exp\left(\frac{I_4 \cdot R_B}{T_{eth}}\right)^{-1} [I_4 - 0.3] = -K \cdot \exp\left(\frac{\phi_{sc}}{T_{eth}}\right)$$

$$\frac{[I_4 - 0.3]}{\exp\left(\frac{I_4 \cdot R_B}{T_{eth}}\right)} = -K \exp\left(\frac{\phi_{sc}}{T_{eth}}\right) \quad 6.22$$

$$F = e^{-\frac{I_4 \cdot R_2}{T_{eth}}} \cdot (I_4 - I_{s_{tb}}) + K \cdot \exp\left(\frac{\phi_{sc}}{T_{eth}}\right) \quad 6.23$$

We find the  $F$  function characterized by a strong non-linear behaviour due to the resistances<sup>51</sup>. If we combine it with Eqn. 6.19 we obtain a system of non-linear equations (Eqn. 6.24), where every current is a function of  $\phi_{sc}$ .

$$\begin{cases} I_1 + I_2 + I_3 + I_4 = 0 \\ F = e^{-\frac{I_4 \cdot R_2}{T_{eth}}} \cdot (I_4 - I_{s_{tb}}) + K \cdot \exp\left(\frac{\phi_{sc}}{T_{eth}}\right) \end{cases} \quad 6.24$$

The complete code in Appendix C solves this system using the function `fsolve` and gives in one command all the four current in a vector.

The study and the results can be improved with the study of the plume through PIC programs.

The next chapter will present the results and the study done with the described code.

---

<sup>51</sup> It is clear that the  $F$  has a strongly non-linear trend and that depends on the resistances imposed. To see where the zero of the system is, the code add a plot limiting the values on the ordinates.

# Chapter 7

This chapter contains the observations regarding the results obtained with the code described in Chapter 6 and reported in Appendix C.

The chapter is divided into eight successive steps. In every step a variant of the original code will be proposed that can make improvements or even just a new point of view on the problem, to confirm the theoretical observations or to approach experimental data.

Each step will evaluate a certain number of cases in order to cover at least the cases in which the four structural elements of the problem are either completely isolated or directly connected to the S/C. All these cases are reported in Appendix D in the form of tables.

Note that the last two steps (seventh and eighth) are based on a new Matlab code that is coupled with an analysis performed with PicPlus software.

## 7.1 First step

We obtain from the code the 4 currents, potential drops on the resistance plus  $\phi_{SC}$  and  $\phi_{th}$ . In the first step, the results respond to these inputs:

- plasma potential  $\phi_P = 0 V$ ;
- bias potential difference between spacecraft and linearly loaded solar array  $\Delta V_1 = 100 V$ ;
- interconnections area factor  $\theta = 1/100$ ;
- CRP always fixed at  $-15 V$ .

As we said spacecraft dimensions were taken from Chapter 4<sup>52</sup>.

In A and B boxes we choose to put isolator resistors with variable intensity. In Tab. 15 are reported 9 cases of coupling between resistance  $R_A$  and  $R_B$  with different values<sup>53</sup>.

A resistance equal to zero indicates that there is direct contact between the two components (it is like a closed switch). A resistance equal to infinite ( $10^6 \Omega$ ) indicates that the resistance is perfectly insulating (the boxes A and B are like open switches, and there is no current on that branch of the circuit).

---

<sup>52</sup> Is considered the entire surface of the solar arrays necessary for a power demand of 25 kW.

<sup>53</sup> Note that the program can perform all the combinations, we have given these because they are border conditions.

The results on the table in the appendix can confirm these simple observations.

$R_A$ ( $\Omega$ )	inf	inf	0	0	10000	inf	0	10000	1000
$R_B$ ( $\Omega$ )	inf	0	inf	0	0	10000	10000	inf	1000

**Table 15** Input case for A and B resistances. Inf stay for  $10^6\Omega$ .

The most relevant observations are those concerning the trend of the potentials changing the resistances.

The potential of the spacecraft floats always negative compared to the plasma. However, the large size of the solar panel brings it to values close to  $-\Delta V_1$ . The S/C because of this collects a large amount of ions. The current  $I_1$  is in fact ion saturation current in every combination of resistances; in other words, the spacecraft chassis collect only a negligible quantity of electrons.

It is possible to observe that as the resistance becomes less insulating ( $R_A$  and  $R_B$  decrease) the potential of the spacecraft rises (the increase in resistance instead lowers the potential).

When the cathode is isolated, the spacecraft reaches the lowest potentials.

When  $R_A$  becomes null  $\phi_{SC}$  reaches the CRP value (with  $\Delta V_A \sim 2.7 V$ )<sup>54</sup>.

When  $R_B$  becomes null  $\phi_{th}$  reaches the S/C potential. When both the resistance are null  $\phi_{th}$  approaches the CRP value. In this case, currents  $I_3$  and  $I_2$  exceed 2 A.

Variations of  $R_B$  influence mostly  $\phi_{th}$  while  $R_A$  influences more  $\phi_{SC}$ .

The floating potential of the TB is -17.91 V.

If the TB has a  $\phi_{th} < \phi_f$  it will always collect the electrons and ions but  $I_{is} < I_e$  in this case, because it will collect more electrons (see Fig. 38). The resulting current will not be zero as in the isolated thruster but rather negative. The electron current, however, has no weight because it is very small respect to  $I_{is_{th}} = 300 mA$ .

We also note that the signs of  $\Delta V_A$  and  $\Delta V_B$  are obviously related to the directions of currents  $I_3$  and  $I_4$ .

## 7.2 Second Step

The inputs on the second step are:

---

<sup>54</sup> The cases of infinite or null resistances are ideal cases that in reality cannot be reached, here they are at most a mathematical problem.

- plasma potential  $\phi_P$  floats;
- spacecraft potential grounded  $\phi_{SC} = 0 V$ ;
- bias potential difference between spacecraft and linearly loaded solar array  $\Delta V_1 = 100 V$ ;
- interconnections area factor  $\theta = 1/100$ .

We tried here to solve the same problem but we change the reference point. All data are here evaluated respect to the null and constant  $\phi_{SC}$ .

The difference between the two scales is just the spacecraft chassis floating potential.

In every case, the plasma reaches opposite spacecraft's potentials of the previous step.

The CRP is now positive but always 15V less than the space potential and now also equal to  $\Delta V_A$  values.

The plasma potentials in the thruster generated low energy plasma plume at high angles relative to the main thrust beam are 10V ÷ 20V of "cathode common".

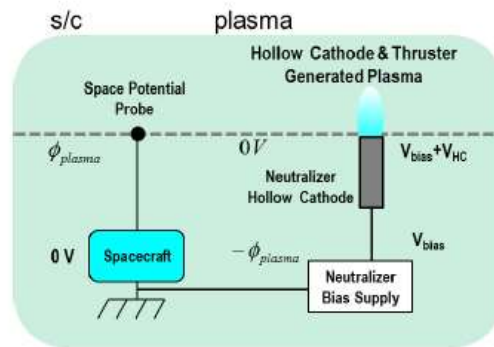


**Figure 41** Thruster body isolated. Cathode grounded with a potential difference respect to the plasma of 15 V (credit by [51]).

When box A is like a closed switch (see Fig. 42) the plasma floats to 17,7 V meanwhile the cathode reference potential almost reach the value of  $\phi_{SC}$ .

Currents and potential differences have no changes.

Instead, values on the thruster body changed becoming equal to  $\Delta V_B$ .

### 7.3 Third Step

Using the same input written for the first step here, we change the contents of boxes A and B. Instead of resistors, they are power supplies. In Tab. 16 are reported the cases evaluated (for the results table look at Appendix D).

By fixing the potential differences there will be an effect directly on the potentials to which the elements of the system are placed. However, we could incur in too high or unreal current values (as in the case of  $\Delta V_A = 0$  and  $\Delta V_B = 100$  V).

The cost in mass would be higher than that of the resistance but we would be able to change the direction of the currents. For example,  $I_2$  which was previously negative is now also positive, which means that the solar panel has a large part of the surface under the plasma potential and collects considerably less electrons.

The only current that always remains equal to its saturation value (0.07385 A) is current  $I_1$ . If we wanted to rediscover the values of the previous steps it is sufficient to insert potential values within  $0 \div 85$  V.

$\Delta V_A$	0	100	0	100	50	60
$\Delta V_B$	0	0	100	100	50	30

**Table 16** Input case for A and B power supply.

## 7.4 Fourth Step

In the fourth step, the code simulates the Direct Drive configuration. The generated potential  $\Delta V_1$  is 300 V, plasma potential is 0 V,  $\theta = 1/100$ , and  $CRP = -15$  V.

The increase in potential involves, as seen a decrease in mass but exposes the entire system to greater damage due to electrostatic charging. The calculated electronic currents are too high to be considered safe (already they were in the first step). Moreover, the spacecraft acquires potentials below -200 V.

If the potential between spacecraft surfaces and the EP generated plasma is large, it may accelerate plasma ions enough to cause significant erosion of spacecraft surfaces by ion sputtering<sup>55</sup>.

In addition to the currents and particle sputtering, arcing can also become a real threat. Flight observations have shown that the large potential differences can lead to arc discharges.

---

<sup>55</sup> Negative chassis potential leads to increased ion energies.

As can be seen from the results in the appendix, wanting to solve the problem of currents, however, results in the problem of the too low potential. Contrarily lifting the potential cause the growth of the electric current. A compromise must be found.

As a precaution, we can say that some configurations must be avoided or otherwise treated with care. In these four steps, for example, the isolation of the cathode from the structure always generates currents on the solar panel above 2 A. These values do not reflect those that can normally be found in these systems.

In [51] a calculation for a notional spacecraft with four 9 kW Hall thrusters shows the solar arrays are expected to collect less than 10 mA of electrons, far less than the 300 mA of ion saturation current for a single thruster body.

What we can improve on this point is the solar panel itself. In fact, we do not know how much this conductor is or rather, how much the interconnections cover the surface. It depends on the type of solar panel mainly. So the only factor we can change now to get closer to the data in [51] is  $\theta$ .

## 7.5 Fifth & Sixth Step

(Input sixth step 0 V,  $\Delta V_1 = 300$  V,  $\theta = \frac{1}{10000}$ , CRP = -15V).

(Input fifth step 0 V,  $\Delta V_1 = 100$  V,  $\theta = \frac{1}{10000}$ , CRP = -15V).

Modern geosynchronous communications satellites are typically covered with conducting surfaces, to prevent surface potential differences and arcing.

The only non-conducting surfaces usually are the solar cell cover glasses<sup>56</sup>.

In flight, solar array collection will not play a significant role because of cover glasses. The thruster body ion current, about 300 mA, is much greater than the maximum solar array electron collection, less than 10mA.

The fifth and sixth steps evaluate the changing of  $\theta$  from 1/100 to 1/10000 with the purpose to reducing the collected currents in a nominal drive condition (100 V) and in direct drive condition (300 V).

Reducing the coding area so much, however, leads the results to no longer being influenced by the value of  $\Delta V_1$ . For both conditions (normal and direct), the results are practically the

---

<sup>56</sup> The more isolated is the solar array is, the more it weights.

same. Currents and voltages are reduced and configurations that were previously discouraged now seem possible.

To note is the fact that the S/C if the TB is not isolated, floats to cathode potential. If TB is isolated  $\phi_{SC}$  goes at higher potentials because potential difference became negative (on resistances).

The electrons not collected by the solar panel will partially end up on the spacecraft.

The spacecraft will result with a “positive” area greater.

It will collect therefore a larger current of electrons that will subtract from ion saturation current, and  $I_1$ , which until now had remained constant, will dim its value.

## 7.6 Plume Software Analysis

Analysis of electric propulsion plasma plumes constitutes a difficult task, due to the complexity and number of phenomena taking place in the plume formation and downstream expansion. Usually, a triple approach combining ground testing, in-space measurements and modelling must be followed to correctly describe the plume.

For the simulation of the electric propulsion plasma plume, the particle-in-Cell (PIC) software PICPlus (Appendix E) is used.

The software models the fluid dynamics of Hall thruster plume by sophisticated Direct Simulation Monte Carlo codes.

It is capable of direct simulation of propellant ions and neutral atoms coming from the thruster, indirect simulation of background and fluid dynamic treatment of the electrons<sup>57</sup>.

The plume flow field can be computed self-consistently with the spacecraft geometry or, as is the case here, computed independently and then overlaid onto the geometry.

The tracking of  $n_i$  and  $T_i$  into the plume allows this programs to be useful (apart from the study of charging) for:

- detection of unexpected torque disturbances;
- detection of sudden heat transfer, and arising of the temperature of surfaces;
- computation of erosion rates and contamination using sputter rate database and maps.

---

<sup>57</sup> In this method, the collisions of the highly energetic ions with the background neutrals are explicitly simulated, which enables to assess the influence of the background gas pressure onto the plume. Furthermore, the influence of the plasma potential on the plume characteristics is respected. This enables the change of boundary conditions for space and at the spacecraft surfaces.

That said, it can provide guidance for the design of space vehicles.

The next two steps of the study derive from the union of the Matlab code, used up to now, with the simulations carried out through PIC software developed by SITAEEL.

### 7.6.1 PICPluS Simulations

The purpose of the simulation is an investigation of possible differences in the plume interaction with the deployed solar panel when this is in normal drive condition or in direct drive condition.

We now briefly describe the steps that allowed us to discretize a proper plume plasma.

First of all, there is the construction of the tug model with Gmsh. The architecture described in chapter 4 was chosen as a model.

The geometry of the spacecraft is illustrated in Fig. 43. The HT-20k thruster, as seen from the images, was mounted with the exhaust axis inclined at  $45^\circ$  with respect to the directions of the solar panel, in order to simulate the worst possible condition, i.e. the one in which part of the plume touches directly the panel.

A panel with new dimensions:  $2.216\text{ m} \times 8.19\text{ m}$ .

This allowed us to concentrate the analysis on a panel of reduced dimensions compared to the original, in order to simulate only the area affected by more dangerous plasma and to lighten the computational cost<sup>58</sup>.

The 3D mesh of the model with the introduction of the boundary conditions was then loaded through a pre-processing on PICPluS.

---

<sup>58</sup> For a panel of 20.8 m we would have to enlarge the far field increasing exponentially the convergence times of the simulation.

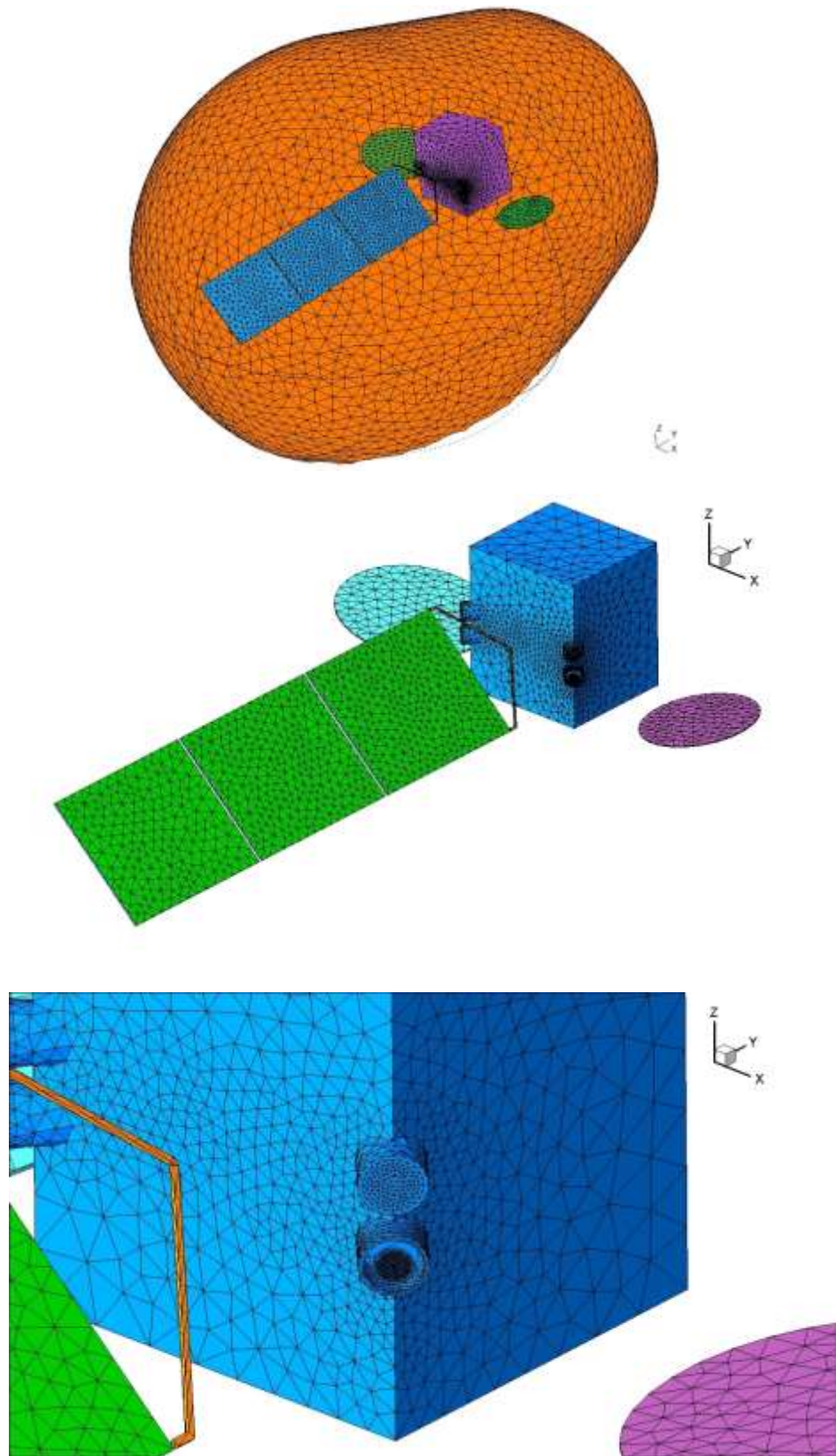


**Figure 42** In order top-down are shown the: Gmsh model in the far field environment, the mesh on the model of the tug and the model of HT20k near the solar panel.

Lastly, we added the data of the engine operating point, summarized in the Tab. 8 (in Chapter 3).

The output of the simulation is a “.tec” file which is read with special visualization programs like Tecplot or Paraview (see Fig. 44, 45).

The area of concern is the effect of the high energy plume on the large solar arrays. With the help of this program we are able to extract “.dat” files that contain all the information of the plasma in contact with the solar panel.

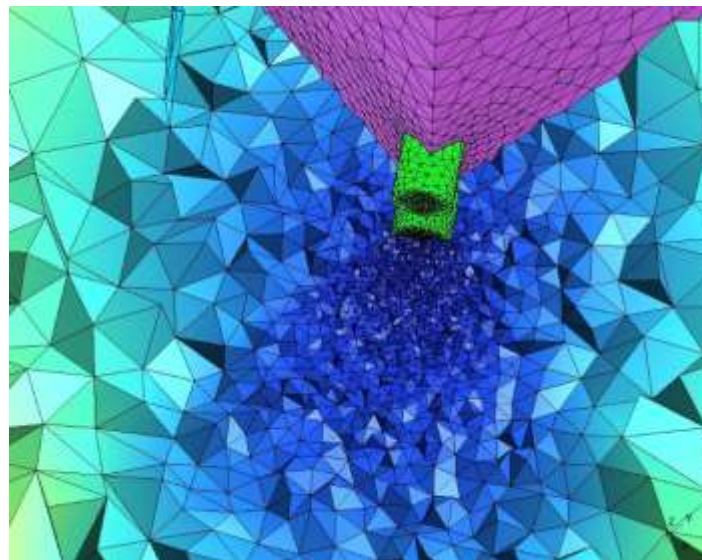
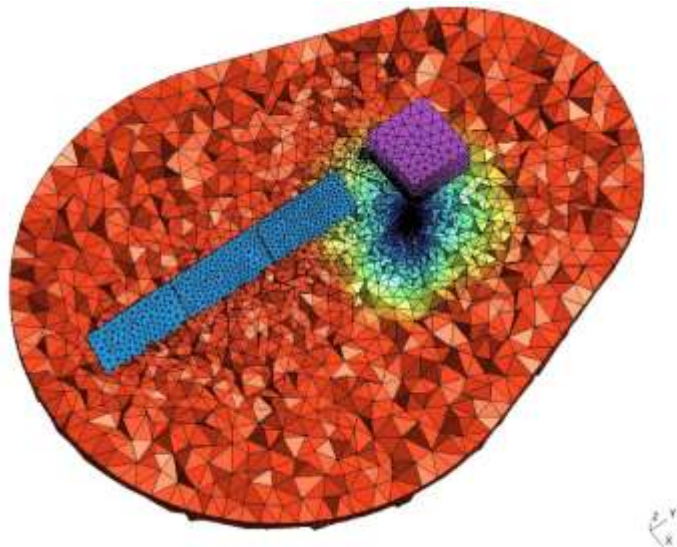


**Figure 43** The computed plume in a clipped section of Tecplot evaluation on the surfaces of the elements of the mesh. Density decreases as we move away from the thruster (credit by SITAEI).

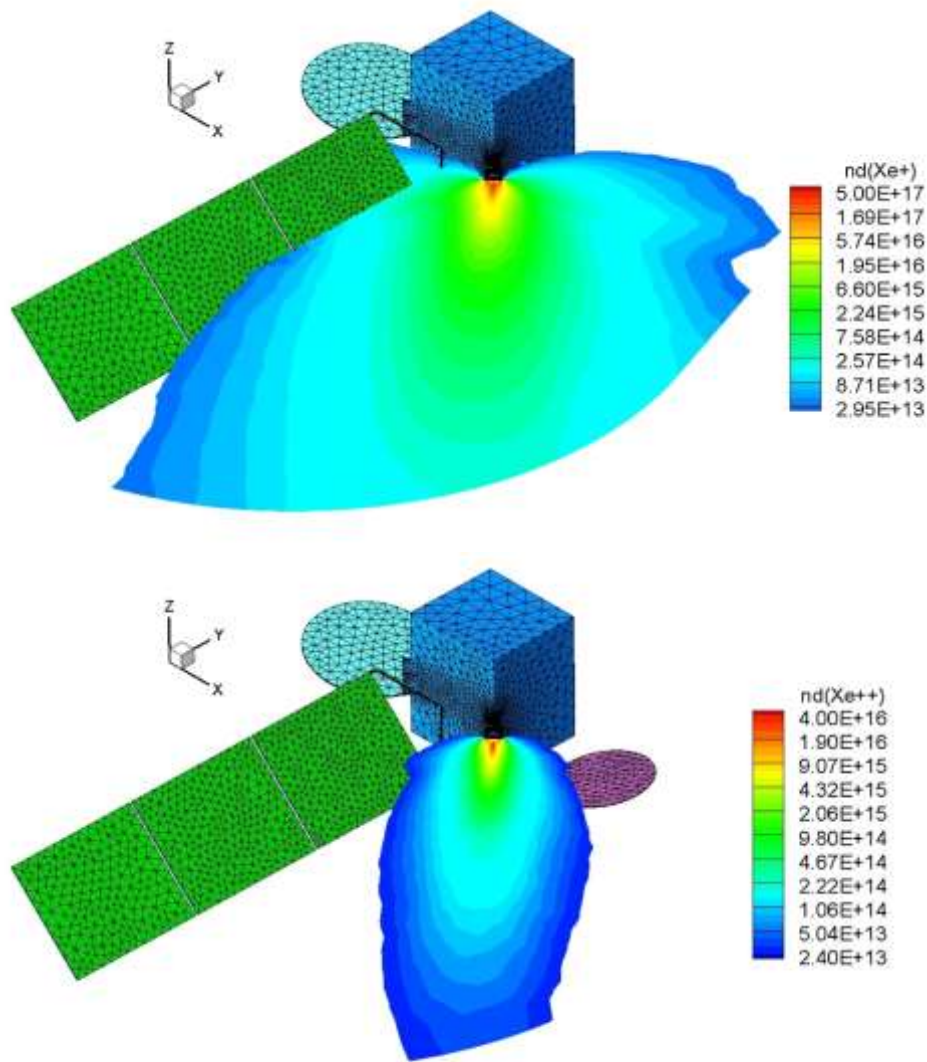


**Figure 44** The plume is computed 2D in terms of single (top) and double (down) charged ions distributions measured in number density (nd).  $Xe^{++}$  are concentrated in the axial region of the plume (credit by SITAEL).

## 7.6.2 Max Solar Array Electron collection from High Power Thruster Plume

A new Matlab code that uses “.dat” files is based on some data provided by Katz during the presentation of [51] in order to re-evaluate the current actually collected by the SA, which in our problem is called  $I_2$ .

Katz suggests a current density  $j_{plasma}^{n_e=10^{14} m^{-3}}$  calculated for an ideal plasma characterized by a number density of  $10^{14} m^{-3}$ .

$$j_{plasma}^{n_e=10^{14} m^{-3}} = 1.58 \frac{mA}{m^2} \quad 7.1$$

$$I_{2MAX} = j_{plasma}^{n_e=10^{14} m^{-3}} \times \frac{\int_{wing} n_e \cdot dA}{10^{14} m^{-3}} \quad 7.2$$

The maximum current collected varies from 1.4 mA to 5.2 mA. For Katz this depends on:

- the shape and dimensions of the panel;
- total number of cells and cells per string;
- area of a single cell, in fact, smaller cells have more interconnects and thus large effective collection surface;
- plasma temperature at the highest number density.

The Matlab code (showed in the second part of Appendix C) extracts the needed data from Tecplot and inserts them into Eqn. 7.2

Current  $I_{2MAX}$  then will be inserted in the previous code to see how this varies the balance within the system.

## 7.7 Seventh & Eighth Step

Input for these steps are plasma 0 V,  $\Delta V_1 = 100 V$  and  $300 V$ , with PICPluS evaluation of  $I_{2MAX}$ .

For nominal drive condition  $I_{2MAX}$  is equal to  $-0,0019 A$ .

For direct drive condition  $I_{2MAX}$  is equal to  $-0,0018 A$ .

They are equal and similar to the current collected in Katz paper<sup>59</sup>.

The introduction in the code of the new current has the same effect as the lowering of the interconnects coefficient  $\theta$ , it removes the dependence of the entire circuit from the bias potential between S/C and SA.

The steps 7th and 8th, in fact, have the same values for each case. This avoids the appearance of too negative  $\phi_{SC}$  and large currents.

---

<sup>59</sup> In the change of the two conditions from 100 to 300 V we did not change the operative point of the engine.

The particle *distribution* is not affected by the different delta of potential (100 - 300 V) on the panel because any delta of potential is shielded by the plasma (for distances of the length of Debye) this is called *Debye shielding*.

Different delta of potential changes the *number* of particles going on the solar array and on the S/C<sup>60</sup>. This is explained also by the growth of the sheath thickness on surfaces with higher potential. The larger the collecting surface the more particles are captured.

This affects the ions threshold energy for passing into the sheath layer and by consequence the sputtering events<sup>61</sup>.

The calculation of the maximum electron current considers the whole panel at a positive potential with respect to the plasma without defining a negative and a positive saturation region.

The actual maximum current collected should, therefore, be lower.

To verify this we take a random combination of resistors  $R_A$  and  $R_B$ :

- 1) we enter the new  $I_2$  current in the code described in chapter 6.
- 2) we take note of the extremes to which the increasing potential is placed on the panel and look for the exact value of the coordinate in which the potential is null along the length.
- 3) we find the barycenter of each triangle of the mesh to understand which ones are placed on the right or left of the coordinate.
- 4) with the data files deriving from Tecplot is possible to recalculate the electron current collected only from the positive part of the solar array (that is, after the coordinate found in 2), this is slightly lower.

Then repeat the points 1) and 2) we realize that the extremes do not vary; this suggests that the current we found in point 4) is the current actually collected.

For the 7th step (solar array from -14.3 to + 85.7 V) the current found after in point 4) is -0,0016 A.

For the 8th step (solar array from -14.3 to + 285.7 V) the current found after in point 4) is -0,0018 A.

The contribution due to the variation of the saturation region does not change the current value drastically.

---

<sup>60</sup> The difference in potential on the panel affects more the collection of charged particles than their distribution.

<sup>61</sup> Before the simulation we were "afraid" that sputtered particles could be counted a second time inside the plasma, thus varying the local number density values. This does not happen.

## 7.8 Study on the Katz Constant

These last two cases were finally used for a more accurate study of the constant presented by Katz in Eqn. 7.1

$$j_{plasma}^{n_e=10^{14} m^{-3}} = \alpha * n_o v_o q.$$

Where  $\alpha = \cos \theta$ ,  $n_o = n_e = 10^{14}$ ,  $v_o \propto T_e = 1eV$ .

This helps us to find the value of  $\alpha$  that only depends on the composition of the solar array. The current was therefore calculated by inserting the point-by-point values of current density and temperature  $T_e$  deriving from the Tecplot software.

The new current density is no longer characterized only by  $n_e$  and it is automatically differentiated when on the surface of the panel it meets a potential above the plasma potential.

This value must then be multiplied by the area of the mesh element. In Fig. 45 we can see that the current grows linearly with the area until it becomes saturated.

The current collected from the entire panel surface calculated in this way was

for the seventh step:  $I_{2MAX} = - 0.0017 A$  and

for the eighth step:  $I_{2MAX} = - 0.0016 A$ .

Identical values in the two cases with potentials different and also equal to those calculated within the previous study

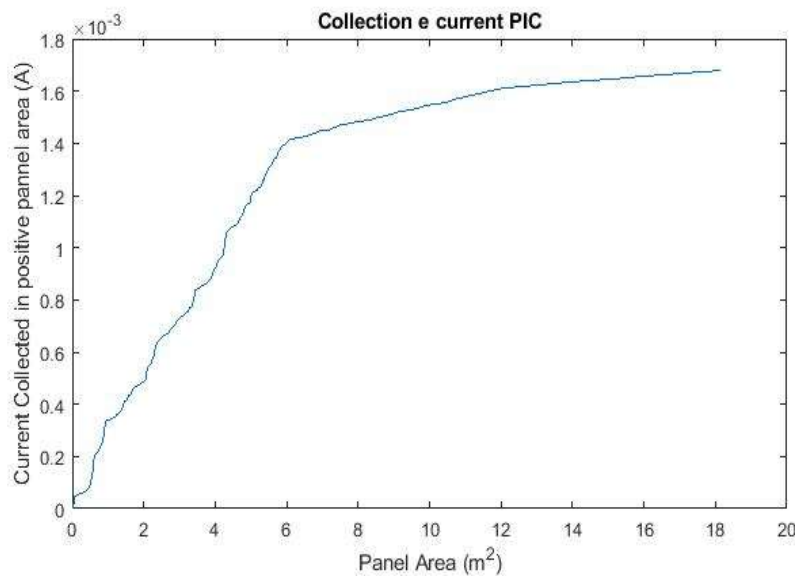


**Figure 45** Collection of electron current with extraction of local number density and temperature of the plasma.



# Future Works

Possible expansions and improvements of the study carried out here can be divided according to the aspects that should be investigated.

A first expansion may be that related the study of tug configurations with the purpose of:

- 1) Perform a complete optimization analysis of the trajectories, integrating the periods of eclipse and oscillations that have been neglected in this Master thesis. With the hope of obtaining more realistic data in terms of mission durations and propellant consumption. Changing even the trajectories themselves and the mission parameters.
- 2) To quantify all the advantages (direct and indirect) deriving from a Direct Drive configuration in order to provide a better estimate of the available payload. Moreover, it would be interesting to investigate the aspects concerning other critical issues of the Direct Drive approach as the ignition and performance regulation problems.

In order to improve the simulations and the code, the aspects concerning the interaction with the HT20k plume could be further characterized.

- 3) The sheath thickness is that are important in determining the collected current. As the voltage is raised, either too large positive or large negative values with respect to the plasma, the sheath thickness increases according to Child's law and, consequently, the effective collecting area also increases. The same effect can be noticed in the interconnections of the solar array. By removing the infinite surface hypothesis (for the Langmuir probes it is equivalent to the case when  $h_{sheath} \sim r_{sphere}$ ) then the saturation current is not constant but it grows when the surface of the potential increases.
- 4) A further improvement of the analysis can be obtained if the real cathode behaviour is included in the model. In particular, if we can characterize the cathode CRP with respect to the emitted current (depending on the thruster working point), the analysis will give more representative results.
- 5) Study the differences between floating and grounded CRP and perform a characterization of the beam stray current.

The latter point deserves a better explanation.

On most spacecrafts that use electric propulsion, the typical grounding approach (*Floating CRP*) implements galvanic isolation between the Cathode Return Potential (CRP) and the spacecraft Electrical Power System (EPS) Ground.

Any beam stray current,  $I_{stray}$ , which may “leak” to the EPS Ground, through a plurality of complex diffusion and interaction mechanisms involving some of the spacecraft conductive surfaces exposed to the plasma environment, would then result in a voltage drop across resistances.

Such voltage drop would thus move the CRP in the direction of reducing  $I_{stray}$ , until a point of equilibrium is finally achieved.

Typically, at equilibrium, the CRP can reach few tens of volts negative with respect to the EPS Ground, but also the case with CRP few volts positive cannot be entirely ruled out (as shown by measurements performed onboard during the SMART-1 mission [62]).

In fact, given a certain value of resistance, the actual value of  $I_{stray}$ , will depend on the value of relevant environmental variables: plasma environment, orbit altitude, sunlight or eclipse, solar activity and season

In the DD configuration, the typical grounding approach is *Grounded CRP*.

This approach connects directly the HET Cathode Return Potential to the Spacecraft Ground potential.

Such a condition might expose the S/C to the risk of potential damages resulting from too large  $I_{stray}$  currents.

The  $I_{stray}$  problems exist also in a vacuum chamber environment.

Experiments on these effects are still ongoing in SITAEL. A new Matlab code has already been implemented, but further tests are necessary for the validation of the results (see Figure 47).

Finally, we want to highlight the intention to rewrite the Matlab code in Fortran to make it part of the PICPluS software, in order to solve similar problems with a single interface.

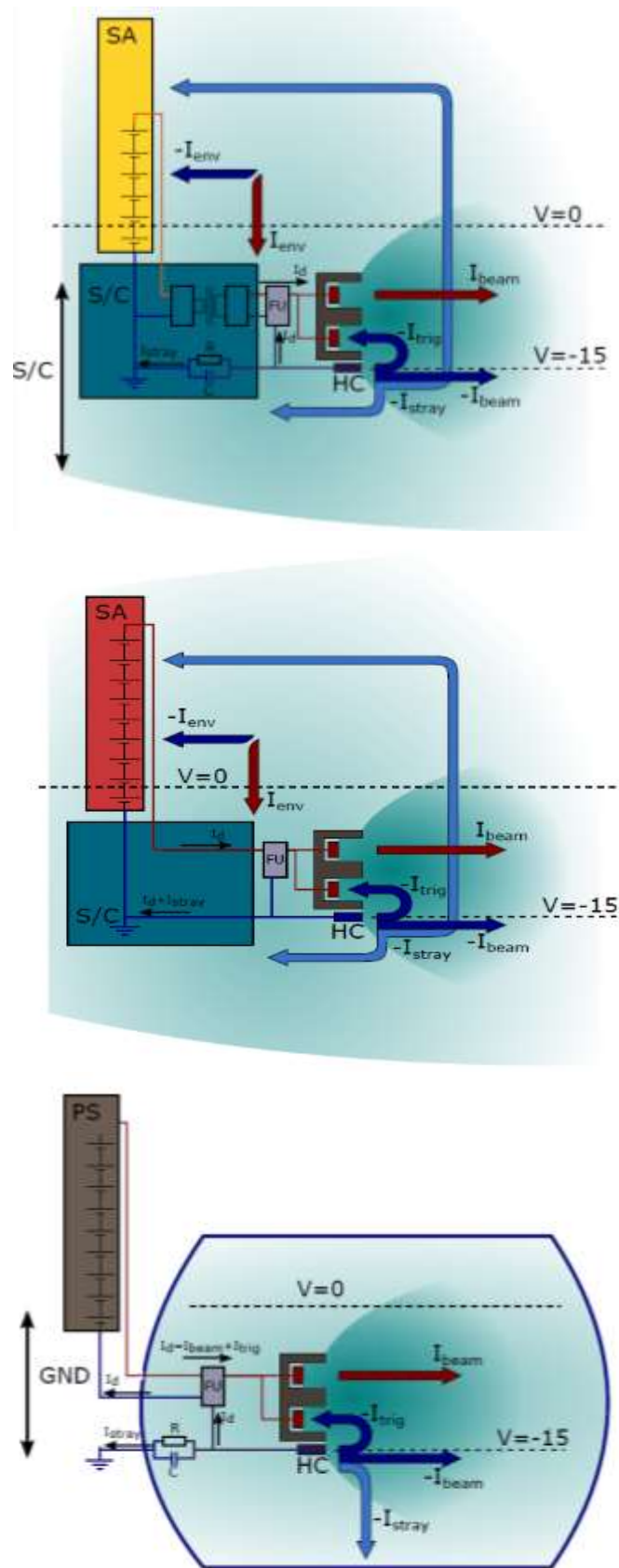


**Figure 46** Future study on the beam stray current in different environment: spacecraft PPU in flight (top), spacecraft DDU in flight (middle), vacuum chamber (bottom).

# Conclusions

The thesis developed is a multidisciplinary work aimed to study the interactions between the plume of the plasma thrusters and the S/C systems, with a specific focus on the electrostatic charging of surfaces.

This is not only one of the most interesting aspects of design for any SEP vehicle but also one of the critical issues to overcome if we want to apply a Direct Drive configuration, i.e. a direct non-isolated connection between the EP system and the solar arrays.

To analyze the problem, a simple theoretical description and a numerical tool were developed, which could provide currents and voltages of the most significant elements of space vehicle with Hall Effect thrusters.

This was possible first by paying particular attention to the theoretical aspect of the problem (see Chapters 1, 2, 5) and then through a preliminary mission analysis aimed at sizing a LEO-GEO tug (see Chapter 3 and 4).

The present study on electric propulsion and, in particular, on the Hall Effect engines has shown that the HT20k is a suitable primary propulsion system even for missions that a few years ago were prerogative of chemical propulsion. This is mainly due to the advantages of propellant consumption.

The HET application is of great interest for a particular space vehicle: the Orbital Maneuvering Vehicle (OMV) or tug. To complete a LEO-GEO transfer, the propulsion system must carry out what is commonly called EOR.

The analysis with the STK software allows the assessment of transfer time and propellant consumption for three mission architectures with different take-off mass and engine operative point.

The complete evaluation with STK is shown in Appendix A.

In order to evaluate the advantages of a DD configuration, we have configured the first architecture with a PPU and the second with a DDU.

The considerable increase of the specific impulse in the in direct drive configuration allows the second case to arrive in GEO a week in advance with respect to the tug with PPU, which completes the outward journey in 120 days. This, however, entails a cost of propellant of additional 150 kg in DD (assuming also a return in LEO).

The cost is dampened by the mass benefits resulting from the elimination of 92% of the mass of the PPU and from the introduction of the HVB at 300 V. These changes that are the basis of the Direct Drive approach, broadly described in Chapter 4.

The maximum mass gain was estimated to be larger than 160 kg for the third tug architecture. Considering only the advantages derived from the simplification of the PPU for this architecture we obtained, a total mass of 6000 kg, 4 HETs and an available power of 50kW.

For the smallest tug (25 kW and a total mass of 2800 kg), the analysis of systems and masses was carried out together with the sizing of tug body and solar array.

The sizing of to these two elements mark the end of the *first part* of the thesis. At this point, even though the technology maturity of several subsystems need to be improved in order to build a high-power SEP tug, there appear to be no major technical hurdles that would prevent this vehicle from becoming a reality.

The *second part* starts from Chapter 5, which is dedicated to the description of the phenomena affecting surfaces in contact with a plasma. The Sheath Theory and the behaviour of the Langmuir probe in a plasma are at the base of the developed numerical code that simulates the (completely reported in Appendix C).

Understanding how the thruster body, SA, S/C chassis and cathode behave in contact with the plume plasma was fundamental for the definition of the model equations. The separation between ion and electron current density, the concept of saturated current and the balance of currents in a body (or a set of bodies) immersed in a plasma are just some of the key concepts described in Chapter 6.

The combination of these concepts leads us to a system of non-linear equations, which allows to find the potential of each of the four elements mentioned above.

The formulated code is simple yet flexible. It is possible in fact:

- to insert values of insulating resistors or applied voltages between elements,
- to modify the plasma properties, e.g. the number density and electron temperature,
- to enter any size for TB and SA,
- to change the conductivity of the solar panel.
- to modify the bias potential between SA and TB, e.g. at 100 V or at 300 V (DD).

Various tests have been done to simulate conditions similar to measured experimental and theoretical data. Each of these is reported in Appendix D and commented in Chapter 7.

Then, analysis were carried out for different SA voltages in combination with PICPlus, which simulates the HT20k plume around the solar array.

The value of the collected current depends on the degree of conductivity of the panel, i.e. on its composition and on how much surface is composed of interconnects.

The electron current collected by the solar panel is small (1.8 mA) and, as expected, the difference in potential bias does not involve any difference in the balance of the currents. We can state that the potential of the panel does not interfere with the distribution of particles, but only on their collection. In particular, a low potential on surfaces could lead to a substantial increase in the energy of the ions collected, which can cause massive sputtering.

Apart from observing the elements' potentials, particular attention must be paid to the currents between the different S/C elements and to the large potential differences that may lead to arching.

In general, each current must be controlled. In fact, just a few mA on insulating resistors ( $M\Omega$ ) are enough to create unexpected potential peaks and shut down the systems.

Hence, an accurate and reliable model for the calculation of the potential of the different S/C elements is essential for the design of future satellites.

The characterization and the investigation of the plume are therefore paramount for understanding HET devices and assessing the mechanical and electrical interactions of the exhaust plasma plume with the spacecraft itself.

Furthermore, understanding the dependence of the plume evolution with the main operating parameters allows to optimize the thruster design and to reduce potential risk associated with plume interactions.

# Bibliography

- [1] Robert G. Jahn, “Physics of Electric Propulsion”, Professor of Aerospace Sciences, Princeton University, 1968
- [2] Dan M. Goebel and Ira Katz, “Fundamentals of Electric Propulsion: Ion and Hall Thrusters”, Jet Propulsion Laboratory, California Institute of Technology, 2008
- [3] J. A. Bittencourt, “Fundamentals of Plasma Physics”, National Institute for Space Research (INPE), Brazil, 2004, third edition
- [4] Michael A. Lieberman, Allan J. Lichtenberg, “Principles of Plasma Discharges and Materials Processing” – second edition, Wiley-Interscience, 2005
- [5] Mukund R. Patel, “Spacecraft Power Systems”, 2005
- [6] Wiley J. Larson, United States Air Force Academy and James R. Wertz, Microcosm, Inc., “Space Mission, Analysis and Design” - Third Edition, United States Air Force Academy, 2005
- [7] Francis E Chen, “Introduction to Plasma Physics and Controlled Fusion” - second edition, Electrical Engineering Department, School of Engineering and Applied Science, University of California, Los Angeles, California, 1974
- [8] F. Paganucci, T. Andreussi, Electric Propulsion I: Lectures notes
- [9] Jean-Pierre Boeuf, “Tutorial: Physics and Modelling of Hall thrusters”; Citation: Journal of Applied Physics 121, 2017; Published by the American Institute of Physics.
- [10] Robert G. Jahn, Edgar Y. Choueiri, “Electric Propulsion”, Princeton University, 2002
- [11] Daniela Pedrini, Fabrizio Paganucci, University of Pisa, Riccardo Albertoni, Mariano Andrenucci, SITAEL S.p.A., Pisa, “Experimental Characterization of a Lanthanum Hexaboride Hollow Cathode for Five-Kilowatt-Class Hall Thrusters”, Journal of Propulsion and Power, Vol. 32, No. 6, November–December 2016
- [12] Joseph Homer Saleh, Fan Geng, Michelle Ku, Mitchell L. R. Walker II, “Electric propulsion reliability: statistical analysis of on-orbit anomalies and comparative analysis of electric versus chemical propulsion failure rates”, School of Aerospace Engineering, Georgia Institute of Technology, Atlanta, USA, 2017
- [13] Ian J. E. Jordan, “Electric Propulsion: Which One for My “Spacecraft?”, Space Systems I course at JHU, Whiting School of Engineering, December 6, 2000.
- [14] Alexander V.Semenkin, "High-Power Hall Devices: Status and Current Challenges", TSNIIMASH, Moscow, Russia.
- [15] James H. Gilland, “Mission and System Optimization of Nuclear Electric Propulsion Vehicles for Lunar and Mars Missions”, Sverdrup Technology, Inc., NASA Lewis Research Center, Brookpark, Ohio. IEPC 1991-038

- [16] Andrey A. Shagayda, “On Scaling of Hall Effect Thrusters”, Keldysh Research Center, Moscow, Russia. Presented at the 33rd International Electric Propulsion Conference, The George Washington University, Washington, D.C., USA, October 6 – 10, 2013 IEPC-2013-056
- [17] Matteo Laterza, Daniele Aprile, “Progetto Di Un Propulsore a Effetto Hall di Classe 30 kW”, Tesi di Laurea Specialistica, Corso di Laurea in Ingegneria Aerospaziale, Università Degli Studi Di Pisa, 2011/2012
- [18] L. E. Zakharenkov, A.V. Semenkin, A.E. Solodukhin, “Concept of Electric Propulsion Realization for High Power Space Tug”, SSC Keldysh Research Centre, Moscow, Russia. 2016
- [19] <https://directory.eoportal.org/web/eoportal/satellite-missions>
- [20] A. Piragino, Development of a 20kW-class Hall effect thruster, Master’s thesis University of Pisa, 2015-2016.
- [21] [http://help.agi.com/stk/index.htm#seet/seet\\_overview.htm](http://help.agi.com/stk/index.htm#seet/seet_overview.htm)  
<https://www.agi.com/products/engineering-tools/space-operations>
- [22] James E. Pollard, “Simplified Approach for Assessment of Low-Thrust Elliptical Orbit Transfers”, The Aerospace Corporation, Los Angeles, CA
- [23] J. E. Pollard, “Simplified Analysis of Low-Thrust Orbital Maneuvers”, Propulsion Science and Experimental Mechanics Department, Space Materials Laboratory, August 2000
- [24] M. Mammarella, P. M. Vernicari, N. Viola, “Design and Cost Analysis of High-Power Solar Electric Propulsion Platforms”, Department of Mechanical and Aerospace Engineering, Politecnico di Torino. Space Propulsion 2018, Seville, Spain, 14 – 18 May 2018
- [25] Kalina K. Galabova, “Architecting a Family of Space Tugs based on Orbital Transfer Mission Scenarios”, B.S. in Mechanical Engineering/Aeronautical Systems, United States Military Academy, Massachusetts Institute of Technology, February 2004
- [26] W.D. Deininger, Bryce Unruh Scott Mitchell, John Dankanich, “Solar Electric Propulsion Demonstration Mission Trajectory Trades”, Ball Aerospace & Technologies Corp., Conference Paper, 33rd International Electric Propulsion Conference, at the George Washington University, Washington, D.C., USA, October 2013.
- [27] William D. Deininger, Scott Enger, Joe Hackel, J. C. Soto, Bryce Unruh, “Solar Electric Propulsion Demonstration Mission Baseline” Ball Aerospace, Boulder, CO, USA. Dave Murphy, ATK Aerospace Systems, Goleta, CA, USA, Kristi DeGrys, Aerojet Rocketdyne, Redmond, WA, USA. Presented at the 33rd International Electric Propulsion Conference, The George Washington University, Washington, D.C., USA, October 6 – 10, 2013
- [28] Steven R. Oleson, “Mission Advantages of Constant Power, Variable Isp Electrostatic Thrusters”, Glenn Research Center, Cleveland, Ohio, November 2000
- [29] Christopher S. Loghry “LEO to GEO (and Beyond) Transfers using High Power Solar Electric Propulsion (HP-SEP)”, Moog Inc, Chatsworth, CA, USA & Steven Oleson, Jeffrey Woytach, Michael Martini, David Smith, James Fittje, John Gyekenyesi, Anthony Colozza, James Fincannon, Aimee

- Bogner, Robert Jones, Thomas Packard, Elizabeth Turnbull, NASA Glenn Research Center, Cleveland, OH, USA. Presented at the 35th International Electric Propulsion Conference, Georgia Institute of Technology, Atlanta, Georgia, USA, October 8 – 12, 2017
- [30] Nicolas Arcis, A. Bulit, A. Varinois, J.-M. Ruault, M. Gollor, J. Roggen, K. Ruf, “D2.2 Database of EPS key requirements and technical specifications for current and future missions”, Centre National d’Etudes Spatiales, 2015
- [31] Rodney L Burton, University of Illinois, Urbana-Champaign; Monika Auweter-Kurtz, Steinbeis Hochschule Berlin; W.D. Deininger, Ball Aerospace & Technologies Corp., “Optimized Low-Thrust Orbit Transfer for Space Tugs”, *Journal of Spacecraft and Rockets*, January 200
- [32] Martina Mammarella, “High Power Hall Effect Thruster Subsystem for Space Transportation and Exploration”, *Spacecraft Preliminary Design*, Technical Note 5, Politecnico di Torino, 2018
- [33] Martina Mammarella, “High Power Hall Effect Thruster Subsystem for Space Transportation and Exploration”, *Spacecraft Power and Mass Budget*, Technical Note 8, Politecnico di Torino, 2018
- [34] John Steven Snyder, John R Brophy, Richard R. Hofer, Dan M. Goebel, Ira Katz, “Experimental Investigation of a Direct-Drive Hall Thruster and Solar Array System at Power Levels up to 10 kW”, Jet Propulsion Laboratory, California Institute of Technology, Pasadena, CA. 48th AIAA/ASME/SAE/ASEE Joint Propulsion Conference & Exhibit, 2012
- [35] Henry W. Brandhorst, “Direct-Drive Performance of a T-100 HET powered by Triple Junction, High-Voltage Concentrator PV Array” Jr., Steve R. Best, Julie A. Rodiek, Space Research Institute, Auburn University, AL, USA; Mark J. O’Neill, Entech Solar, Inc., Ft. Worth, TX, USA; Michael F. Piszczor, Jr., NASA Glenn Research Center, Cleveland, OH. 46th AIAA/ASME/SAE/ASEE Joint Propulsion Conference & Exhibit, Nashville, TN, 25 - 28 July 201
- [36] John R. Brophy, Muriel Noca, “Electric Propulsion for Solar System Exploration”, Jet Propulsion Laboratory, California Institute of Technology, Pasadena, California. *Journal of Propulsion and Power*, Vol. 14, No. 5, September –October 1998
- [37] John Brophy, Robert Gershman, Nathan Strange, Damon Landau, Raymond Merrill, and Thomas Kerslake. "300-kW Solar Electric Propulsion System Configuration for Human Exploration of Near-Earth Asteroids", 47th AIAA/ASME/SAE/ASEE Joint Propulsion Conference & Exhibit, Joint Propulsion Conferences
- [38] John W. Dankankh, “Direct Drive for Low Power Hall Thrusters”, Gray Research Inc., Huntsville, AL. Conference: 41st AIAA/ASME/SAE/ASEE Joint Propulsion, 2005
- [39] John A. Hamley, “Hall Thruster Direct Drive Demonstration” John M. Sankovic, John R. Miller, NASA Lewis Research Center Cleveland, Ohio; Mark J. O’Neill, Entech Inc. Keller, TX; Peter Lynn, Naval Research Laboratory, Washington, DC; Steven R. Oleson, NYMA Inc., Cleveland, Ohio. 33rd AIAA Joint Propulsion Conference, Seattle, 1997
- [40] David J. Hoffman, Thomas W. Kerslake, Jeffrey S. Hojnicky, David H. Manzella, Robert D. Falck, Harry A. Cikanek III, Mark D. Klem, and James M. Free, “Concept Design of High Power Solar

- Electric Propulsion Vehicles for Human Exploration”, Glenn Research Center, Cleveland, Ohio, December 2011
- [41] Kerslake T. W. “Effect of Voltage Level on Power System Design for Solar Electric Propulsion Mission”, International Solar Energy Conference, March 2003, NASA /TM-2003-212304.
- [42] W. Andrew Hoskins, “Direct Drive Hall Thruster System Development” Daniel Homiak and R. Joseph Cassady, Aerojet-General Corporation, Redmond, WA; Tom Kenlake, Todd Peterson, Dale Ferguson and Dave Snyder, NASA Glenn Research Center Cleveland, OH; Ioannis Mikellides and Gary Jongeward, Science Applications International Corporation, San Diego, CA; Todd Schneider, NASA Marshall Space Flight Center, Huntsville, AL. AIAA-2003-4726
- [43] Gabriele Impresario, “Design and Simulation of a 5 kW Hall Thruster Direct Drive Experiment”, Corso di Laurea Specialistica in Ingegneria Aerospaziale, Tesi di Laurea, Dipartimento di Ingegneria Civile e Industriale, Università di Pisa, 2015
- [44] Alessio Pampaloni, Mirko Trisolini, “Hall Thruster Direct-Drive Assessment and Demonstration”, Tesi di Laurea In Ingegneria Aerospaziale, Indirizzo Spaziale, Università Degli Studi di Pisa, 2013
- [45] Gary A. Jongeward, Ira Katz, Ioannis G. Mikellides, “High Voltage Solar Arrays for a Direct Drive Hall Effect Propulsion System” Science Applications, International Corporation, San Diego, CA; Melvin. R. Carruth, NASA/MSFC; David Q. King, General Dynamics; Eugene L. Ralph, TECSTAR; Todd Peterson, NASA/GRC. 27<sup>th</sup> Presented as Paper IEPC-01-000 at the International Electric Propulsion Conference, Pasadena, CA, 15-19 October 2001.
- [46] Alessio Pampaloni, Mirko Trisolini, University of Pisa; Tommaso Misuri, Mariano Andrenucci, Alta S.p.A., Ospedaletto, Pisa, “A Direct Drive System Application for Hall Effect Thrusters”, Presented at the 33rd International Electric Propulsion Conference, The George Washington University, Washington, D.C., USA, October 6 – 10, 2013
- [47] John Steven Snyder, John R. Brophy, “Peak Power Tracking and Multi-Thruster Control in Direct Drive Systems”, Jet Propulsion Laboratory, California Institute of Technology, Pasadena, CA. Presented at the 33rd International Electric Propulsion Conference, The George Washington University, Washington, D.C., USA, October 6 – 10, 2013
- [48] John Steven Snyder, John R. Brophy, Richard R. Hofer, Dan M. Goebel, Ira Katz, “Experimental Investigation of a Direct-Drive Hall Thruster and Solar Array System”, Jet Propulsion Laboratory, California Institute of Technology, Pasadena, California, Journal of Spacecraft and Rockets Vol. 51, No. 1, January–February 2014
- [49] Reinhardt K. C., “Space Power Technology in Power Management and Distribution Electronics”, Journal of Spacecraft and Rockets, Vol. 35, No. 6, November-December 1998
- [50] Francis F. Chen, “Lecture Notes on Langmuir Probe Diagnostics”, Electrical Engineering Department, University of California, Los Angeles, Mini-Course on Plasma Diagnostics, IEEE-ICOPS meeting, Jeju, Korea, June 5, 2003.

- [51] Ira Katz, Alejandro Lopez Ortega, Dan M. Goebel, Michael J. Sekerak, Richard R. Hofer, Benjamin A. Jorns, John R. Brophy, "Effect of solar array plume interactions on Hall thruster cathode common potentials", Jet Propulsion Laboratory, California Institute of Technology, USA. 14th Spacecraft Charging Technology Conference, ESA/ESTEC, Noordwijk, NL, 04-08 APRIL 2016
- [52] Farbod Faraji, Maryam Reza, Ugo Cesari, Nicola Giusti, Tommaso Andreussi, Giacomo Morreale, Luca Benetti, Mariano Andrenucci, SITAEL S.p.A, Pisa, Italy; Denis Estublier, ESA-ESTEC, Noordwijk, The Netherlands, "Experimental Investigation of a Direct-Drive Hall Thruster", Space Propulsion 2018, Barcelo Renacimiento Hotel, Seville, Spain / 14–18 May 2018
- [53] D.E. Parks, I. Katz, "Spacecraft-Generated Plasma Interaction with High-Voltage Solar Array", Systems, Science and Software, La Jolla, CA. 13th International Electric Propulsion Conference, International Electric Propulsion Conference, San Diego, CA, U.S.A., 1978
- [54] J.L. Herr, "Spacecraft Environments Interactions: Protecting Against the Effects of Spacecraft Charging", Sverdrup Technology, Inc. Huntsville, Alabama; M.B. McCollum, Marshall Space Flight Center, MSFC, Alabama; Electromagnetics and Environments Branch, Systems Definition Division, Systems Analysis and Integration Laboratory, Science and Engineering Directorate. National Aeronautics and Space Administration, Marshall Space Flight Center, Alabama, November 1994
- [55] Ronald L. Corey, David J. Pidgeon, "Electric Propulsion at Space Systems/Loral", Space Systems/Loral, Palo Alto, CA. Presented at the 31st International Electric Propulsion Conference, University of Michigan, Ann Arbor, Michigan, USA, September 20 – 24, 2009 IEPC-2009-270
- [56] Howard Gray, EADS Astrium Ltd, Portsmouth, UK; Severin Provost, EADS Astrium SAS, France; Michael Glogowski, Inmarsat Global Ltd, London, UK; Alain Demaire, EADS Astrium SAS, France, "Inmarsat 4F1 Plasma Propulsion System Initial Flight Operations". Presented at the 29th International Electric Propulsion Conference, Princeton University, October 31 November 4, 2005 IEPC-2005-082
- [57] Thomas M. Liu, Mitchell L. R. Walker, "Integration of Electric Propulsion Systems with Spacecraft, An Overview", Georgia Institute of Technology, Atlanta, GA, USA. Presented at the 33rd International Electric Propulsion Conference, The George Washington University, Washington, D.C., USA, October 6 – 10, 2013 IEPC-2013-355
- [58] Carruth, R. & Vaughn, J., Increasing Importance Of Material Electrical Interaction With The Space Environment, International Symposium on Materials in a Space Environment; 8th; 8 Jun. 2000; Arcachon, France.
- [59] Kerslake, W. R. & Ignaczak, L. R. Development and Flight History of the SERT II Spacecraft, JSR 30, pp 258-290, 1993.
- [60] 2)BILL G. HERRON, JOHN R. BAYLESS, and JOHN D. WORDEN. "High-Voltage Solar Array Technology", Journal of Spacecraft and Rockets, Vol. 10, No. 7 (1973), pp. 457-462.
- [61] Denis L. Estublier, The SMART-1 Spacecraft Potential Investigations, IEEE TRANSACTIONS ON PLASMA SCIENCE, VOL. 36, NO. 5, OCTOBER 2008

- [62] Luca Ghislanzoni, Luca Benetti, Tommaso Misuri, Giovanni Cesaretti and Lorenzo Fontani, “Hall Effect Thruster Direct Drive PUs, Experimental Investigation of the Cathode Potential Grounding Problem”. 11<sup>th</sup> European Space Power Conference, 23 May 2017

# Appendix A

Extract of reports of STK simulations

## CASE 1

3 Oct 2018 14:30:01

Civil Air Patrol Use Only

Satellite-Satellite1

Astrogator MCS Segment Summary Astrogator MCS Target Sequence Summary

---

MCS Segment Type: TargeterSequence

Name: Target Sequence

User Comment: Sequence that runs targeting profiles

Sequence Start: 27 Sep 2018 09:59:58.000 UTCG; 2458388.91664352 UTC Julian Date

Sequence Stop: 29 Jan 2019 22:20:34.460 UTCG; 2458513.4309544 UTC Julian Date

\*\*\*<<<< Start of Sequence: Target Sequence >>>>\*\*\*

\*\*\*-----\*\*\*

MCS Segment Type: Maneuver:Finite

Name: Target Sequence.Maneuver

User Comment: Maneuvers satellite with impulsive or finite burn

Propagator model used: Earth\_HPOP\_Default\_v10 (Default Earth HPOP settings for STK 10.0)

Stopping Condition Information (Gregorian Date [Julian Date]):

29 Jan 2019 22:20:34.460 [2458513.4309544]: Stopped on: Duration; Run Sequence STOP

Propagation Statistics:

Number of steps: 66402

Average step size: 162.006 sec

Largest step size: 1081.28 sec

Smallest step size: 40.063 sec

Maneuver Summary:

Maneuver Start: 27 Sep 2018 09:59:58.000 UTCG; 2458388.91664352 UTC Julian Date

Maneuver Stop: 29 Jan 2019 22:20:34.460 UTCG; 2458513.4309544 UTC Julian Date

Duration: 1.0758e+07 sec

Fuel Used: 430.9699506571806 kg

DeltaV Magnitude: 4589.401007483315 m/sec

Maneuver Direction Specification: Thrust Vector

Maneuver direction is updated during maneuver.

Burn centring is OFF.

Thrust Efficiency: 1 (Affects acceleration, but not mass flow rate)

## CASE 2

3 Oct 2018 13:39:23

Civil Air Patrol Use Only

Satellite-Satellite1

### Astrogator MCS Segment Summary Astrogator MCS Maneuver Summary

---

MCS Segment Type: Maneuver: Finite

Name Target Sequence.Manoeuvre

User Comment: Maneuvers satellite with impulsive or finite burn

Propagator model used: Earth\_HPOP\_Default\_v10 (Default Earth HPOP settings for STK 10.0)

Stopping Condition Information (Gregorian Date [Julian Date]):

27 Dec 2018 20:04:38.315 [2458480.33655457]: Stopped on: Duration; Run Sequence STOP

Propagation Statistics:

Number of steps: 49358

Average step size: 160.017 sec

Largest step size: 1079.13 sec

Smallest step size: 40.063 sec

Maneuver Summary:

Maneuver Start: 27 Sep 2018 09:59:58.000 UTCG; 2458388.91664352 UTC Julian Date

Maneuver Stop: 27 Dec 2018 20:04:38.315 UTCG; 2458480.33655457 UTC Julian Date

Duration: 7.89868e+06 sec

Fuel Used: 583.9448974329189 kg

DeltaV Magnitude: 4587.370090799202 m/sec

Maneuver Direction Specification: Thrust Vector

Maneuver direction is updated during maneuver.

Burn centring is OFF.

Thrust Efficiency: 1 (Affects acceleration, but not mass flow rate)

### CASE 3

3 Oct 2018 15:32:19

Civil Air Patrol Use Only

Satellite-Satellite1

Astrogator MCS Segment Summary Astrogator MCS Maneuver Summary

---

MCS Segment Type: Maneuver: Finite

Name Target Sequence.Manoeuvre

User Comment: Maneuvers satellite with impulsive or finite burn

Propagator model used: Earth\_HPOP\_Default\_v10 (Default Earth HPOP settings for STK 10.0)

Stopping Condition Information (Gregorian Date [Julian Date]):

3 Jan 2019 09:57:50.227 [2458486.91516467]: Stopped on: Duration; Run Sequence STOP

Propagation Statistics:

Number of steps: 52882

Average step size: 160.101 sec

Largest step size: 1078.57 sec

Smallest step size: 40.038 sec

Maneuver Summary:

Maneuver Start: 27 Sep 2018 09:59:58.000 UTCG; 2458388.91664352 UTC Julian Date

Maneuver Stop: 3 Jan 2019 09:57:50.227 UTCG; 2458486.91516467 UTC Julian Date

Duration: 8.46707e+06 sec

Fuel Used: 1251.931569863586 kg

DeltaV Magnitude: 4589.935458379644 m/sec

Maneuver Direction Specification: Thrust Vector

Maneuver direction is updated during maneuver.

Burn centring is OFF.

Thrust Efficiency: 1 (Affects acceleration, but not mass flow rate)

# Appendix B

Preliminary mass systems evaluation for the three cases examined in Chapter 3 and 4.

The tables represent each one a different architecture. An analysis of the Direct Drive configuration is present from the third table. This quantitative analysis is based on the observations and documents included in Chapter 4. Components are taken for the majority of GEO electric satellites that performed an EOR. However, the data inserted here are not to be taken as absolute since no flight-model PPU has been developed for this power level. The system mass and possible benefits are too dependent on the spacecraft configuration, which has not been well defined. Few data have been found on the sizing of the PMAD.

Rather than putting a safe margin for each system, we preferred to insert a conservative margin for the total structure. The Mass Growth Allowance (MGA) was placed at 20% and 25% of the total dry mass.

<i>subsystem</i>	EPS	EP	TCS	AOCS	CDH	TTC	Str& Mec	HARN
Case 1	18.5	31	9	-	1.5	0.5	38	2.5
Case 2	19	25	8.5	-	1.5	0.5	43	2
Case 3	26	26	11	6	1	0.5	33	3

**Table 17** Summary of the different dry mass % for each subsystem in each case.

Component/System	Mass %	Number	Basic Mass
		#	kg
<b>TUG</b>	<i>70,863</i>		1982,72
<b>Ideal Mass (STK)</b>			2800
<b>Payload</b>	<i>29,137</i>		817,28
<b>Tug dry mass</b>			1095,6
<b>Tug dry mass + Margin Mass</b>	<i>47,006</i>		1314,72
Margin Mass (%20)			241,032
<b>Tot dry ideal mass (STK)</b>			2200

<b>power and propulsion module</b>	<i>59,179</i>		<b>1655,8</b>
<b>EPS</b>	<i>7,268</i>		<b>203,5</b>
HARN (cables and harness)			28,5
battery Li-iON (155Wh/kg)		1	15
Solar Array		2	160
<b>TCS</b>	<i>3,500</i>		<b>98</b>
<b>EP</b>	<i>12,304</i>		<b>343,3</b>
PPUs		2	88,2
HT-20K		2	100
Feed System (FSC, PRs)			28,5
Support, control, gimbals		2	26,6
<b>STR&amp;MEC</b>	<i>14,679</i>		<b>411</b>
Propellant Tanks		2	31
Structures and Mechanisms			380
<b>Propellant</b>	<i>21,429</i>		<b>600</b>
<b>control module</b>	<i>1,421</i>		<b>39,8</b>
ADCS			16,5
CDH			16,8
TTC			6,5
<b>STR&amp;MEC support</b>	<i>2,429</i>		<b>68</b>
adapters and attaches			68

**Table 18** Case with 2 thrusters and 2 PPU. The base structure is the ESPA. In this configuration, only two tanks of propellant are necessary to perform also the return from GEO.

Component/System	Mass %	Number	Basic Mass
		#	kg
<b>TUG</b>	<i>73,199</i>		2046,44
<b>Ideal Mass (STK)</b>			2800
<b>Payload</b>	<i>26,801</i>		753,56
<b>Tug dry mass</b>			973,7
<b>Tug dry mass + Margin Mass</b>	<i>41,841</i>		1168,44
Margin Mass (%20)			214,214
<b>Tot dry ideal mass (STK)</b>			1990
<b>power and propulsion module</b>	<i>62,382</i>		1744,1
<b>EPS</b>	<i>6,596</i>		<b>184,7</b>
HARN (cables and harness)			21
battery Li-iON (155Wh/kg)		1	7,4
Solar Array		2	156,3
<b>TCS</b>	<i>2,964</i>		<b>83</b>
<b>EP</b>	<i>8,821</i>		<b>244,4</b>
DDUs		2	6,8
HT-20K		2	90
Feed System (FSC, PRs)			21
Support, control, gimbals		2	26,6
<b>STR&amp;MEC</b>	<i>15,071</i>		<b>422</b>
Propellant Tanks		3	42
Structures and Mechanisms			380
<b>Propellant</b>	<i>28,929</i>		<b>810</b>
<b>control module</b>	<i>1,414</i>		<b>39,6</b>
ADCS			16,3
CDH			16,8
TTC			6,5
<b>STR&amp;MEC support</b>	<i>2,429</i>		<b>68</b>
adapters and attaches			68

**Table 19** Case with 2 thrusters and 2 DDU. The base structure is the ESPA. In this configuration, three tanks of propellant are necessary to perform also the return from GEO. The mass benefit from Direct Drive configuration affects the component of the power and propulsion module causing the additional propellant to be less severe on the payload mass.

Component/System	Mass %	Number	Basic Mass
		#	kg
<b>TUG</b>	<i>66,799</i>		4001,624
<b>Ideal Mass (STK)</b>			6000
<b>Payload</b>	<i>33,201</i>		1998,376
<b>Tug dry mass</b>			1429,2
<b>Tug dry mass + Margin Mass</b>	<i>29,883</i>		1786,5
Margin Mass (%25)			314,424
<b>Tot dry ideal mass (STK)</b>			4110

<b>power and propulsion module</b>	<i>54,680</i>		<b>3275,6</b>
<b>EPS</b>	<i>6,147</i>		<b>368,8</b>
HARN (cables and harness)			42
battery Li-iON (155Wh/kg)		2	14,8
Solar Array			312
<b>TCS</b>	<i>2,667</i>		<b>160</b>
<b>EP</b>	<i>6,400</i>		<b>378,8</b>
Feed System (FSC, PRs)			42
DDUs		4	14,8
Hydrazine + AOCS			90
HT-20K		4	180
Support, control, gimbals		4	53,2
<b>STR&amp;MEC</b>	<i>7,967</i>		<b>478</b>
Propellant Tanks		7	98
Structures and Mechanisms			380
<b>Propellant</b>	<i>31,500</i>	<b>7</b>	<b>1890</b>
<b>control module</b>	<i>0,727</i>		<b>43,6</b>
ADCS			20
CDH			16,9
TTC			6,7
<b>STR&amp;MEC support</b>	<i>6,133</i>		<b>368</b>
adapters and attaches			68
chaser or docking mechanism (mating)			300

**Table 20** Six tons tug with 4 thrusters and 4 DDU. The base structure is the ESPA. In this configuration, 7 tanks of propellant are necessary to perform also the return from GEO. The mass benefit from Direct Drive configuration affects the component of the power and propulsion module causing the additional propellant to be less severe on the payload mass.

# Appendix C

## Code description

How they work and which formulas they use.

1. `current_function.m`
2. `tugLEOGEO.m`
3. `bigsolvent100.m` & `bigsolvent300.m`

### Part One

Program on the basic of sheath theory. To calculate current density on any surface of the system At the end we will have in fact a  $j = j_{is} + j_e$  that is sum of the two ionic and electron densities

The space potential place to 0 V.

$n_e$  and  $T_e$  insert for both plasmas. The single current densities are

$$j_{is} = \frac{1}{2} n q u_b$$
$$j_e = -q n v_e \exp(V - \phi_s)$$
$$j_e = -q n v_e$$

with

$$u_b = \left(\frac{q T_e}{m_i}\right)^{0.5} \quad v_e = \left(\frac{q T_e}{2 \pi m_e}\right)^{0.5}$$

The ionic current is always saturated when it is not fixed.

For the electronic density instead, there are two ways: the saturation way when the potential of the surface passes the space plasma e the normal current densities for the region of negative potential.

### Part Two

Problem data. The resistances Ra and Rb are here fixed.

Given a voltage between 150 and -150V in this range the  $s / c$  may vary, the solution is  $V_{sol}$ .

It is the spacecraft voltage which makes currents null, then it is the solution to equilibrium.

This gives also all the four current.

At the end the value of Va and Vb on the resistances are evaluated.

### Part Three

The code uses directly `current_function`. Just enter a voltage or range and the two resistances from a correct answer (or a current vector). We have put here the known dimensions of the various parts and potential differences.

$w$  and  $L$  panel dimensions (with PICplus these will be superfluous).

The code seek balance by making sure that the sum of currents arriving on S/C, as point of reference, are zero.

I1 is the current between plume and S/C.

I2 is the current between SA and S/C. It will be composed in one way for the part under the 0 of the plasma and in another way for the part above the plasma.

I3 is the current between cathode and S/C.

I4 is the current between thruster body and S/C.

$\Delta V_1 = 100 \text{ V}$  or  $300 \text{ V}$ .

I2 recalculate the current density for better results. For a point on the panel the potential is

$$V_{sc} + \Delta V_1 * y/L$$

It is then multiplied by w and by 1/100 (for now we do not know how much area of the panel is actually conductive we know that it is little we put a penny in reality is less, the exact data will be possible to get it only with PICplus).

I4 is the final current for the non-linearity equation system. Fsolve is used to find the “x”

`x-current_function(nth, Teth, phiS, V(i)+x*R2)*Sth`

The plasma here is more dense and energetic

$$V4 = V_{sc}(sol) + I_4 R_2$$

After these codes, the codes used to extract the data from the ".dat" files deriving from the study with Picplus and Tecplot have been placed, in order to extract the values to calculate the current on the solar array portion.

The program must iterate until the equilibrium is found, since the current variation is due to the low or high (with respect to the plasma) the S/C with the potential but the change in current influences the formula of the  $\phi_{sc}$  itself. Case striking is the current collection of the solar array that depends on how much solar array in percentage is below or above the plasma threshold then positive or negative compared to this. As the program iterates more and more defines the area that is positive with respect to the plasma, it goes without saying that changing the collection area changes the currents, that makes the  $\phi_{sc}$  change, which makes the potential margins of the spacecraft change again. Precisely the areas or rather the positions of zero on the solar panel (with the iterations) this point will be lowered more and more until equilibrium.

Dimensions for satellite.

$l1 = 3 \text{ m}$ ;  $l2 = 3.6 \text{ m}$ .

Dimensions for solar panels or area need for 25kW SEP.

Area =  $125 \text{ m}^2$ ;

Number of panels = 2;

$w = 3 \text{ m}$ ;  $L = 20.8 \text{ m}$ ;

Dimensions of the portion of solar array, considering the worst condition between SA and plume cone.

$w = 2.216 \text{ m}$ ;  $L = 8.19 \text{ m}$ ;

Area =  $18.15 \text{ m}^2$

Thruster plume plasma  $T_{e,th} = 3 \text{ eV}, n_{th} = 10^{16} \text{ m}^{-3}$ .

Space plasma  $T_{e,pl} = 1 \text{ eV}, n_{pl} = 10^{14} \text{ m}^{-3}$ .

## Matlab Codes

```
%%%%%%%%%%%%%%%%%%%%%%%%%%%%%%%%%%%%%%%%%%%%%%%%%%%%%%%%%%%%%%%%%%%%%%%%%
CURRENT FUNCTION
%%%%%%%%%%%%%%%%%%%%%%%%%%%%%%%%%%%%%%%%%%%%%%%%%%%%%%%%%%%%%%%%%%%%%%%%%

function j = current_function(n,Te,phis,V)
%Ambivalent function to evaluate the current densities

q = 1.60e-19;
me = 9.11e-31;
mi = 2.19e-25;
vb = ((q*Te)/mi)^0.5;
ve = (q*Te/(2*pi*me))^0.5;
% Ionic Current Densities
jis = 0.5*n*q*vb*ones(size(V)); %[A/m^2]
je = -q*n*ve*ones(size(V)); %[A/m^2]
nV = length(V);
for i=1:nV
    if phis>V(i)
        je(i) = je(i)*exp((V(i)-phis)/Te);
    end
end
j = jis+je;
end

%%%%%%%%%%%%%%%%%%%%%%%%%%%%%%%%%%%%%%%%%%%%%%%%%%%%%%%%%%%%%%%%%%%%%%%%%
TUG LEOGEO,
%%%%%%%%%%%%%%%%%%%%%%%%%%%%%%%%%%%%%%%%%%%%%%%%%%%%%%%%%%%%%%%%%%%%%%%%%

% clc
% clear all
% close all
%% Evaluation of the four current in one iteration with bisolvent100.m and
bigsolvent300.m

V=-150:10:150;
Ra = 1e1;
Rb = 1e4;
    = bigsolvent100(V,Ra,Rb);
% I = bigsolvent300(V,Ra,Rb);
[~,imin] = min(sum(I,1).^2);
V0 = V(imin);
funI = @(v) sum(bigsolvent100(v,Ra,Rb),1);
% funI = @(v) sum(bigsolvent300(v,Ra,Rb),1);
Vsol = fsolve(funI,V0);
```

```

Isol = bigsolvent100(Vsol,Ra,Rb);
% Isol = bidsolvent300(Vsol,Ra,Rb);
deltaVa = Isol(3,1)*Ra;
deltaVb = Isol(4,1)*Rb;
Vth= Vsol+deltaVb;
fprintf(' Spacecraft voltage is %f V \n',Vsol);
fprintf(' Solar Array voltage goes from %f V to %f V \n', Vsol, Vsol+100);
fprintf(' CRP is -15V \n');
fprintf(' Difference potential on Ra is %f V; \n difference potential on Rb is %f
V; \n',deltaVa, deltaVb);
fprintf(' Thruster body voltage %f V \n', Vth);
fprintf(' I1 = %f A; \n I2 = %f A; \n I3 = %f A; \n I4 = %f A;
\n',Isol(1,1),Isol(2,1),Isol(3,1),Isol(4,1));

```

```

%%%%%%%%%%%%%%%%%%%%%%%%%%%%%%%%%%%%%%%%%%%%%%%%%%%%%%%%%%%%%%%%%%%%%%%%
BIGSOLVENT 100
%%%%%%%%%%%%%%%%%%%%%%%%%%%%%%%%%%%%%%%%%%%%%%%%%%%%%%%%%%%%%%%%%%%%%%%%

```

```

function I = bigsolvent100(V,R1,R2)

```

```

%Dimensions

```

```

l1 = 3;l2 = 3.6;
w = 3; L = 41.66;
Asc = l1*l2;
Sth = 0.2537; %area taken from Katz work

```

```

%Potential

```

```

phis = 0;
diffpot1 = 100;
Vhc = 15;
CRP = -Vhc;

```

```

% Plasma near the solar array and the spacecraft

```

```

Tep1=1; npl=10^14;%
% Plasma plume near thruster surfaces
Teth=3; nth=10^16;

```

```

%Current

```

```

I1 = zeros(size(V));
I2 = zeros(size(V));
I3 = zeros(size(V));
I4 = zeros(size(V));

```

```

nV = length(V);

```

```

options = optimoptions('fsolve','Display','none');

```

```

x0 = 0;

```

```

for i=1:nV

```

```

    I1(i) = current_function(npl,Tep1,phis,V(i))*Asc;

```

```

%    jsa = @(y) current_function(npl,Tep1,phis,(V(i)+diffpot1*y/L))*w*1/10000;

```

```

%questa è da modificare con i dati in PICPLUS o 1/100

```

```

%    I2(i) = integral(jsa,0,L);

```

```

    %I2(i)=-0.0019; %dal primo pic

```

```

    I2(i)=-0.0016; %dopo la prima coppia di estremi

```

```

    I3(i) = (CRP-V(i))/R1;

```

```

    fun = @(x) x-current_function(nth,Teth,phis,V(i)+x*R2)*Sth;

```

```

    %x is the I4 to find
    I4(i) = fsolve(fun,x0,options); x0 = I4(i);
end
I = [I1;I2;I3;I4];
end

```

```

%%%%%%%%%%%%%%%%%%%%%%%%%%%%%%%%%%%%%%%%%%%%%%%%%%%%%%%%%%%%%%%%%%%%%%%%
BIGSOLVENT 300
%%%%%%%%%%%%%%%%%%%%%%%%%%%%%%%%%%%%%%%%%%%%%%%%%%%%%%%%%%%%%%%%%%%%%%%%

```

```

function I = bigsolvent300(V,R1,R2)

%Dimensions
l1 = 3;l2 = 3.6;
% w = 3;L = 20.8; ma con la nuova I2 non contano più sono state prese da picplus
w =3; L = 41.66;
Asc = l1*l2;
Sth = 0.2537; %area taken from Katz work

%Potential
phiS = 0;
diffpot1 = 300;
Vhc = 15;
CRP = -Vhc;

% Plasma near the solar array and the spacecraft
Tep1=1; npl=10^14;%
% Plasma plume near thruster surfaces
Teth=3; nth=10^16;

%Current
I1 = zeros(size(V));
I2 = zeros(size(V));
I3 = zeros(size(V));
I4 = zeros(size(V));

nV = length(V);
options = optimoptions('fsolve','Display','none');
x0 = 0;
for i=1:nV
    I1(i) = current_function(npl,Tep1,phiS,V(i))*Asc;

    %w*1/100 modifica la nostra densità di corrente
    % si passa a 1/10000 non 1/100000
    %   jsa = @(y) current_function(npl,Tep1,phiS,(V(i)+diffpot1*y/L))*w*1/10000;
    %   I2(i) = integral(jsa,0,L);
    I2(i)=-0.0018; %corrente massima di pic plus
    I3(i) = (CRP-V(i))/R1;
    fun = @(x) x-current_function(nth,Teth,phiS,V(i)+x*R2)*Sth;
    %x is the I4 to find
    I4(i) = fsolve(fun,x0,options); x0 = I4(i);
end
I = [I1;I2;I3;I4];
end

```

## Matlab Codes in relation with PICPluS Study

Load files .dat in form of matrices, data collected by Tecplot or Paraview only on the surface of the simulation panel ended.

Get from these files: the matrix of connectivity, the 3D coordinates of the extremes; the number densities, the temperatures and areas of each triangle.

Calculate the barycenters of triangles and the coordinate on the solar panel which is at 0 V.

Generally, the size of the solar array should no longer be entered in the code because it is already part of the .dat file.

```
%%%%%%%%%%%%%%%%%%%%%%%%%%%%%%%%%%%%%%%%%%%%%%%%%%%%%%%%%%%%%%%%%%%%%%%%
New CURRENT FUNTION
%%%%%%%%%%%%%%%%%%%%%%%%%%%%%%%%%%%%%%%%%%%%%%%%%%%%%%%%%%%%%%%%%%%%%%%%
```

```
function j = c_f(n,Te) % j = c_f(n,Te,phis,V)
%nuova current function
q = 1.60e-19;
me = 9.11e-31;
mi = 2.19e-25;
vb = ((q*Te)/mi)^0.5;

T=1; %potrebbe variare con temperatura attenzione coie potrebbe essere
v = (q*T/(2*pi*me))^0.5;
alfa=(1.58e-3)/(10e14*q*v);

    ve = (q*Te/(2*pi*me))^0.5;
    je = alfa*n*ve*q;

j=je; %si considera nulla jis cosi
end
```

```
%%%%%%%%%%%%%%%%%%%%%%%%%%%%%%%%%%%%%%%%%%%%%%%%%%%%%%%%%%%%%%%%%%%%%%%%
NUOVA LETTURA (takes data from PIC and Tecplot files)
%%%%%%%%%%%%%%%%%%%%%%%%%%%%%%%%%%%%%%%%%%%%%%%%%%%%%%%%%%%%%%%%%%%%%%%%
```

```
%estrazione 100V datipic100.txt
X=datipic100([1:98],:);
x=reshape(X,[1,882]);
xx=x(1:881);

Y=datipic100([99:196],:);
y=reshape(Y,[1,882]);
yy=y(1:881);

Z=datipic100([197:294],:);
```

```

z=reshape(Z,[1,882]);
zz=x(1:881);

surf =datipic100([1883:1883+1588-1],1);
numberdensity =datipic100([6647:6647+1588-1],1);
TEM =datipic100([8235:8235+1588],1);
CON =datipic100([39995:end],[1:3]);

bari=[0 0 0];
for i=1:1588
    a=CON(i,1);
    b=CON(i,2);
    c=CON(i,3);
    %matrice dei baricentri di ogni trinagolo
    bari(i,:)=[(xx(a)+xx(b)+xx(c))/3,
(yy(a)+yy(b)+yy(c))/3,(zz(a)+zz(b)+zz(c))/3];
end

%% tutto il pannello positivo corrente direttamnte da picplus pre iterazione

dim=length(surf);
area=0;
int=0;
for i=1:dim
    area=area+surf(i);
    int=int+(numberdensity(i)*surf(i));
end
KATZ=1.58e-3;
maxI=int*KATZ/10e14
fprintf('area pannello è di %f \n', area );
fprintf('integrale è di %f \n', int );

% prima a 0.0019 questi sono i limiti del pannello
high = 85.715797;
low = -14.284203;

% 14.282206 V to 85.717794 alla seconda lettura non cambia gia piu nulla

B=low;
L=(2.73*3); % 2.2163m w dimensioni Pannello PiC

dot=-(-B*L/100)+max(yy);% rifasato nel sistema di riferimento del pannello

% % selezione con i baricentri
% Nar=0; %new area
% inte=0; %integrale
% for i=1:dim
%     j(i) = bari(i,2);
%     if j(i) < dot %è negativo il pan
%         Nar=Nar+surf(i);
%         inte=inte+(numberdensity(i)*surf(i));
%     end
% end

%% nuova selezione a zig zag
Nar=0; %new area
inte=0; %integrale
for i=1:1588

```

```

a=CON(i,1);
b=CON(i,2);
c=CON(i,3);
%ricoda che le coordinate y del pannello hanno direzione crescente
%verso sinistra sono negative
%   if (yy(a) < dot && yy(b)< dot) || (yy(a) < dot && yy(c)< dot) || (yy(c) <
dot && yy(b)< dot)
%   if yy(a) < dot && yy(b)< dot && yy(c) < dot %sovrastimata area
%   positiva
%   if (yy(a) < dot && yy(b) < dot && yy(c)>dot) || (yy(a)>dot && yy(b) < dot &&
yy(c)<dot) || (yy(a)<dot && yy(b)>dot && yy(c) < dot) || (yy(a)<dot && yy(b)<dot
&& yy(c)<dot)
        Nar=Nar+surf(i);
        inte=inte+(numberdensity(i)*surf(i));
    end
end
NEWmaxI=inte*KATZ/10e14
fprintf('area pannello positiva è di %f \n', Nar );
fprintf('integrale è di %f \n', inte );
Itot=0;
totsurf=0;
for i=1:1588
    I(i,1) = c_f(numberdensity(i),TEM(i))*surf(i);
    totsurf(i)= surf(i);
    Itot(i)=I(i,1);
    if i>=2
        Itot(i)=Itot(i-1)+I(i,1);
        totsurf(i)= totsurf(i-1)+surf(i);
    end
end
end
plot(totsurf,Itot)

```

# Appendix D

## Results tables

All the various cases evaluated with matlab code previously presented.

Legend: inf = resistance 1e6 ohm;

0 = resistance 1e0 ohm;

### First step

V <sub>sc</sub> (V)	-98,53	-89,54	-17,70	-17,72	-89,33	-98,29	-17,70	-98,28	-93,93
V <sub>th</sub> (V)	-17,91	-89,24	-17,91	-17,73	-89,03	-17,99	-17,91	-17,91	-18,77
$\Delta V_a$ (V)	83,53	74,54	2,70	2,72	74,33	83,29	2,70	83,28	78,93
$\Delta V_b$ (V)	80,62	0,30	-0,20	-0,02	0,30	80,30	-0,20	80,38	75,16
I1 (A)	0,073850	0,073850	0,073850	0,073850	0,073850	0,073850	0,073850	0,073850	0,073850
I2 (A)	-0,074006	-0,374394	-2,776314	-2,775743	-0,381750	-0,081951	-2,776314	-0,822460	-0,227939
I3 (A)	0,000084	0,000075	2,702465	2,719478	0,007433	0,000083	2,702485	0,008328	0,078927
I4 (A)	0,000080	0,300475	-0,000001	-0,017585	0,300475	0,008030	-0,000020	0,000080	0,075155
R <sub>a</sub> ( $\Omega$ )	inf	inf	0	0	10000	inf	0	10000	1000
R <sub>b</sub> ( $\Omega$ )	inf	0	inf	0	0	10000	10000	inf	1000

Table 21 Results with plasma 0 V,  $\Delta V_1 = 100$  V,  $\Delta A = \frac{1}{100}$ , CRP = -15V.

### Second step

V <sub>pl</sub> (V)	98,53	89,54	17,70	17,72	89,33	98,29	17,70	98,28	93,93
CRP (V)	83,53	74,54	2,70	2,72	74,33	83,29	2,70	83,28	78,93
V <sub>th</sub> (V)	80,62	0,30	-0,20	-0,02	0,30	80,30	-0,20	80,38	75,16
$\Delta V_a$ (V)	83,53	74,54	2,70	2,72	74,33	83,29	2,70	83,28	78,93
$\Delta V_b$ (V)	80,62	0,30	-0,20	-0,02	0,30	80,30	-0,20	80,38	75,16
I1 (A)	0,073850	0,073850	0,073850	0,073850	0,073850	0,073850	0,073850	0,073850	0,073850
I2 (A)	-0,074006	-0,374394	-2,776314	-2,775743	-0,381750	-0,081951	-2,776314	-0,822460	-0,227939
I3 (A)	0,000084	0,000075	2,702465	2,719478	0,007433	0,000083	2,702485	0,008328	0,078927
I4 (A)	0,000080	0,300475	-0,000001	-0,017585	0,300475	0,008030	-0,000020	0,000080	0,075155
R <sub>a</sub> ( $\Omega$ )	inf	inf	0	0	10000	inf	0	10000	1000
R <sub>b</sub> ( $\Omega$ )	inf	0	inf	0	0	10000	10000	inf	1000

Table 22 Results with spacecraft grounded at 0 V,  $\Delta V_1 = 100$  V,  $\Delta A = \frac{1}{100}$ , CRP = -15V.

Third step

V <sub>sc</sub> (V)	-15,00	-115,00	-15,00	-115,00	-65,00
V <sub>th</sub> (V)	-15,00	-115,00	85,00	-15,00	-15,00
ΔV <sub>a</sub> (V)	0,00	-261,18	0,00	244,41	31,00
ΔV <sub>b</sub> (V)	0,00	0,00	-0,85	-203,44	-101,72
I <sub>1</sub> (A)	0,0738	0,0738	0,0738	0,0738	0,0738
I <sub>2</sub> (A)	-2,8667	0,0085	-2,8667	0,0085	-1,1950
I <sub>3</sub> (A)	3,2844	-0,3829	120,0395	0,4092	1,6127
I <sub>4</sub> (A)	-0,4916	0,3005	-117,2466	-0,4916	-0,4916
<b>V<sub>a</sub> (V)</b>	<b>0</b>	<b>100</b>	<b>0</b>	<b>100</b>	<b>50</b>
<b>V<sub>b</sub> (V)</b>	<b>0</b>	<b>0</b>	<b>100</b>	<b>100</b>	<b>50</b>

**Table 23** Results with plasma 0 V, ΔV<sub>1</sub> = 100 V, ΔA =  $\frac{1}{100}$ , CRP = -15V, Box A and B are power supply.

Fourth step

V <sub>sc</sub> (V)	-293,56	-266,62	-18,07	-18,05	-251,76
V <sub>th</sub> (V)	-17,91	-266,32	-17,91	-18,04	-22,24
ΔV <sub>a</sub> (V)	278,56	251,62	3,07	3,06	236,76
ΔV <sub>b</sub> (V)	275,64	0,30	0,16	0,01	229,53
I <sub>1</sub> (A)	0,073850	0,073850	0,073850	0,073850	0,073850
I <sub>2</sub> (A)	-0,074401	-0,374577	-3,144484	-3,144631	-0,540147
I <sub>3</sub> (A)	0,000279	0,000252	3,070634	3,057427	0,236764
I <sub>4</sub> (A)	0,000276	0,300475	0,000000	0,013354	0,229526
<b>R<sub>a</sub> (Ω)</b>	<b>inf</b>	<b>inf</b>	<b>0</b>	<b>0</b>	<b>1000</b>
<b>R<sub>b</sub> (Ω)</b>	<b>inf</b>	<b>0</b>	<b>inf</b>	<b>0</b>	<b>1000</b>

**Table 24** Results with plasma 0 V, ΔV<sub>1</sub> = 300 V, ΔA =  $\frac{1}{100}$ , CRP = -15V.

Fifth step

V <sub>sc</sub> (V)	-6,53	-17,43	-14,95	-15,29	-6,57
V <sub>th</sub> (V)	-17,91	-17,48	-17,91	-15,64	17,89
ΔV <sub>a</sub> (V)	-8,47	2,43	-0,05	0,29	-8,42
ΔV <sub>b</sub> (V)	-11,38	-0,05	-2,95	-0,34	-11,32
I <sub>1</sub> (A)	0,031505	0,073849	0,073841	0,073844	0,033459
I <sub>2</sub> (A)	-0,031499	0,073849	-0,028682	-0,028568	-0,031484
I <sub>3</sub> (A)	-0,000008	0,000002	-0,045156	0,295087	-0,000843
I <sub>4</sub> (A)	-0,000011	-0,046005	-0,000003	-0,340363	-0,001132
<b>R<sub>a</sub> (Ω)</b>	<b>inf</b>	<b>inf</b>	<b>0</b>	<b>0</b>	<b>1000</b>
<b>R<sub>b</sub> (Ω)</b>	<b>inf</b>	<b>0</b>	<b>inf</b>	<b>0</b>	<b>1000</b>

**Table 25** Results with plasma 0 V, ΔV<sub>1</sub> = 100 V, ΔA =  $\frac{1}{10000}$ , CRP = -15V.

Sixth step

V <sub>sc</sub> (V)	-6,56	-17,47	-14,95	-15,30	-17,47	-6,58	-14,96	-6,58	-7,15
V <sub>th</sub> (V)	-17,91	-17,51	-17,91	-15,64	-17,51	-17,90	-17,89	-17,91	-17,80
ΔV <sub>a</sub> (V)	-8,44	2,47	-0,04	0,29	2,47	-8,42	-0,04	-8,42	-7,85
ΔV <sub>b</sub> (V)	-11,35	-0,04	-2,95	-0,34	-0,04	-11,31	-2,95	-11,33	-10,80
I1 (A)	0,032748	0,073800	0,073841	0,073844	0,073849	0,033864	0,073841	0,033579	0,051164
I2 (A)	-0,032725	-0,031512	-0,031792	-0,031754	-0,031512	-0,032725	-0,031792	-0,032726	-0,032662
I3 (A)	-0,000008	0,000002	-0,042046	0,297796	0,000247	-0,000008	-0,041755	-0,000842	-0,007850
I4 (A)	-0,000011	-0,042345	-0,000003	-0,339886	-0,042589	-0,001131	-0,000295	-0,000011	-0,010654
R <sub>a</sub> (Ω)	inf	inf	0	0	10000	inf	0	10000	1000
R <sub>b</sub> (Ω)	inf	0	inf	0	0	10000	10000	inf	1000

Table 26 Results with plasma 0 V, ΔV<sub>1</sub> = 300 V, ΔA =  $\frac{1}{10000}$ , CRP = -15V.

Seventh step (PIC)

V <sub>sc</sub> (V)	-5,99	-17,19	-14,93	-15,27	-14,28	-14,28
V <sub>th</sub> (V)	-17,91	-17,26	-17,91	-15,62	-17,90	-17,90
ΔV <sub>a</sub> (V)	-9,00	2,19	-0,07	0,27	-0,72	-0,72
ΔV <sub>b</sub> (V)	-11,91	-0,07	-2,98	-0,34	-3,00	-3,62
I1 (A)	-0,0019	0,0738	0,0738	0,0738	0,0738	0,0738
I2 (A)	-0,0019	-0,0019	-0,0019	-0,0019	-0,0019	-0,0016
I3 (A)	0,0000	0,0000	-0,0719	0,2724	-0,0716	-0,0718
I4 (A)	0,0000	-0,0720	0,0000	-0,3444	-0,0004	-0,0004
R <sub>a</sub> (Ω)	inf	inf	0	0	1	1*
R <sub>b</sub> (Ω)	inf	0	inf	0	10000	10000*

Table 27 Results with plasma 0 V, ΔV<sub>1</sub> = 100 V, with Picplus evaluation of I2, (\*)the last column is the second iteration.

Eighth step (PIC)

V <sub>sc</sub> (V)	-5,99	-17,19	-14,93	-15,27	-14,28	-14,28
V <sub>th</sub> (V)	-17,91	-17,26	-17,91	-15,62	-17,90	-17,90
ΔV <sub>a</sub> (V)	-9,01	2,19	-0,07	0,27	-0,72	-0,72
ΔV <sub>b</sub> (V)	-11,91	-0,07	-2,98	-0,34	-3,62	-3,62
I1 (A)	0,0018	0,0738	0,0738	0,0738	0,0738	0,0738
I2 (A)	-0,0018	-0,0018	-0,0018	-0,0018	-0,0018	-0,0018
I3 (A)	0,0000	0,0000	-0,0720	0,2723	-0,0717	-0,0717
I4 (A)	0,0000	-0,0721	0,0000	-0,3444	-0,0004	-0,0004
R <sub>a</sub> (Ω)	inf	inf	0	0	1	1*
R <sub>b</sub> (Ω)	inf	0	inf	0	10000	10000*

Table 28 Results with plasma 0 V, ΔV<sub>1</sub> = 300 V, with Picplus evaluation of I2, (\*) the last column is the second iteration.

# Appendix E

## PICPluS Basic description

PICPluS is a Particle In Cell (PIC) MCC/DSMC validated simulation code, with direct simulation of propellant ions and neutral atoms coming from the thruster, indirect simulation of background and fluid dynamic treatment of the electrons.

The present version (3.6) is capable to simulate the flow for any Hall Effect Thruster (HET) or Gridded Ion Engine (GIE), provided that reliable input data are available.

*The PICPluS code (Particle In Cell Plume Simulator) is meant to be a simulation instrument to study and predict the features of plasma thruster their interaction with space vehicle surfaces.*

In this approach, the simulation of heavy species is performed on a particulate basis superimposed to a grid-based simulation of the light species. More specifically the single or multiple charged ions of the simulated plasma and the neutral atoms, which originate from non-ionized propellant or from the partial pressure of the background gas, are modelled by particles.

The much lighter electrons are modelled on a grid by assuming quasi neutrality of the plasma in every simulation cell:

$$n_e = n_i$$

with  $n_e$  and  $n_i$  denoting the number of electrons and ions respectively.

By further assuming adiabatic expansion of the electron gas, the simplified electron momentum equation can be solved for the plasma potential.

$$\varphi = \varphi_{ref} + \frac{k_B T_{ref}}{q} \frac{\gamma}{\gamma - 1} \left[ \left( \frac{n_e}{n_o} \right)^{\gamma - 1} - 1 \right]$$
$$\varphi = \varphi_{ref} + \frac{k_B}{q} \frac{\gamma}{\gamma - 1} [T_e - T_{ref}]$$

Here the free parameters of the adiabatic exponent, of the reference electron temperature, plasma potential and electron number at the plasma-inlet are respectively given by  $\gamma$ ,  $T_{ref}$ ,  $\varphi_{ref}$  and  $n_{ref}$ .

To further increase the computational speed of the simulation, the single ions and neutrals are integrated into super-particles, which behave like single entities but rather represent collections of ions. This method enables the use of simulation domains as large as entire test-chambers or satellites.

These super-particles obey the equations of motion and interact with the plasma potential computed above:

$$m \frac{dv}{dt} = -q(\nabla\varphi - v\mathbf{B})$$

Collisions between the ions and neutrals result in charge exchange (CEX) collisions, where the fast moving ions transfer their charge to the slow moving neutrals. These generated slow ions move towards the sides of the plasma driven by the plasma potential gradient and can even move to angles larger than 90° as was shown by numerous studies.

Even if these CEX ions exhibit much lower energies than the fast ions, their impact on a satellite surface can still generate an erosion of the material. Therefore, a lot of care must be taken to model the outer ranges of the plume correctly in terms of ion current and ion energy.

To simulate the plasma plume generated by an electric propulsion thruster in an on-ground experiment, the experimental settings, such as propellant mass flow, gas pressure and thrust are set accordingly. Furthermore, the ionization and acceleration efficiency and the parameters from the above equations are chosen specific to the thruster type.

For all simulations in this work, it is ensured that the quasi-neutrality-assumption is not violated and that the grid propagates in a smooth way as described in.

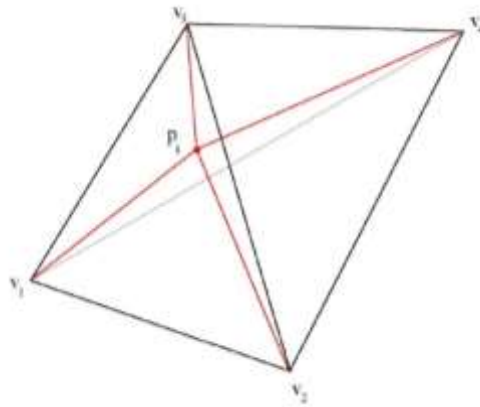


**Figure 47** Tetrahedral schematic.

In order to compute equation we need to have the value  $s$  of charge density on the nodes of the computational mesh. To accomplish this, the charge of each macro-particle is scattered on the particles or the tetrahedron to which the particle belongs, using weighting factors.

### PICPlus features

- 2D 3D axisym, 3 components of velocity
- Structured grid with variable cell size (scaled to local Debye length)
- Xe<sup>+</sup>, Xe<sup>++</sup>, Xe simulated particles
- Elastic, CEX collisions (2 different algorithms)
- Effect of background pressure
- Input from experimental distributions or from external simulations (magnetostatic FEM)
- Simulated engines: Hall Effect Thruster or Gridded Ion Engine
- Evaluation of cross section
- Gas surface interaction sputtering model and different particles reflections.

### Algorithms

- Particle in Cell with Ruyten weighting
- Nanbu-Kitatani TPMC or Szabo MCC (Monte Carlo Collisions) dynamics.

- 3 models for collision cross-sections
- Potential from Poisson solver (SOR method, Chebishev acceleration, checker-board ordering) or quasi-neutrality (Boltzmann relation)
- 3 models for electron temperature (constant, adiabatic, first order Chapman-Enskog) or experimental distribution
- Full DSMC option for neutrals
- All input fields/distributions from experiments, simulations, or simplified models
- Sputter erosion model (Yamamura Model)
- CLL (Cercignani Lampis Lord) scattering kernels for particles reflections.

## Outputs

- Instantaneous and averaged fields at steady state (species by species)
- Instantaneous and averaged thrust and beam ion current
- Ion current density measured with virtual Faraday's probe rakes
- Impact history on (possible) solid external surface and related statistics.

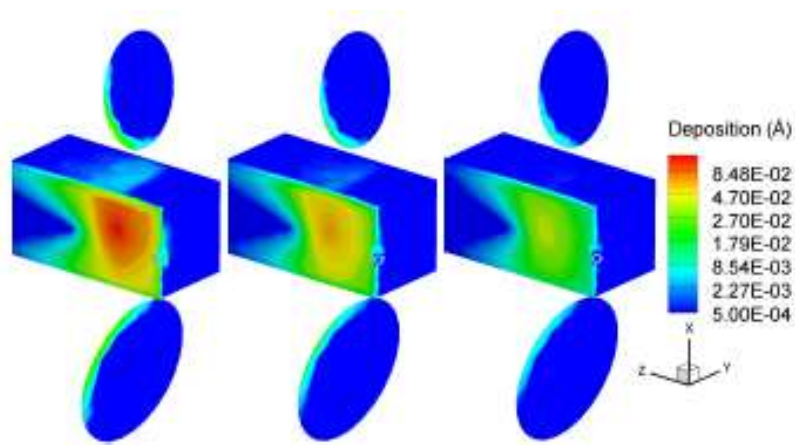


**Figure 48** Deposition of silver after one panel revolution in 3600s. Result of a simulation re-deposition of sputtered material - Tecplot.

## The Program

The program is written in Fortran 90, parallelized with the OpenMP libraries to take advantage of multi-processor/multi-core hardware configurations.



**Figure 49** Main GUI window.

The first step for the set-up of a simulation is usually the preparation of the mesh file and of the proper boundary conditions set.

PICPlus default mesh generator is the open source Gmsh software.

First a .geo input file have to be created. Than a Gmsh mesh file once a .geo file is available. This carries out the pre-processing of the Gmsh mesh file with the generation of the grid file (.grd) required by Picplus starting dromfile .msh.

The files with boundaries are made. The data are completed and the plasma far field becomes concrete.

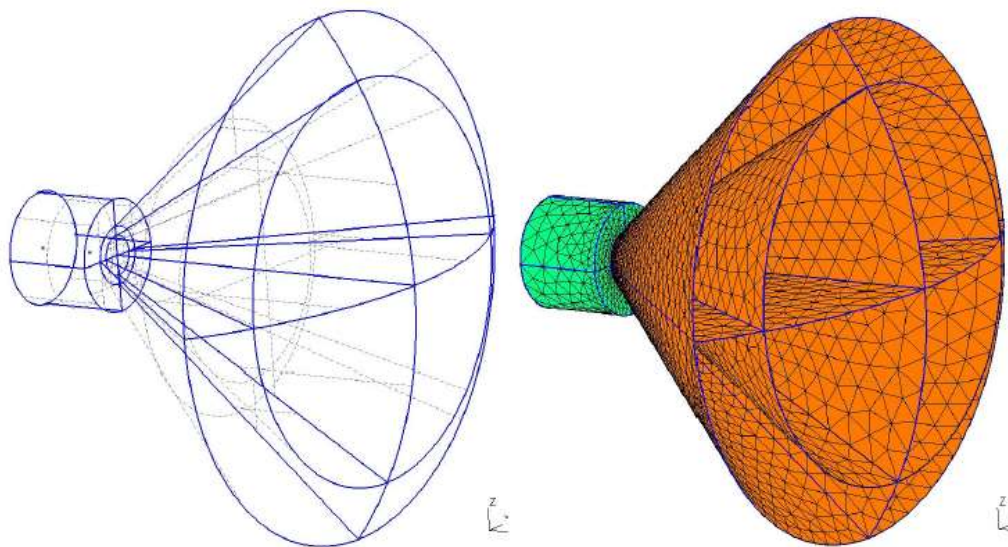


**Figure 50** Geometry of the thruster affection area obtained through the Gmsh geo file.

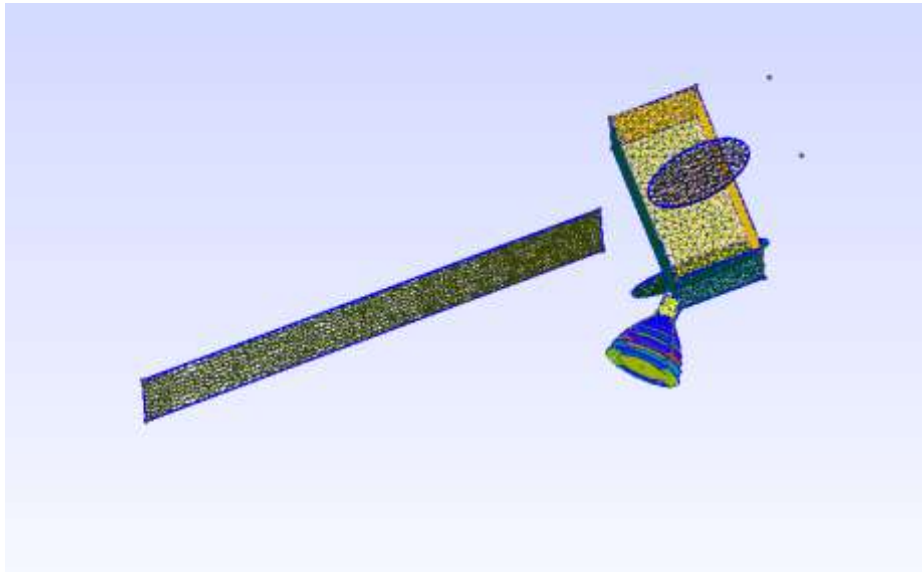


**Figure 51** An example of satellite model computed with Gmsh. Here the 2D mesh is visible.

In the simulation window we can set parameters:

- Number of time step to be performed;
- Time step size (s) =  $\Delta t$ ;
- Neutrals time step multiplier;
- Presence of a plume of neutral to be read from a file;
- Option to collect speed distribution;
- Option to start rotation the panel module, avoiding the stating of a new simulation only for changing the orientation of SA;
- Number of time steps after which quantities and plasma interactions start to be averaged (flow fields);
- Number of processors available for the simulation.

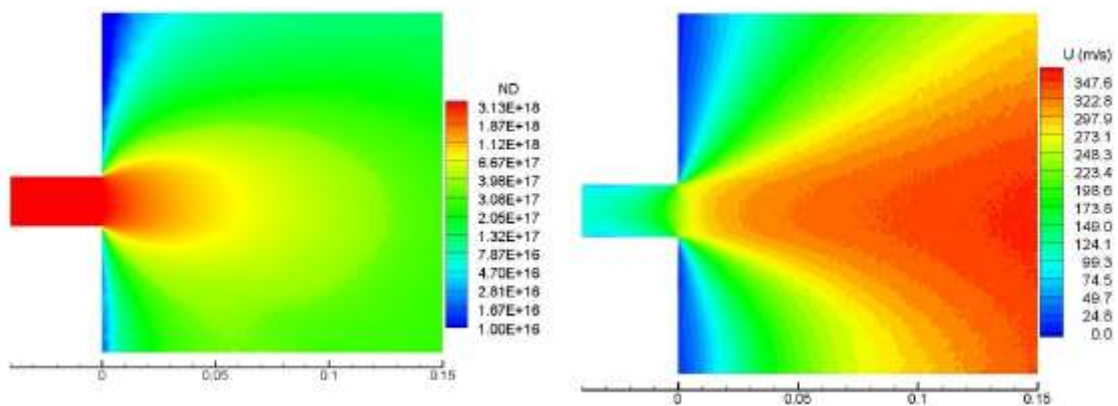


**Figure 52** Computed number density (left) and axial speed (right) - Tecplot.

At each time step new particles are injected in the simulation model through the thrusters exit plane. The number of macro particles to be injected for each simulated specie is a function of the corresponding mass flow, computed on the basis of the assigned thruster parameters previously set up. Moreover it is possible to change the diagnostics, the materials, the types of impacts, the sputtering, the types of particles rotate the solar panels and various inclinations surfaces.